technische universität
dortmund

Dissertation
zur Erlangung des akademischen Grades eines
Doktors der Naturwissenschaften
(Dr. rer. nat.)

Projected Gradient Stabilization for Unfitted Finite Element Methods with Application to Tumor Growth

Der Fakultät für Mathematik der
Technischen Universität Dortmund
vorgelegt von

Jan-Phillip Bäcker

im Januar 2026

Dissertation

Projected Gradient Stabilization for Unfitted Finite Element Methods with Application to Tumor Growth

Von der Fakultät für Mathematik der Technischen Universität Dortmund zur Veröffentlichung angenommene Dissertation zur Erlangung des akademischen Grades eines Doktors der Naturwissenschaften (Doctor rerum naturalium).

Erstgutachter:	Prof. Dr. Dmitri Kuzmin
Zweitgutachter:	Prof. Dr. Maxim Olshanskii
Drittprüfer:	Prof. Dr. Matthias Röger
Vorsitzender der Prüfungskommission:	Prof. Dr. Christoph Buchheim
Abgabedatum:	13. Januar 2026
Datum der mündlichen Prüfung:	14. April 2026

Imagination is more important than knowledge. For knowledge is limited, whereas imagination embraces the world [...].

~ Albert Einstein
Cosmic Religion and Other Opinions and Aphorisms

Abstract

Motivated by mathematical models for tumor growth, the work conducted in this thesis is focused on stabilization techniques for unfitted finite element methods (FEMs). In such models, appropriate transmission conditions are imposed on the possibly evolving sharp interface between the subdomains occupied by the tumor and surrounding tissue. To avoid frequent remeshing, an unfitted FEM may be employed that uses a fixed background mesh together with an implicit description of the geometry. However, the presence of small cut cells can lead to numerical instabilities, poor conditioning of the system matrix and loss of accuracy caused by small cut cells. To deal with this issue, we introduce a new ghost penalty based on the difference between two consistent discretizations of the Laplacian operator.

The proposed projected-gradient stabilization is straightforward to implement and provides an implicit extension of the solution beyond the physical domain. We show that the bilinear form of the stabilization term is symmetric and establish second order convergence in L^2 for the solution of the discrete problem. To overcome difficulties associated with numerical integration over sharp embedded interfaces, a diffuse-interface description based on a level set representation is developed. Results of several numerical examples support the theoretical analysis and illustrate the performance of the proposed unfitted FEM. Since the lumped-mass L^2 projection that we use for gradient recovery is at most second-order accurate, we introduce nodal averaging as an alternative projection operator for the stabilization term to attain optimal-order accuracy for higher-order polynomial approximations. The stabilization concept is then extended to unfitted FEMs for elliptic interface problems with discontinuous coefficients, for which analogous stability and convergence results are obtained. Moreover, the proposed stabilization is incorporated into an unfitted FEM for a convection–diffusion problem with an embedded interface, and its effectiveness is demonstrated by a numerical example.

The unfitted FEM with projected-gradient stabilization is applied to a mathematical model for tumor growth. Using formal asymptotic expansions, a thin-rim limit problem for a tumor growth model is derived. In the thin-rim limit, the pressure satisfies a Poisson equation with a Robin boundary condition in a time-dependent domain whose evolution is governed by a forced mean curvature flow. In the case of stationary, rotationally symmetric solutions, the weak-star convergence of the pressure solution in L^∞ is proven. A generalized thin-rim limit problem is discretized using the proposed stabilized unfitted FEM. The obtained numerical results exhibit good qualitative agreement with results published in the literature and illustrate convergence properties of the proposed method.

Acknowledgments

At this point, I would like to express my sincerest gratitude to all those who supported me throughout the completion of this thesis and who made the past six years an exciting and varied time.

First and foremost, I am deeply grateful to Prof. Dr. Dmitri Kuzmin, who supervised this work and provided the research topic. His guidance, support, and encouragement over the years have meant a lot to me; especially during the corona virus pandemic, when I was about to quit my PhD. I particularly appreciate that he gave me the opportunity to attend numerous conferences during my doctoral studies and that I was allowed to contribute to his workshop "Modeling and Simulation of Transport Phenomena 2025" as a co-organizer. I would furthermore like to thank Dmitri for carefully proofreading my thesis and providing helpful suggestions.

I would like to express my gratitude to Prof. Dr. Matthias Röger for supervising parts of this thesis. Through many fruitful discussions, Matthias helped me establish several results in Chapter 5. Additionally, I am grateful for his willingness to serve as an examiner during my PhD defense. I am also thankful to Matthias for kindly proofreading parts of this thesis.

My sincere thanks extend to Prof. Dr. Maxim Olshanskii, with whom I had the opportunity to collaborate. This collaboration provided the foundation for many parts of this thesis. I am thankful to him for agreeing to act as a reviewer of this thesis and as an examiner during my PhD defense.

I would equally like to thank Prof. Dr. Christoph Buchheim for his willingness to chair the examination board.

I am indebted to Dr. Christoph Lohmann and Dr. Timm Treskatis for their careful proofreading and constructive feedback. My appreciation further extends to Prof. Dr. Stefan Turek and the entire LS3 research group for creating a pleasant and productive working environment. In particular, I would like to thank Jun.-Prof. Dr. Hennes Hajduk, Falko Ruppenthal, Joshua Vedral, and Paul Moujaes for the many insightful and inspiring discussions we shared.

During my PhD studies, I had the great opportunity to visit Lawrence Livermore National Laboratory (LLNL) as an intern. I would like to thank everyone who made this visit possible, especially Dr. Vladimir Tomov, my supervisor at LLNL. In addition, I would like to acknowledge the MFEM group at LLNL for developing and maintaining such a powerful open-source software library that has contributed substantially to this work.

I also sincerely thank the Bischöfliche Studienförderung Cusanuswerk for its ideological and financial support during my Bachelor's and Master's programs.

My heartfelt thanks go to my friends — especially Henrik Eichholz, Johanna Grüll, Lars Dielmann, and Dr. Katharina Wegener — for their constant support and for the many enjoyable game nights that brought balance and joy during demanding times.

Finally, my deepest gratitude goes to my family. Their unwavering support, encouragement, and belief in me made this work possible. Specifically, I would like to thank my parents, Claus Bäcker and Elisabeth Bäcker-Heusch, my brother Dr. Claus Maximilian Bäcker, as well as Insa-Marie Schneider. Whenever I encountered a problem or simply needed someone to talk to, they were always there to listen. In moments of self-doubt, they encouraged me, restored my confidence, and helped me stay on course toward my goal.

Thank you so much!

Jan-Phillip Bäcker

Contents

1 Introduction

A wide range of processes in nature, medicine, physics, and other applications can be modeled using partial differential equations (PDEs). The variables involved in such models represent velocities, concentrations, or other quantities associated with phases or species. An important application for PDEs is the mathematical modeling and simulation of tumor growth. As emphasized by Gatenby and Gawlinski in [GG03], tumor growth involves nonlinear interactions across multiple spatial and temporal scales. Hence, intuition and qualitative reasoning alone are insufficient to completely understand the behavior of tumors. Mathematical models combined with accurate numerical methods enable investigations of tumor dynamics without the need for costly or ethically challenging experiments. Depending on the underlying model, these simulations can incorporate a wide variety of biological influences or even predict the response of tumors to therapeutic interventions; see, e.g., [Pre03].

Starting in the first half of the 20th century, modeling tumor growth became increasingly popular (cf. [AM04]). Since the early developments, interest in this field has increased steadily, with a substantial rise in activity beginning in the 1990s, leading to many publications. Many of these publications build upon the framework established by Burton ([Bur66]), Greenspan ([Gre72; Gre74; Gre76]), and McElwain ([MP77; MM78]). In the early 2000s, a variety of modeling approaches emerged. Examples include mixture-theoretic models treating the tumor as a solid phase embedded in a liquid environment (cf. [BP03]), two-phase flow models in which the tumor comprises two interacting phases (cf. [Byr+03]), and incompressible fluid models where the tumor is explicitly treated as a viscous fluid (cf. [HMS05]). Around the same time, additional biological aspects were incorporated into the mathematical models. For instance, the inclusion of tumor angiogenic factors led to a variety of models describing the vascularization of a tumor; see, e.g., [DP00; CLN03; ZWC05; HMS06; SBP13; XVG16]. Other approaches considered the interaction between tumor cells and the immune system; see, e.g., [BP00; AB12]. Each of these extensions increased the biological accuracy of the models but also added significant mathematical and computational complexity. A step toward linking macroscopic tumor behavior with microscopic cell-level processes was achieved through multiscale formulations. Lowengrub ([Low+10]), Peng ([Pen+17]), and Carraro ([Car+21]) proposed two-phase models that describe the tumor and the extracellular matrix as distinct phases. Coupling macroscopic evolution equations with cell-scale dynamics,

the models capture how local interactions and cellular mechanisms on the microscale can influence the tumor dynamics.

A recent model for nutrient-driven tumor growth was introduced by Eyles and coauthors in [Eyl19; EKS19]. Building on earlier models by Ward ([WK97]) and King ([KF06]), they developed a simplified yet tractable formulation that captures key mechanisms such as nutrient uptake, proliferation, cell death, and necrotic core formation. The objective of this model is not biological accuracy but rather the development of a mathematical framework to which additional biological complexity can be added. Edelmann et al. ([EKL25]) refined this model to facilitate theoretical studies of numerical discretization.

In the last years, phase-field approaches for tumor growth models gained popularity (cf. [Haw+13; CGH15; FGR15; Gar+16; GT22; Tra24]). These formulations couple the governing tumor equations with a Cahn–Hilliard-type phase-field model. This yields a diffuse-interface representation of the tumor boundary. Therefore, these models offer several advantages, including straightforward handling of topological changes. However, for certain applications, particularly those in which the interface between healthy and tumorous tissue needs to be sharply localized, a diffuse-interface approximation may be inappropriate. In such cases, the numerical method must resolve a sharp tumor boundary and impose appropriate transmission conditions on it. Several strategies for the accurate numerical treatment of conditions on sharp interfaces and boundaries exist in the literature. A widely used approach, also used in this thesis, is to employ an unfitted finite element method (FEM) with suitable stabilizations.

1.1 State of the art

Unfitted FEMs, which employ a fixed and often structured background mesh, offer significant benefits in terms of computational cost. Their flexibility has made them increasingly popular for solving PDEs posed on domains with discontinuous material properties or evolving geometries (cf. [Bor+18]). Throughout this section, the term interface refers to both genuine interfaces and domain boundaries. A wide variety of unfitted discretization techniques has been proposed in the literature. These methods include the immersed boundary method (cf. [LL97; Pes00; MI05]), the extended FEM (XFEM) (cf. [CSB02; ABI12; BGN13; Leh15]), as well as many other approaches.

Based on Nitsche's idea [Nit71], symmetric unfitted Nitsche FEMs have been introduced for various elliptic PDEs (cf. [HH02; CB09; BET11; Wad+13; HLZ14; Cho24]). These methods impose interface and boundary conditions weakly through

surface integrals. However, a drawback of unfitted Nitsche formulations is their sensitivity to small cut cells. Such cut configurations often yield ill-conditioned system matrices and may cause numerical instabilities. To mitigate these effects, stabilization terms can be incorporated, giving rise to the cutFEM methodology. Among several possible stabilizations (cf. [Bur12; BHL18]), a widely used approach is the ghost penalty (GP) stabilization introduced by Burman in [Bur10]. In the GP framework, a stabilization term penalizing the difference between the solution and its projection into the finite element space is added on patches consisting of a moderate number of elements surrounding the interface. These patches are constructed in such a way that every cut cell belongs to one of them. Subsequently, Burman et al. (see [BH10; BH12; BH14; Mas+14; Bur+15; BCM15; Pre+23]) adapted the concept of continuous interior penalty (CIP) (cf. [BE07]) to stabilize unfitted methods against small cut cells. The stabilization is applied on the same patches as in the original GP approach but penalizes jumps of the normal derivative across facets. The resulting GP stabilization using CIPs can also be used to stabilize convective terms (cf. [BE07]) and is therefore effective in many contexts. However, these stabilizations do not readily accommodate limiters for enforcing discrete maximum principles (DMPs). High-order extensions of cutFEM have been developed in recent years (cf. [BE18; MSW18; Bur+21; Wah21]). To extend the GP approach to time-dependent problems, Lehrenfeld and Olshanskii ([LO19]) applied the stabilization on a wider strip of elements around the interface. Recently, Olshanskii and von Wahl ([OW25]) demonstrated that a global application of GP stabilization is required to attain certain stability properties. Many of these approaches are supported by theoretical studies, including optimal a priori error estimates and bounds for the condition number.

A different GP-type approach was proposed by Badia and coauthors in [BNV22]. Using the concept of aggregate finite elements (cf. [BVM18]), they penalized the difference between the gradient of the solution and the gradient of its projection into the aggregate finite element space. Codina and coauthors also used the difference between gradients and projected gradients to stabilize against cut cells (see [Cod+23]). For the Navier–Stokes equation they define a subdomain consisting of cut elements and their interior neighbors and penalize the difference between the gradients of the pressure and velocity with their L^2 projected counterparts on the subdomain.

A potential difficulty of unfitted approaches lies in the computation of surface integrals. However, these integrals can be approximated by volumetric integrals using approximate Dirac delta functions; see, e.g., [ETT05; Hys06; Sme06; Tei+07; ZT10; Tei+11; KT16; KT18]. To use these approximations, the quantities appearing in the surface integral must be extended in the normal direction, typically using constant extrapolation. Such extensions can be computed either with PDE-based

techniques (cf. [Che+97; AS99; UK18]) or through closest-point search algorithms as in [KB22].

Another promising approach recently emerging from the unfitted Nitsche method is the shifted-boundary method (SBM) (see [MS18a; MS18b; ACS20; Li+20; ACS21; Sau+21; Yan+24]), which belongs to the class of surrogate boundary methods. Instead of operating on small cut cells, the SBM applies surrogate boundary conditions on facets shared by cut and uncut elements. Facets sufficiently close to the true boundary are chosen to construct a surrogate boundary lying either completely inside or completely outside the physical domain. After determining the closest point on the true boundary, the transfer of data to the shifted boundary is accomplished by a Taylor expansion (cf. [MS18a; MS18b; ACS20]). A similar strategy for jump conditions on genuine interfaces is described in [Li+20]. The SBM is conceptually simple and supported by rigorous theoretical results (cf. [MS18a; ACS21; Ant+24]), including high-order extensions (cf. [ACS22]). Nonetheless, the closest-point projection required for mapping to the true boundary can be computationally demanding, and the convergence rate may degrade for certain geometries. To reduce this sensitivity, [Yan+24] proposes constructing the surrogate boundary in a manner that allows it to cross the true boundary locally.

1.2 Outline and originality of the thesis

We conclude this chapter with an outline of the thesis. In Chapter 2, we introduce an elliptic boundary value problem (BVP) and an elliptic interface problem as model problems and apply a fitted FEM to discretize them. The chapter ends with an overview of techniques to incorporate interfaces in numerical methods. Topics discussed in this chapter are well established in the literature. We present the unfitted Nitsche method for elliptic BVPs as described in the literature in Chapter 3. Using the idea proposed in [OBK25], we introduce an alternative to the common GPs and analyze the convergence of the resulting unfitted FEM. Although the analysis follows the structure of [OBK25], all derivations were carried out independently by the author. We further formulate a diffuse-interface variant using the narrow-band extension based on level set functions introduced in [KB22]. The chapter concludes with numerical examples that illustrate the performance, stability, and accuracy of the proposed approach. Following the same structure, Chapter 4 extends these ideas to elliptic interface problems. This chapter is based on the publication [OBK25]. The numerical analysis in the paper was originally performed by Prof. Maxim Olshanksii and is detailed here by the author of this thesis. In Chapter 5, we apply the stabilized unfitted FEM to a mathematical model for tumor growth. Following [EKS19], we introduce a nutrient-driven tumor growth model and derive

its thin-rim limit. For stationary, rotationally symmetric configurations, we provide a rigorous proof showing that the pressure component of the tumor model converges to the solution of the thin-rim limit problem. The limit problem is generalized by decoupling the curvature term from the boundary condition and discretized using an unfitted FEM. Finally, we compare numerical results obtained with our method to those reported in [EKS19], demonstrating the validity and robustness of the proposed discretization. We wrap up this thesis with the conclusions in Chapter 6. The key results of this thesis are summarized and several directions for future research are outlined.

Throughout the preparation of this thesis, the large language model ChatGPT5 was used for linguistic refinement. Sentences written by the author were reformulated by artificial intelligence. These reformulations were critically reviewed and revised by the author, ensuring clarity, precision, and conformity with academic writing standards. All scientific research, theoretical analysis, and numerical work were conducted solely by the author and his coworkers.

2 Model problems and interface description

This chapter introduces the stationary model problems used in Chapters 3 and 4, the concept of finite element discretizations, as well as different techniques to handle time-dependent interfaces numerically. The chapter is structured into three sections. Section 2.1 introduces the Poisson equation as the model problem for second-order elliptic boundary value problems (BVPs). We derive the weak formulation and construct a fitted finite element method (FEM) on a mesh aligned with the geometry. The section concludes with a convergence result for the solution of the discrete problems.

In Section 2.2, we turn our attention to an elliptic interface problem in which the diffusion coefficient exhibits a jump across a smooth embedded interface. The model problem is introduced in the strong and weak form, and discretized using a fitted finite element approach. This approach uses a mesh that is aligned with both the outer geometry and the embedded interface.

The final section has a completely different focus. In Section 2.3 we give an overview of some numerical techniques to handle interfaces numerically. Even though the numerical treatment of interfaces can be neglected in the case of stationary problems with analytically given interfaces, handling interfaces accurately becomes important for problems, in which the governing equation or the domain is time dependent.

Together, these three sections provide the context for the methods introduced in subsequent chapters.

2.1 Elliptic boundary value problem

Following the presentation in [Eva10], we introduce the Poisson equation as a model problem for an elliptic BVP. Let $\Omega \subset \mathbb{R}^d$, $d = 1, 2, 3$, be a bounded domain with boundary $\Gamma = \partial\Omega$. For functions $f : \Omega \to \mathbb{R}$, $g : \Gamma \to \mathbb{R}$, and $\mu : \Omega \to \mathbb{R}$ with $\mu \geq \mu_0 > 0$ smooth, the elliptic BVP under consideration is given by: Find $u : \Omega \to \mathbb{R}$ such that

$$-\nabla \cdot (\mu \nabla u) = f \qquad \text{in } \Omega, \tag{2.1a}$$

$$u = g \qquad \text{on } \Gamma. \tag{2.1b}$$

The boundary condition in (2.1b) is called a Dirichlet boundary condition. Alternatively, one may prescribe a Neumann boundary condition $\mu\partial_{\mathbf{n}}u = g$ or a Robin boundary condition $u + \mu\partial_{\mathbf{n}}u = g$, where $\partial_{\mathbf{n}}$ is the normal derivative. In what follows we restrict our attention to the Dirichlet BVP.

Classical theory requires solutions of (2.1) to satisfy $u \in C^2(\Omega) \cap C(\overline{\Omega})$ (cf. [Sch24]), which in turn demands $f \in C(\Omega)$ and $g \in C(\Gamma)$. However, this might not be satisfied by given data. To solve the elliptic BVP in a more general setting, we introduce the weak formulation of the problem. Assume that $f \in L^2(\Omega)$ and $g \in L^2(\partial\Omega)$. We call $u \in H^1(\Omega)$ a weak solution of (2.1) if $u = g$ on Γ and

$$\int_\Omega \mu\nabla u \cdot \nabla\phi \mathrm{d}\mathbf{x} = \int_\Omega f\phi \mathrm{d}\mathbf{x} \quad \forall\phi \in H_0^1(\Omega). \tag{2.2}$$

This weak formulation is obtained by multiplying the partial differential equation (PDE) (2.1a) with a test function $\phi \in H_0^1(\Omega)$, integrating over Ω and using integration by parts.

To construct a numerical scheme for the elliptic BVP, we consider the weak form (2.2). Following [LT08], we first assume that Ω is a polytope. Let $\mathcal{T}_h$ denote a conforming triangulation fitted to Ω, that is, $\overline{\Omega} = \bigcup_{K\in\mathcal{T}_h} K$. The mesh-size parameter h is defined as $h = \min_{K\in\mathcal{T}_h} h_K$ with $h_K = \operatorname{diam} K$. Let V_h be the finite element space of continuous, piecewise affine functions defined on $\mathcal{T}_h$. Precisely,

$$V_h = \{v_h \in C(\overline{\Omega}) : v_h|_K \in P_1(K) \ \forall\, K \in \mathcal{T}_h\}.$$

For the discrete problem, we require two subspaces of V_h. The test function ϕ in (2.2) vanishes on Γ, and we reflect this property in the discrete space

$$V_{h,0} = \{v_h \in V_h : v_h|_\Gamma = 0\}.$$

Likewise, the finite element approximation to the solution satisfies the boundary condition $u = g$. The corresponding space is defined as

$$V_{h,g} = \{v_h \in V_h : v_h|_\Gamma = g\}.$$

We can now formulate the discrete elliptic BVP as follows: Find $u_h \in V_{h,g}$ such that

$$\int_\Omega \mu\nabla u_h \cdot \nabla\phi_h \mathrm{d}\mathbf{x} = \int_\Omega f\phi_h \mathrm{d}\mathbf{x} \quad \forall\phi_h \in V_{h,0}. \tag{2.3}$$

We now drop the assumption that the domain Ω is a polytope and assume that Ω is a convex domain with smooth boundary. In this case, an exact fitted triangulation

is not available. However, by selecting suitable points on Γ, we can construct a triangulation $\mathcal{T}_h$ of Ω, such that $\Omega \setminus \bigcup_{K\in\mathcal{T}_h} K$ is of order $O(h^2)$.

The following theorem states that the solution of the discrete problems converge to the weak solution of the elliptic BVP.

Theorem 2.1. *Assume that $u_h \in V_{h,g}$ solves (2.3) and let $u \in H^2(\Omega)$ be a solution of (2.2). Then,*

$$\|u_h - u\|_{0,\Omega} \leq Ch^2 \|u\|_{2,\Omega},$$

where C is a constant independent of the mesh size.

For a proof of this theorem, see, e.g., [LT08, Thm. 5.4]

Remark 2.1. *Instead of using piecewise affine functions, we can define the finite element spaces with higher-order polynomial approximations. If the domain is a polytope, polynomial approximations of degree p yield convergence of order $p+1$ for the solution of the discrete problem.*

2.2 Elliptic interface problem

In the previous section, we assumed that the diffusion coefficient is smooth in the entire domain. We now drop this smoothness assumption and allow the diffusion coefficient to be piecewise constant.

Let $\Omega \subset \mathbb{R}^d$, $d \in \{1,2,3\}$, be a bounded Lipschitz domain, subdivided into two disjoint subdomains Ω_1 and Ω_2 by a smooth embedded interface Γ. Denote by $\mathbf{n}$ the unit normal to Γ pointing outward from Ω_1. For a function $v : \Omega \to \mathbb{R}$, we denote by v_k its restriction to Ω_k, $k = 1,2$. We define the jump $[\![v]\!] = v_1 - v_2$ of v across Γ and the weighted average $\{v\} = \kappa_1 v_1 + \kappa_2 v_2$, with nonnegative weights κ_1 and κ_2 depending on $\mathbf{x} \in \Gamma$. For a vector field $\mathbf{v}(\mathbf{x})$, the jump $[\![\mathbf{v}]\!] = (\mathbf{v}_1 - \mathbf{v}_2)\cdot\mathbf{n}$ and the average $\{\mathbf{v}\} = (\kappa_1\mathbf{v}_1 + \kappa_2\mathbf{v}_2)\cdot\mathbf{n}$ are defined in the normal direction $\mathbf{n}$. Let $\mu_k > 0$ be constant diffusion coefficients in the corresponding subdomains, $f_k : \Omega_k \to \mathbb{R}$, and $g : \partial\Omega \to \mathbb{R}$. Consider the following elliptic interface problem: Find $u_k : \Omega_k \to \mathbb{R}$, $k = 1,2$, such that

$$-\nabla\cdot(\mu\nabla u) = f \quad \text{in } \Omega_k,\ k = 1,2, \tag{2.4a}$$
$$u = g \quad \text{on } \partial\Omega, \tag{2.4b}$$
$$[\![u]\!] = 0 \quad \text{on } \Gamma, \tag{2.4c}$$
$$[\![\mu\nabla u]\!] = 0 \quad \text{on } \Gamma, \tag{2.4d}$$

where

$$\mu = \begin{cases} \mu_1 & \text{in } \Omega_1, \\ \mu_2 & \text{in } \Omega_2. \end{cases}$$

To derive the weak formulation, we multiply (2.4a) with test functions $\phi_k \in H_k$, where $H_k = \{\phi \in H^1(\Omega_k) : \phi|_{\partial\Omega \cap \partial\Omega_k} = 0\}$ and integrate over the corresponding domain Ω_k. Integration by parts yields

$$\begin{aligned} \int_{\Omega_1} \mu_1 \nabla u_1 \cdot \nabla \phi_1 \mathrm{d}\mathbf{x} - \int_\Gamma \mu_1 \nabla u_1 \cdot \mathbf{n} \phi_1 \mathrm{d}s + \int_{\Omega_2} \mu_2 \nabla u_2 \cdot \nabla \phi_2 \mathrm{d}\mathbf{x} + \int_\Gamma \mu_2 \nabla u_2 \cdot \mathbf{n} \phi_2 \mathrm{d}s \\ = \int_{\Omega_1} f_1 \phi_1 \mathrm{d}\mathbf{x} + \int_{\Omega_2} f_2 \phi_2 \mathrm{d}\mathbf{x} \quad \forall \phi_1 \in H_1, \phi_2 \in H_2. \end{aligned}$$

Owing to the interface condition (2.4d), the interface terms cancel. This yields the following weak problem: Find $u \in H_g$, where $H_g = \{\phi_k \in H^1(\Omega_k) : \phi|_{\partial\Omega} = g \wedge \phi_1|_\Gamma = \phi_2|_\Gamma\}$ such that

$$\begin{aligned} \int_{\Omega_1} \mu_1 \nabla u_1 \cdot \nabla \phi_1 \mathrm{d}\mathbf{x} + \int_{\Omega_2} \mu_2 \nabla u_2 \cdot \nabla \phi_2 \mathrm{d}\mathbf{x} \\ = \int_{\Omega_1} f_1 \phi_1 \mathrm{d}\mathbf{x} + \int_{\Omega_2} f_2 \phi_2 \mathrm{d}\mathbf{x} \quad \forall \phi_1 \in H_1, \phi_2 \in H_2. \end{aligned}$$

To construct a fitted FEM for the elliptic interface problem, we consider a conforming triangulation $\mathcal{T}_h$ of Ω. We assume that $\mathcal{T}_h$ is fitted to the interface, meaning that the induced subtriangulations $\mathcal{T}_{h,1}$ and $\mathcal{T}_{h,2}$ provide conforming triangulations of Ω_1 and Ω_2, respectively. This assumptions imply a $d-1$-dimensional triangulation of Γ by facets of elements within $\mathcal{T}_h$. As in the previous section, let V_h denote the finite element space of piecewise affine functions defined on $\mathcal{T}_h$, that is,

$$V_h = \{v_h \in C(\overline{\Omega}) : v_h|_K \in P_1(K) \ \forall K \in \mathcal{T}_h\}.$$

We again define the subspaces $V_{h,0}$ and $V_{h,g}$ as above. The discrete interface problem then reads as: Find $u_h \in V_{h,g}$ such that

$$\int_\Omega \mu \nabla u_h \cdot \nabla \phi_h \mathrm{d}\mathbf{x} = \int_\Omega f \phi_h \mathrm{d}\mathbf{x} \quad \forall \phi_h \in V_{h,0}.$$

Note that the diffusion coefficient μ is constant in the subdomains and discontinous across Γ.

2.3 Interface description

The model problems (2.1) in Section 2.1 and (2.4) in Section 2.2 involve stationary domain boundaries and interfaces. However, in many practical applications, the geometry of the domain or the position of the interface varies in time. To address such situations, different numerical techniques, handling evolving boundaries and interfaces in time-dependent problems, have been developed. Throughout this section, the term interface refers to both genuine interfaces and domain boundaries. Following [Bas17; Bän+23], we provide an overview over some of these techniques and introduce the employed approach below.

A common classification distinguishes between interface tracking methods and interface capturing methods.

Interface tracking methods describe the interface explicitly by mesh-related quantities. Consequently, the mesh follows the movement of the interface. In contrast, interface capturing methods represent the interface implicitly, typically through an auxiliary scalar field. Before discussing specific approaches, we summarize some advantages and limitations of these two classes of methods.

Using an explicit representation of the evolving geometry, interface tracking methods enable accurate evaluation of geometric quantities, such as curvature, and typically pose no difficulties when incorporating boundary conditions or material discontinuities. Because the mesh moves with the interface, these methods are well suited for moderate interface deformations. However, they struggle with topological changes, and large deformations may lead to severely distorted cells, which in turn may necessitate remeshing.

Interface capturing methods have become standard tools in many applications. They can accommodate complex deformations, arbitrary topological changes, and large interface motions. Their main challenges lie in preserving geometric properties, such as volume, and in achieving accurate evaluations of curvature and related quantities. Several enhanced formulations have been proposed to address these difficulties.

In what follows, we discuss representative methods from each category in more detail.

2.3.1 Interface tracking methods

In interface tracking methods, the interface $\Gamma(t)$ is represented explicitly. We distinguish between two main classes within this category: moving mesh methods and front tracking methods.

Moving mesh methods In moving mesh methods, the computational mesh is fitted to the interface, meaning that the discrete approximation of $\Gamma(t)$ aligns with element facets. The mesh is moved in accordance with the interface evolution (cf. [Bän01]). This explicit representation allows straightforward treatment of boundary conditions and discontinuities. In addition, it enables accurate computation of geometric quantities, especially when curved elements are used. Moving mesh approaches can also resolve small gaps between interfaces. Their drawbacks include the limited ability to handle large deformations and the difficulty of treating topological changes. Furthermore, mesh motion may lead to highly distorted or small elements, requiring remeshing to maintain acceptable mesh quality. To reduce the impact of these problems, one may use an arbitrary Lagrangian-Eulerian approach; see, e.g., [HLZ81; DGH82; FN99; FN04; Boi+11]. In these approaches, only the nodes on the interface are moved with the velocity of the phase while the rest of the mesh is moved with an independent velocity to reduce deformations of the mesh.

Front tracking methods In front tracking methods, an interface mesh is introduced that is independent of the background mesh, allowing the interface to cut through background elements in an arbitrary manner; see, e.g., [UT92; Try+01; BG14; BG17]. This increases flexibility compared with moving mesh methods and enables larger deformations while still permitting accurate computation of geometric quantities. However, large interface deformations still might require reparametrization or remeshing of the interface. Additionally, the handling of boundary or interface conditions in the governing equation becomes more involved. Moreover, surface integrals must be evaluated by exchanging information between the interface mesh and the background mesh. Extensions of the classical approach are discussed in [TSZ11], considering multi-physics settings with adaptive interface management, and in [Gli+98], developing front-tracking methods to treat topological changes.

2.3.2 Interface capturing methods

In contrast to interface tracking methods, interface capturing methods use indicator functions to describe the interface implicitly. Below, we briefly discuss the phase-field method, the volume-of-fluid method, and the level set method as three representatives of this class.

Phase-field method The phase-field method differs from the other approaches discussed here in that it regularizes the interface and introduces a smooth transition layer of thickness ε; see, e.g. [Jac01; Eck+09; Li+09]. This regularization smooths all involved variables, which is advantageous from both numerical and modeling

perspectives. In addition, the phase-field method is able to handle arbitrary domain deformations and topological changes; see, e.g., [Jam+99; PP01]. However, accurately resolving the diffuse interface layer requires sufficiently fine meshes or high-order approximations, which may result in large numbers of degrees of freedom and, consequently, large linear systems. A key advantage of the phase-field formulation is that no sharp interface needs to be tracked, allowing the use of standard discretization techniques. Its principal limitation is that error estimates deteriorate exponentially as ε^{-1}. For a more detailed explanation of the phase-field method we refer to [Ste09; DF20].

Volume-of-fluid method A second interface capturing method is the volume-of-fluid method introduced by Hirt and Nichols in [HN81]. A discontinuous indicator function $\psi : \Omega \times \mathbb{R}_+ \to [0, 1]$ is used to describe the volume fraction of one particular phase within a mesh element (see [HN81; SZ99]). Therefore, we have $\psi = 1$ when only this particular phase is present within a cell and $\psi = 0$ when the phase is not present. In mesh elements intersected by the interface we have $\psi \in (0, 1)$. Note that instead of giving a sharp description of the interface, this method identifies the cells intersected by the interface. Extensions of the method to handle topological changes and large deformations of the interface are available in the literature (cf. [WW00; SW08]).

Level set method In the level set method, introduced by Osher and Sethian (see [OS88; SSO94; AS95; Che+97; OF01; Set01; SS03; OF06]) and based on an idea published in [DT06], the interface is represented implicitly by a level set function $\phi : \Omega \times \mathbb{R}_+ \to \mathbb{R}$. Without loss of generality, we assume that $\Gamma(t)$ corresponds to the zero level set of $\phi(\cdot, t)$, that is, $\Gamma(t) = \{x \in \Omega : \phi(x, t) = 0\}$. The level set method is a flexible and widely used approach that can handle essentially arbitrary deformations and topological changes (see [SD98; Gib+07; TMB07]). On the other hand, accurate computations of geometric quantities and maintaining desirable properties such as volume conservation is challenging. For instance, the computation of mean curvature is not straightforward. However, different approaches to compute the mean curvature from a level set function have been developed (cf. [Hys06; Hys07; GR11; TK12; RE14]). In addition, recently developed extensions of the level set method can deal with conservation of volume; see, e.g., [Kee+11; Kuz14; QKK19; QHK20]. Implementing the level set method robustly requires care, as several algorithmic components must work consistently. For example, in many cases an approximate signed distance function (SDF) is needed in the context of level set algorithms. Even though many level set algorithms do not preserve the

signed distance property, various redistancing approaches to reconstruct an SDF are available in the literature; see, e.g., [BK13; Reu13; BK14; Bas17; BKS17].

Additionally, there exist hybrid methods combining the advantages of the different methods; see, e.g., [BW13; BW14]. Since every method has its own advantages and drawbacks, the optimal choice for the numerical interface handling depends on the application. For further details on the methods we refer to the literature, e.g., [DDE05; DE13; BS20; BGN20; DF20]. Whenever an interface treatment method is required in the remainder of this thesis, we employ the level set method.

3 Projected gradient stabilization in unfitted finite element methods for elliptic boundary value problems

Solving boundary value problems (BVPs) in complex geometries poses significant challenges. As discussed in Chapter 2, when using classical fitted finite element methods (FEMs), the computational mesh needs to be aligned with the boundary to ensure accuracy. The computational cost of constructing such a mesh increases with the complexity of the geometry, and the constructed mesh might contain elements that are either very small or exhibit a very acute angle. These possibly irregular meshes also add to the computational cost during the assembly of the matrices. Solving partial differential equations (PDEs) in time-dependent domains increases the computational cost even further. The displacement of the boundary requires a moving-mesh approach or remeshing at each time step to keep the mesh facets aligned with the boundary. To prevent the violation of essential mesh criteria, regular remeshing is also needed in the context of moving-mesh approaches. This frequent remeshing in fitted FEMs increases the complexity and computational costs and can lead to instabilities.

An effective alternative to fitted FEMs, overcoming these limitations through an implicit representation of the interface, is provided by unfitted FEMs. In contrast to fitted FEMs, these methods rely on a fixed mesh that remains unchanged throughout the computations, rather than aligning the mesh with the boundary. Different techniques, such as level sets or phase-field indicator functions, can be used to represent the boundary. This implicit treatment of the boundary within a fixed mesh eliminates the need for remeshing in time-dependent problems and allows us to use fixed meshes even for complex geometries.

Unfitted FEMs are particularly advantageous for PDEs in evolving domains; however, we restrict ourselves to the stationary problem. This restriction is motivated by the observation that the time discretization behaves analogously to that of other FEMs. By doing so, we eliminate temporal complexities and can focus on the spatial aspects and establish theoretical foundations. The elliptic BVP under consideration in a fictitious domain formulation reads as follows.

Let $\Omega \subset \mathbb{R}^d$, $d \in \{1, 2, 3\}$, be a bounded Lipschitz domain. Within Ω, let $\Omega_+ \subset \Omega$ represent a subdomain bounded by a smooth interface Γ, where Γ satisfies $\Gamma \cap \partial\Omega = \emptyset$ and has an outward-pointing unit normal vector denoted by $\mathbf{n}$. Find sufficiently smooth $u : \Omega_+ \to \mathbb{R}$ such that

$$-\Delta u = f \quad \text{in } \Omega_+, \tag{3.1a}$$
$$u = g \quad \text{on } \Gamma. \tag{3.1b}$$

Here, it is assumed that f and g are sufficiently smooth functions satisfying all necessary compatibility conditions (cf. [Eva10]).

The remainder of this chapter is structured as follows. In Section 3.1, we discretize the elliptic BVP using the unfitted Nitsche FEM. Section 3.2 introduces a stabilization term based on projected gradients; a detailed analysis is then provided in Section 3.3. A diffuse-interface variant of the method is proposed in Section 3.4 to overcome challenges related to the integration over sharp interfaces that are not resolved by the mesh. The chapter concludes with a discussion of numerical results in Section 3.5 and a high-order extension of the method in Section 3.6.

3.1 Unfitted Nitsche method

In this section, we construct a numerical scheme to solve the elliptic BVP (3.1). Therefore, we consider a conforming triangulation $\mathcal{T}_h$ of the domain Ω. For simplicity, we assume that the triangulation is fitted to the fictitious domain Ω, meaning that $\bigcup_{K \in \mathcal{T}_h} K = \overline{\Omega}$. Since the BVP is defined in $\Omega_+ \subset \Omega$ and not in Ω itself, this assumption does not impose any restriction.

For any $\delta > 0$, we define the subtriangulation $\mathcal{T}_h(\delta)$ consisting of all simplices that overlap with a δ-neighborhood of the subdomain Ω_+. This subtriangulation is given by

$$\mathcal{T}_h(\delta) = \{K \in \mathcal{T}_h \,:\, \exists\, \mathbf{x} \in K \text{ s.t. } \operatorname{dist}(\mathbf{x}, \Omega_+) \leq \delta\}.$$

Using this subtriangulation, we define the mesh-dependent domain

$$\Omega_{+,h}(\delta) = \operatorname{int}\left(\bigcup_{K \in \mathcal{T}_h(\delta)} K \right).$$

By definition, we have $\Omega_+ \subseteq \Omega_{+,h}(\delta)$ for all $\delta \geq 0$. For $\delta = 0$, the domain $\Omega_{+,h}(0)$ corresponds to the union of all simplices that have a nonempty intersection with the subdomain Ω_+, i.e., $\overline{\Omega_{+,h}(0)} = \bigcup_{K \cap \Omega_+ \neq \emptyset} K$.

We denote by $V_h(\delta)$ the finite element space consisting of piecewise affine functions associated with the subtriangulation $\mathcal{T}_h(\delta)$. This finite element space is formally defined as

$$V_h(\delta) = \{v_h \in C(\Omega_{+,h}(\delta)) : v_h|_K \in P_1(K) \ \forall K \in \mathcal{T}_h(\delta)\}.$$

Following [Nit71; BET11; Cho24], the standard Nitsche FEM for solving the elliptic BVP (3.1) reads as follows: Find $u_h \in V_h(0)$ such that

$$\begin{aligned}\int_{\Omega_+} \nabla u_h \cdot \nabla \phi_h \mathrm{d}\mathbf{x} - \int_\Gamma u_h \nabla \phi_h \cdot \mathbf{n} \mathrm{d}s - \int_\Gamma \phi_h \nabla u_h \cdot \mathbf{n} \mathrm{d}s + \int_\Gamma \alpha u_h \phi_h \mathrm{d}s \\ = \int_{\Omega_+} f\phi_h \mathrm{d}\mathbf{x} - \int_\Gamma g \nabla \phi_h \cdot \mathbf{n} \mathrm{d}s + \int_\Gamma \alpha g \phi_h \mathrm{d}s \quad \forall \phi_h \in V_h(0).\end{aligned} \tag{3.2}$$

Here, the interior penalty parameter $\alpha > 0$ is piecewise constant and depends on the local mesh size $h_K = \mathrm{diam}(K)$ for any simplex K in the triangulation $\mathcal{T}_h(\delta)$. The local parameter is given by $\alpha_K = \alpha_0 h_K^{-1}$, where α_0 is chosen to be sufficiently large and independent of the mesh size.

Remark 3.1. *The weak form* (3.2) *involves integration over cut cells. To evaluate these integrals numerically, there are different methods in the literature. These methods often involve the computation of coordinates and weights of quadrature points by means of moment-fitting (see, e.g., [MKO13; BSM20; GD22]) or an adaptive subcell integration (see, e.g., [Vog06; DH20]). On the other hand, a sufficiently smooth boundary can be approximated by a polygon that converges to the boundary with $O(h^2)$. Then the integrals can be calculated directly on the subcells.*

Using the bilinear form

$$a(u, \phi) = \int_{\Omega_+} \nabla u \cdot \nabla \phi \mathrm{d}\mathbf{x} - \int_\Gamma u \nabla \phi \cdot \mathbf{n} \mathrm{d}s - \int_\Gamma \phi \nabla u \cdot \mathbf{n} \mathrm{d}s + \int_\Gamma \alpha u \phi \mathrm{d}s \tag{3.3}$$

and the linear form

$$b(\phi) = \int_{\Omega_+} f\phi \mathrm{d}\mathbf{x} - \int_\Gamma g \nabla \phi \cdot \mathbf{n} \mathrm{d}s + \int_\Gamma \alpha g \phi \mathrm{d}s, \tag{3.4}$$

we can write (3.2) as the abstract problem

$$a(u_h, \phi_h) = b(\phi_h) \quad \forall \phi_h \in V_h(0). \tag{3.5}$$

3.2 Projected gradient stabilization

The finite element formulation (3.5) is theoretically well posed. However, it is prone to numerical instabilities arising from the presence of simplices in $\mathcal{T}_h(0)$ that intersect the physical domain Ω_+ only minimally. These small cut cells can affect both the stability and the accuracy of the numerical scheme. To address this issue, a ghost penalty (GP) stabilization technique was introduced in [Bur10]. A stabilization term mitigating the effects of the critical cut cells is added to simplices that are either directly adjacent to or intersected by the boundary Γ, leading to improved stability. In [LO19], the idea of GP stabilization is extended to a broader strip of elements. Instead of considering only the elements adjacent to Γ, this method incorporates all elements within a distance δ from the boundary of Ω_+. This provides a robust implicit extension in the context of Eulerian finite element discretizations, enhancing the handling of dynamic problems with evolving domains.

As an alternative to the GP stabilization, we introduce a stabilization technique based on projected gradients. This allows us to address both instabilities caused by small cut cells and the proper extension of u_h into $\Omega_{+,h}(\delta)$ for $\delta > 0$. For $u, \phi \in H^1(\Omega_{+,h}(\delta))$ we introduce the projected gradient (PG) stabilization term

$$s_h(u, \phi) = \int_{\Omega_{+,h}(\delta)} (\nabla u - \mathbf{g}(u)) \cdot \nabla \phi \mathrm{d}\mathbf{x}. \tag{3.6}$$

Here, $\mathbf{g}(u)$ represents the lumped-mass L^2 projection of the generally discontinuous gradient $\nabla u \in L^2(\Omega_{+,h}(\delta))$ into the finite element space $V_h(\delta)$.

Using the nodal basis of $V_h(\delta)$, we can compute $\mathbf{g}(u)$ locally. Denote by $\{\Psi_j\}_{j=1,\dots,N_h}$ the nodal basis in $V_h(\delta)$ with $N_h = \dim(V_h(\delta))$. Then we define

$$\mathbf{g}(u) = \sum_{j=1}^{N_h} \mathbf{g}_j(u) \Psi_j,$$

where the coefficients $\mathbf{g}_j(u)$ are computed as

$$\mathbf{g}_j(u) = \frac{\int_{\Omega_{+,h}(\delta)} \Psi_j \nabla u \mathrm{d}\mathbf{x}}{\int_{\Omega_{+,h}(\delta)} \Psi_j \mathrm{d}\mathbf{x}}. \tag{3.7}$$

Note that the computation of the coefficients involves integration only over elements sharing the node $\mathbf{x}_j$ where $\Psi_j(\mathbf{x}_j) = 1$. The algebraic structure of this stabilization term relies solely on gradient and lumped-mass matrices. This is discussed in greater detail in Remarks 3.3 and 3.5.

Adding this stabilization term to the abstract finite element formulation given in (3.5), we obtain the sharp-interface formulation: Find $u_h \in V_h(\delta)$ such that

$$a(u_h, \phi_h) + s_h(u_h, \phi_h) = b(\phi_h) \quad \forall \phi_h \in V_h(\delta). \tag{3.8}$$

Remark 3.2. *In finite element formulations for convection-dominated transport problems, projection-based stabilization terms of the form* (3.6) *are widely used to mitigate the numerical instabilities arising from convection terms (cf. [CB97; CB02; JKL06; JK10]). Consequently, the stabilizing effect of such terms can be naturally extended and used in applications involving convective terms.*

One main reason to apply stabilization globally rather than restricting it to a narrow band around the interface is its broader applicability and robustness. A global approach not only simplifies implementation by removing the need to determine whether an element lies within the narrow band, but also ensures uniform stability across the computational domain. Although GP stabilization in unfitted FEM is traditionally applied within a narrow region near the interface, global definitions of GPs have also been introduced in previous works (cf. [BCM15; MSW18]).

The recent report [OW25] highlights that a global formulation of GP stabilization is essential for ensuring specific stability properties when dealing with moving interfaces. This insight further supports the decision to adopt a global approach for stabilization in dynamic scenarios.

Remark 3.3 (Algebraic representation)**.** *To analyze the algebraic structure of the stabilization term, we consider the standard Lagrangian nodal basis in the finite element space. Let L represent the matrix corresponding to the bilinear form $(\nabla\cdot, \nabla\cdot)_{L^2(\Omega_{+,h}(\delta))}$.*

Similarly, B denotes the gradient matrix associated with the bilinear form

$$(\nabla v_h, \mathbf{w}_h)_{L^2(\Omega_{+,h}(\delta))}$$

with $v_h \in V_h(\delta), \mathbf{w}_h \in (V_h(\delta))^d$. Additionally, we define $\widetilde{M}$ as the lumped-mass matrix corresponding to the finite element space $(V_h(\delta))^d$.

The stabilization term $s_h(\cdot,\cdot)$, when expressed at the algebraic level, takes the form

$$L - B^T \widetilde{M}^{-1} B.$$

This formulation shows that, at the algebraic level, the stabilization term is represented as the difference between L, which represents a standard Laplacian discretization, and $B^T\widetilde{M}^{-1}B$, which corresponds to a mixed finite element discretization of the Laplacian operator.

3.3 Analysis of the projected gradient stabilization

Let us now conduct a detailed analysis of our unfitted FEM with PG stabilization and establish several of its properties. Since the PG stabilization for elliptic BVPs closely resembles the stabilization introduced in [OBK25] for elliptic interface problems, we follow the proof of stability and convergence of the unfitted FEM therein.

For this analysis, we assume that the mesh is shape regular and quasi-uniform and impose a constraint on the extension width δ. We require the extension width to adhere to the relation $\delta \leq Ch$, where C is a constant of order $O(1)$. For readability and to simplify notation, explicit references to δ will be omitted throughout this section when referring to extended domains and finite element spaces. This allows us to focus on core aspects of stability and convergence without unnecessary distractions by technical details. In subsequent calculations, we understand projections and inner products componentwise whenever the arguments involve vector fields.

Following (3.7), we define the lumped L^2 projection operator $\mathcal{P}_h : L^2(\Omega_{+,h}) \to V_h$, mapping functions $v \in L^2(\Omega_{+,h})$ into the finite element space V_h, as

$$\mathcal{P}_h v = \sum_{j=1}^{N_h} \mathrm{g}_j(\mathbf{v})\Psi_j, \qquad \mathrm{g}_j(v) = \frac{\int_{\Omega_{+,h}} v\Psi_j \mathrm{d}\mathbf{x}}{\int_{\Omega_{+,h}} \Psi_j \mathrm{d}\mathbf{x}}. \tag{3.9}$$

Then we can write the bilinear form (3.6) associated with the PG stabilization term as

$$s_h(u,v) = \int_{\Omega_{+,h}} (\nabla u - \mathcal{P}_h \nabla u) \cdot \nabla v \mathrm{d}\mathbf{x}, \quad u, v \in H^1(\Omega_{+,h}). \tag{3.10}$$

Remark 3.4. *A similar stabilization term was used in [Cod+23, Eq. (19)] to stabilize an unfitted FEM for the Navier–Stokes equations. The difference to* (3.10) *is that the lumped-mass L^2 projection operator $\mathcal{P}_h$ is replaced by a consistent-mass L^2 projection operator $\mathcal{P}_h^{cut}$ on a subdomain. However, no numerical analysis for that stabilization is available.*

To improve readability, we omit constants that are independent of the mesh size and the position of the interface within the mesh. If $a \leq cb$ holds with a constant c depending only on the shape regularity of the mesh, we denote this relation by $a \lesssim b$. To indicate that a and b are equivalent up to a multiplicative constant, we use the notation $a \simeq b$ when both relationships $a \lesssim b$ and $b \lesssim a$ are satisfied.

Before we proceed with the analysis of the stabilization, we introduce a lumped inner product and derive some identities involving the lumped L^2 projection $\mathcal{P}_h$.

Therefore, let $M = (m_{ij})_{i,j=1}^N$ denote the finite element mass matrix associated with the nodal basis of V_h. We define the lumped mass matrix $\widetilde{M}$ as the diagonal matrix where each diagonal entry is a row sum of the mass matrix M, i.e., $\widetilde{m}_{ii} = \sum_{j=1}^N m_{ij}$. For linear Lagrange elements, we find that $m_{ij} \geq 0$, and the definitions of M and $\widetilde{M}$ imply

$$\mathrm{w}^T(\widetilde{M} - M)\mathrm{w} = \sum_{i=1}^N \sum_{j=i+1}^N m_{ij}(\mathrm{w}_i - \mathrm{w}_j)^2 \qquad \forall \mathrm{w} \in \mathbb{R}^N. \tag{3.11}$$

Hence, the matrix $\widetilde{M} - M$ is positive semi-definite. For $w_h, v_h \in V_h$, we denote the corresponding coefficient vectors in the Lagrange basis of V_h as $\mathrm{w}, \mathrm{v} \in \mathbb{R}^N$. A result derived from (3.11), and widely recognized in the literature (cf. [BH08, Proposition 1]), is given by

$$\sum_{K \in \mathcal{T}_h} h_K^2 \left\|\nabla w_h\right\|_{0,K}^2 \lesssim \mathrm{w}^T(\widetilde{M} - M)\mathrm{w} \lesssim \sum_{K \in \mathcal{T}_h} h_K^2 \left\|\nabla w_h\right\|_{0,K}^2, \tag{3.12}$$

where $h_K = \operatorname{diam}(K)$ is the local mesh size.

We define a lumped L^2 inner product

$$(w_h, v_h)_\ell = \mathrm{w}^T \widetilde{M} \mathrm{v},$$

where w, v are the coefficient vectors corresponding to $w_h, v_h \in V_h$. For $w_h \in V_h$ and $g \in L^2(\Omega_{+,h})$ with $v_h = \mathcal{P}_h g$ we obtain

$$\begin{aligned}(w_h, \mathcal{P}_h g)_\ell = \mathrm{w}^T \widetilde{M} \mathrm{v} &= \sum_{i=1}^N \mathrm{w}_i \widetilde{m}_{ii} \mathrm{v}_i = \sum_{i=1}^N \mathrm{w}_i \left(\int_{\Omega_{+,h}} \Psi_i \mathrm{d}\mathbf{x} \right) \frac{\int_{\Omega_{+,h}} g \Psi_i \mathrm{d}\mathbf{x}}{\int_{\Omega_{+,h}} \Psi_i \mathrm{d}\mathbf{x}} \\ &= \int_{\Omega_{+,h}} \sum_{i=1}^N \mathrm{w}_i \Psi_i g \mathrm{d}\mathbf{x} = (w_h, g)_{0,\Omega_{+,h}}.\end{aligned}$$

This gives us the identity

$$(w_h, \mathcal{P}_h g)_\ell = (w_h, g)_{0,\Omega_{+,h}} \quad \forall w_h \in V_h,\ g \in L^2(\Omega_{+,h}). \tag{3.13}$$

Using this identity for the scalar components of $\mathbf{w}_h = \mathcal{P}_h \nabla v$ and $\mathbf{g} = \nabla u$ we derive

$$(\mathcal{P}_h \nabla v, \mathcal{P}_h \nabla u)_\ell = (\mathcal{P}_h \nabla v, \nabla u)_{0,\Omega_{+,h}}. \tag{3.14}$$

These last two identities play a crucial role in the proofs of the following lemmas.

Now we can proceed with the analysis of the PG stabilization. We start with the following result for the bilinear form of the PG stabilization.

Lemma 3.1. *The bilinear form $s_h(u,v)$ is symmetric and satisfies*

$$s_h(u,u) \simeq \|\nabla u - \mathcal{P}_h(\nabla u)\|^2_{0,\Omega_{+,h}} + h^2 \|\nabla \mathcal{P}_h(\nabla u)\|^2_{0,\Omega_{+,h}} \quad \forall\, u \in H^1(\Omega_{+,h}). \tag{3.15}$$

Proof. Using (3.14), we obtain for the bilinear form $s_h(u,v)$ of the stabilization

$$\begin{aligned} s_h(u,v) =& (\nabla u - \mathcal{P}_h \nabla u, \nabla v)_{0,\Omega_{+,h}} - (\nabla u - \mathcal{P}_h \nabla u, \mathcal{P}_h \nabla v)_{0,\Omega_{+,h}} \\ &+ (\nabla u - \mathcal{P}_h \nabla u, \mathcal{P}_h \nabla v)_{0,\Omega_{+,h}} \\ =& (\nabla u - \mathcal{P}_h \nabla u, \nabla v - \mathcal{P}_h \nabla v)_{0,\Omega_{+,h}} + (\nabla u - \mathcal{P}_h \nabla u, \mathcal{P}_h \nabla v)_{0,\Omega_{+,h}} \\ =& (\nabla u - \mathcal{P}_h \nabla u, \nabla v - \mathcal{P}_h \nabla v)_{0,\Omega_{+,h}} + (\mathcal{P}_h \nabla u, \mathcal{P}_h \nabla v)_{\ell} \\ &- (\mathcal{P}_h \nabla u, \mathcal{P}_h \nabla v)_{0,\Omega_{+,h}}. \end{aligned} \tag{3.16}$$

Then the symmetry follows directly since the right-hand side is symmetric.

To prove the equivalence stated in (3.15), we first establish the relationship between $(w_h, w_h)_\ell - (w_h, w_h)_{0,\Omega_{+,h}}$ and $h^2 \|\nabla w_h\|^2_{0,\Omega_{+,h}}$ for $w_h \in V_h$. Indeed, for any $w_h \in V_h$ we obtain

$$(w_h, w_h)_\ell - (w_h, w_h)_{0,\Omega_{+,h}} = \mathrm{w}^T \widetilde{M} \mathrm{w} - \mathrm{w}^T M \mathrm{w} = \mathrm{w}^T (\widetilde{M} - M) \mathrm{w}.$$

Using (3.12), along with the assumption of quasi-uniformity of the mesh, this simplifies to

$$(w_h, w_h)_\ell - (w_h, w_h)_{0,\Omega_{+,h}} = \mathrm{w}^T (\widetilde{M} - M) \mathrm{w} \simeq \sum_{K \in \mathcal{T}_h} h_K^2 \|\nabla w_h\|^2_{0,K}. \tag{3.17}$$

This shows the equivalence for $w_h \in V_h$. For $u \in H^1(\Omega_{+,h})$, we use the expression derived in (3.16) to represent the stabilization term as

$$\begin{aligned} s_h(u,u) =& (\nabla u - \mathcal{P}_h \nabla u, \nabla u - \mathcal{P}_h \nabla u)_{0,\Omega_{+,h}} + (\mathcal{P}_h \nabla u, \mathcal{P}_h \nabla u)_{\ell} \\ &- (\mathcal{P}_h \nabla u, \mathcal{P}_h \nabla u)_{0,\Omega_{+,h}}. \end{aligned}$$

Since $\mathcal{P}_h \nabla u$ belongs to the finite element space $(V_h)^d$, we can apply (3.17) componentwise and use the quasi-uniformity to estimate h_K by h. This allows us to prove the equivalence and conclude that the stabilization term satisfies the relationship given in (3.15). □

The symmetry of the bilinear form $s_h(\cdot,\cdot)$, combined with the equivalence established in (3.15), leads to the following result.

Corollary 3.2. *The bilinear form $s_h(\cdot,\cdot)$ induces a semi-inner product on the space $H^1(\Omega_{+,h})$.*

After analyzing the structure of the bilinear form $s_h(\cdot,\cdot)$ associated with the PG stabilization, we are now interested in the stability and approximation properties of the projection operator $\mathcal{P}_h$ as defined in (3.9). These properties are essential for understanding the behavior of $\mathcal{P}_h$ within the stabilization framework.

Lemma 3.3. *The projection $\mathcal{P}_h$ is stable in $L^2(\Omega_{+,h})$ and $H^1(\Omega_{+,h})$, i.e.,*

$$\|\mathcal{P}_h v\|_{0,\Omega_{+,h}} \lesssim \|v\|_{0,\Omega_{+,h}} \quad \text{and} \quad \|\nabla \mathcal{P}_h w\|_{0,\Omega_{+,h}} \lesssim \|\nabla w\|_{0,\Omega_{+,h}} \tag{3.18}$$

for any $v \in L^2(\Omega_{+,h})$, $w \in H^1(\Omega_{+,h})$. Furthermore,

$$\|v - \mathcal{P}_h v\|_{0,\Omega_{+,h}} \lesssim h \|\nabla v\|_{0,\Omega_{+,h}} \quad \forall\, v \in H^1(\Omega_{+,h}). \tag{3.19}$$

Proof. Since the consistent mass matrix M and the lumped mass matrix $\widetilde{M}$, as defined above, are spectrally equivalent (cf. [Wat87]), it follows that $\|w_h\|_\ell \simeq \|w_h\|_{0,\Omega_{+,h}}$ for any $w_h \in V_h$. Using this relationship for the projection operator $\mathcal{P}_h$, we derive

$$\|\mathcal{P}_h v\|^2_{0,\Omega_{+,h}} \lesssim \|\mathcal{P}_h v\|^2_\ell = (\mathcal{P}_h v, \mathcal{P}_h v)_\ell.$$

Choosing $w_h = \mathcal{P}_h v$ and $g = v$ in (3.13), and applying the Cauchy–Schwarz inequality, we obtain

$$(\mathcal{P}_h v, \mathcal{P}_h v)_\ell = (\mathcal{P}_h v, v)_{0,\Omega_{+,h}} \leq \|\mathcal{P}_h v\|_{0,\Omega_{+,h}} \|v\|_{0,\Omega_{+,h}}.$$

Consequently, this leads to

$$\|\mathcal{P}_h v\|^2_{0,\Omega_{+,h}} \lesssim \|\mathcal{P}_h v\|_{0,\Omega_{+,h}} \|v\|_{0,\Omega_{+,h}}.$$

This result proves the first inequality in (3.18).

In the next step, we establish the approximation result stated in (3.19). To this end, let us first assume that $v_h \in V_h \subset H^1(\Omega_{+,h})$. Denote by $\omega(\mathbf{x}_j)$ the domain consisting of all simplices sharing the grid node $\mathbf{x}_j$. Using the triangle inequality,

we estimate

$$\begin{aligned}
\|v_h - \mathcal{P}_h v_h\|^2_{0,\Omega_{+,h}} &= \left\| \sum_{j=1}^{N_h} v_h(\mathbf{x}_j)\Psi_j - \sum_{j=1}^{N_h} \Psi_j \frac{\int_{\omega(\mathbf{x}_j)} v_h \Psi_j \mathrm{d}\mathbf{x}}{\int_{\omega(\mathbf{x}_j)} \Psi_j \mathrm{d}\mathbf{x}} \right\|^2_{0,\Omega_{+,h}} \\
&= \left\| \sum_{j=1}^{N_h} \Psi_j \left(v_h(\mathbf{x}_j) - \frac{\int_{\omega(\mathbf{x}_j)} v_h \Psi_j \mathrm{d}\mathbf{x}}{\int_{\omega(\mathbf{x}_j)} \Psi_j \mathrm{d}\mathbf{x}} \right) \right\|^2_{0,\Omega_{+,h}} \\
&\leq \sum_{j=1}^{N_h} \left\| \Psi_j \left(v_h(\mathbf{x}_j) - \frac{\int_{\omega(\mathbf{x}_j)} v_h \Psi_j \mathrm{d}\mathbf{x}}{\int_{\omega(\mathbf{x}_j)} \Psi_j \mathrm{d}\mathbf{x}} \right) \right\|^2_{0,\Omega_{+,h}} \\
&= \sum_{j=1}^{N_h} \|\Psi_j\|^2_{0,\Omega_{+,h}} \left(v_h(\mathbf{x}_j) - \frac{\int_{\omega(\mathbf{x}_j)} v_h \Psi_j \mathrm{d}\mathbf{x}}{\int_{\omega(\mathbf{x}_j)} \Psi_j \mathrm{d}\mathbf{x}} \right)^2 .
\end{aligned}$$

Using the fact that $\|\Psi_j\|_{0,\omega(\mathbf{x}_j)} \simeq h^{d/2}$, we obtain

$$\begin{aligned}
\|v_h - \mathcal{P}_h v_h\|^2_{0,\Omega_{+,h}} &\leq \sum_{j=1}^{N_h} \|\Psi_j\|^2_{0,\Omega_{+,h}} \left(v_h(\mathbf{x}_j) - \frac{\int_{\omega(\mathbf{x}_j)} v_h \Psi_j \mathrm{d}\mathbf{x}}{\int_{\omega(\mathbf{x}_j)} \Psi_j \mathrm{d}\mathbf{x}} \right)^2 \\
&\simeq h^d \sum_{j=1}^{N_h} \left(v_h(\mathbf{x}_j) - \frac{\int_{\omega(\mathbf{x}_j)} v_h \Psi_j \mathrm{d}\mathbf{x}}{\int_{\omega(\mathbf{x}_j)} \Psi_j \mathrm{d}\mathbf{x}} \right)^2 \\
&= h^d \sum_{j=1}^{N_h} \frac{1}{\left(\int_{\omega(\mathbf{x}_j)} \Psi_j \mathrm{d}\mathbf{x} \right)^2} \left(v_h(\mathbf{x}_j) \int_{\omega(\mathbf{x}_j)} \Psi_j \mathrm{d}\mathbf{x} - \int_{\omega(\mathbf{x}_j)} v_h \Psi_j \mathrm{d}\mathbf{x} \right)^2 .
\end{aligned}$$

We conclude

$$\|v_h - \mathcal{P}_h v_h\|^2_{0,\Omega_{+,h}} \lesssim h^{-d} \sum_{j=1}^{N_h} \left(\int_{\omega(\mathbf{x}_j)} v_h \Psi_j \mathrm{d}\mathbf{x} - v_h(\mathbf{x}_j) \int_{\omega(\mathbf{x}_j)} \Psi_j \mathrm{d}\mathbf{x} \right)^2 \tag{3.20}$$

with the equivalence $\int_{\omega(\mathbf{x}_j)} \Psi_j \mathrm{d}\mathbf{x} \simeq h^d$ due to the assumption of a quasi-uniform mesh. To estimate the above terms, we consider each simplex $K \in \mathcal{T}_h$. Using a transformation to a reference triangle, we estimate for any $K \in \mathcal{T}_h$ and a grid node

$\mathbf{x}_j \in K$

$$\begin{aligned}\Big|\int_K v_h\Psi_j \mathrm{d}\mathbf{x} - v_h(\mathbf{x}_j)\int_K \Psi_j \mathrm{d}\mathbf{x}\Big| &= \Big|\int_K \left(\sum_{i=1}^{N_h} v_h(\mathbf{x}_i)\Psi_i\right)\Psi_j - v_h(\mathbf{x}_j)\Psi_j \mathrm{d}\mathbf{x}\Big| \\ &\lesssim \Big|h^d \int_{\hat{K}} \left(\sum_{i=1}^{N_h} v_h(\mathbf{x}_i)\hat{\Psi}_i\right)\hat{\Psi}_j - v_h(\mathbf{x}_j)\hat{\Psi}_j \mathrm{d}\mathbf{x}\Big|,\end{aligned}$$

where $\hat{\Psi}_j$ is the basis function on the reference triangle corresponding to the global physical basis function Ψ_j. Using the Cauchy–Schwarz inequality and a norm equivalence on the finite-dimensional space $P^1(\hat{K})$ we derive

$$\begin{aligned}\Big|\int_K v_h\Psi_j \mathrm{d}\mathbf{x} - v_h(\mathbf{x}_j)\int_K \Psi_j \mathrm{d}\mathbf{x}\Big| &\lesssim h^d \left\|\sum_{i=1}^{N_h} v_h(\mathbf{x}_i)\hat{\Psi}_i - v_h(\mathbf{x}_j)\right\|_{0,\hat{K}} \left\|\hat{\Psi}_j\right\|_{0,\hat{K}} \\ &\simeq h^d \left\|\sum_{i=1}^{N_h} v_h(\mathbf{x}_i)\nabla\hat{\Psi}_i\right\|_{0,\hat{K}} \left\|\hat{\Psi}_j\right\|_{0,\hat{K}}.\end{aligned}$$

Using a subsequent transformation to the physical element, we conclude

$$\Big|\int_K v_h\Psi_j \mathrm{d}\mathbf{x} - v_h(\mathbf{x}_j)\int_K \Psi_j \mathrm{d}\mathbf{x}\Big| \lesssim h \left\|\nabla v_h\right\|_{0,K} \left\|\Psi_j\right\|_{0,K}.$$

By summation over all simplices in $\omega(\mathbf{x}_j)$, we obtain with the triangle inequality

$$\begin{aligned}\Big|\int_{\omega(\mathbf{x}_j)} v_h\Psi_j \mathrm{d}\mathbf{x} - v_h(\mathbf{x}_j)\int_{\omega(\mathbf{x}_j)} \Psi_j \mathrm{d}\mathbf{x}\Big| &= \Big|\sum_{K\subset\omega(\mathbf{x}_j)} \int_K v_h\Psi_j \mathrm{d}\mathbf{x} - v_h(\mathbf{x}_j)\int_K \Psi_j \mathrm{d}\mathbf{x}\Big| \\ &\leq \sum_{K\subset\omega(\mathbf{x}_j)} \Big|\int_K v_h\Psi_j \mathrm{d}\mathbf{x} - v_h(\mathbf{x}_j)\int_K \Psi_j \mathrm{d}\mathbf{x}\Big| \\ &\lesssim \sum_{K\subset\omega(\mathbf{x}_j)} h \left\|\nabla v_h\right\|_{0,K} \left\|\Psi_j\right\|_{0,K} \\ &\lesssim h^{d/2+1} \left\|\nabla v_h\right\|_{0,\omega(\mathbf{x}_j)}.\end{aligned}$$

Substituting this result into the right-hand side of (3.20) yields

$$\begin{aligned}\left\|v_h - \mathcal{P}_h v_h\right\|^2_{0,\Omega_{+,h}} &\lesssim h^{-d} \sum_{j=1}^{N_h} \left(h^{d/2+1} \left\|\nabla v_h\right\|_{0,\omega(\mathbf{x}_j)}\right)^2 \\ &= h^2 \sum_{j=1}^{N_h} \left\|\nabla v_h\right\|^2_{0,\omega(\mathbf{x}_j)} \lesssim h^2 \left\|\nabla v_h\right\|^2_{0,\Omega_{+,h}}\end{aligned}$$

and establishes (3.19) for $v_h \in V_h$. To extend the approximation result (3.19) to arbitrary $v \in H^1(\Omega_{+,h})$, we consider the L^2-orthogonal projection $\mathcal{Q}_h v \in V_h$. Applying the triangle inequality, we obtain

$$\|v - \mathcal{P}_h v\|_{0,\Omega_{+,h}} \leq \|\mathcal{P}_h(\mathcal{Q}_h v - v)\|_{0,\Omega_{+,h}} + \|\mathcal{P}_h(\mathcal{Q}_h v) - \mathcal{Q}_h v\|_{0,\Omega_{+,h}} + \|v - \mathcal{Q}_h v\|_{0,\Omega_{+,h}}.$$

Leveraging the L^2 stability of the operator $\mathcal{P}_h$, together with the approximation property in (3.19) for functions in V_h, we estimate

$$\begin{aligned}\|v - \mathcal{P}_h v\|_{0,\Omega_{+,h}} &\leq \|\mathcal{P}_h(\mathcal{Q}_h v - v)\|_{0,\Omega_{+,h}} + \|\mathcal{P}_h(\mathcal{Q}_h v) - \mathcal{Q}_h v\|_{0,\Omega_{+,h}} + \|v - \mathcal{Q}_h v\|_{0,\Omega_{+,h}} \\ &\lesssim \|\mathcal{Q}_h v - v\|_{0,\Omega_{+,h}} + h\|\nabla \mathcal{Q}_h v\|_{0,\Omega_{+,h}} + \|v - \mathcal{Q}_h v\|_{0,\Omega_{+,h}}.\end{aligned}$$

Additionally, we use the H^1 stability and approximation properties of the L^2-orthogonal projection on quasi-uniform meshes (see [BS02; Cia02; EG04]) to show that the right-hand side is bounded by $h\|\nabla v\|_{0,\Omega_{+,h}}$. This proves that the approximation result given in (3.19) holds for all functions $v \in H^1(\Omega_{+,h})$.

To derive the second estimate in (3.18), we apply the triangle inequality in conjunction with the finite element inverse inequality (cf. [BCM15; EG21])

$$\|\nabla v_h\|_{0,K} \lesssim h^{-1}\|v_h\|_{0,K} \quad \forall v_h \in V_h, K \in \mathcal{T}_h, \tag{3.21}$$

to obtain

$$\begin{aligned}\|\nabla \mathcal{P}_h v\|_{0,\Omega_{+,h}} &\leq \|\nabla(\mathcal{P}_h v - \mathcal{Q}_h v)\|_{0,\Omega_{+,h}} + \|\nabla \mathcal{Q}_h v\|_{0,\Omega_{+,h}} \\ &\lesssim h^{-1}\|\mathcal{P}_h v - \mathcal{Q}_h v\|_{0,\Omega_{+,h}} + \|\nabla \mathcal{Q}_h v\|_{0,\Omega_{+,h}}.\end{aligned}$$

Using the H^1 stability of the L^2-orthogonal projection $\mathcal{Q}_h$ and again the triangle inequality we deduce

$$\begin{aligned}\|\nabla \mathcal{P}_h v\|_{0,\Omega_{+,h}} &\lesssim h^{-1}\|\mathcal{P}_h v - \mathcal{Q}_h v\|_{0,\Omega_{+,h}} + \|\nabla \mathcal{Q}_h v\|_{0,\Omega_{+,h}} \\ &\lesssim h^{-1}\|\mathcal{P}_h v - \mathcal{Q}_h v\|_{0,\Omega_{+,h}} + \|\nabla v\|_{0,\Omega_{+,h}} \\ &\lesssim h^{-1}\|\mathcal{P}_h v - v\|_{0,\Omega_{+,h}} + h^{-1}\|v - \mathcal{Q}_h v\|_{0,\Omega_{+,h}} + \|\nabla v\|_{0,\Omega_{+,h}}.\end{aligned}$$

Finally, with the approximation property (3.19) and the approximation property of $\mathcal{Q}_h$, we conclude

$$\begin{aligned}\|\nabla \mathcal{P}_h v\|_{0,\Omega_{+,h}} &\lesssim h^{-1}\|\mathcal{P}_h v - v\|_{0,\Omega_{+,h}} + h^{-1}\|v - \mathcal{Q}_h v\|_{0,\Omega_{+,h}} + \|\nabla v\|_{0,\Omega_{+,h}} \\ &\lesssim \|\nabla v\|_{0,\Omega_{+,h}}.\end{aligned}$$

□

In the next step, we localize the stabilization term to element patches. Let $\mathcal{F}_h$ denote the set of internal facets of the triangulation $\mathcal{T}_h$, and denote by $\omega(f) = K \cup K'$ the union of the two simplices K and K' that share a facet $f \in \mathcal{F}_h$. Using $h_f = \max\{h_K, h_{K'}\}$ as the local mesh size associated with the patch, we define the localized stabilization term

$$s_h^f(u,v) = \int_{\omega(f)} [(\nabla u - \mathcal{P}_h \nabla u) \cdot (\nabla v - \mathcal{P}_h \nabla v)] \mathrm{d}\mathbf{x} + h_f^2 \int_{\omega(f)} (\nabla \mathcal{P}_h \nabla u) : (\nabla \mathcal{P}_h \nabla v) \mathrm{d}\mathbf{x}.$$

By summing these localized stabilization terms over all facets $f \in \mathcal{F}_h$, and using (3.15), we obtain

$$s_h(u,u) \simeq \sum_{f \in \mathcal{F}_h} s_h^f(u,u) \quad \forall\, u \in H^1(\Omega_{+,h}). \tag{3.22}$$

We are now ready to prove a key technical result.

Lemma 3.4. *For arbitrary $K_1, K_2 \in \mathcal{T}_h$ such that $K_1 \cup K_2 = \omega(f)$ for a facet $f \in \mathcal{F}_h$, it holds*

$$\|\nabla u\|_{0,K_2}^2 \lesssim \|\nabla u\|_{0,K_1}^2 + s_h^f(u,u) \quad \forall\, u \in H^1(\Omega_{+,h}), \tag{3.23}$$

$$\|u_h\|_{0,K_2}^2 \lesssim \|u_h\|_{0,K_1}^2 + h^2 s_h^f(u_h,u_h) \quad \forall\, u_h \in V_h. \tag{3.24}$$

Proof. The triangle inequality implies

$$\|\nabla u\|_{0,K_2} \leq \|\nabla u - \mathcal{P}_h \nabla u\|_{0,K_2} + \|\mathcal{P}_h \nabla u\|_{0,K_2}. \tag{3.25}$$

Let $\mathbf{w}_h = \mathcal{P}_h \nabla u \in (V_h)^d$. To estimate the second term on the right-hand side of (3.25), we utilize Friedrichs' inequality (cf. [HH02])

$$\|v\|_{1,K_i} \lesssim h_{K_i} \|\nabla v\|_{0,K_i} + \sqrt{h_{K_i}} \|v\|_{0,f} \quad \forall v \in H^1(K_i), i = 1,2 \tag{3.26}$$

and Young's inequality. This yields

$$\|\mathcal{P}_h \nabla u\|_{0,K_2}^2 = \|\mathbf{w}_h\|_{0,K_2}^2 \leq \|\mathbf{w}_h\|_{1,K_2}^2 \lesssim h_{K_2}^2 \|\nabla \mathbf{w}_h\|_{0,K_2}^2 + h_f \|\mathbf{w}_h\|_{0,f}^2.$$

Next, employing the finite element trace inequality (cf. [BH12; PE12; BCM15; EG21])

$$\|v_h\|_{0,\partial K} \lesssim \sqrt{h_K} \|\nabla v_h\|_{0,K} + \left(\sqrt{h_K}\right)^{-1} \|v_h\|_{0,K} \quad \forall v_h \in V_h, K \in \mathcal{T}_h, \tag{3.27}$$

and applying Young's inequality again, we obtain

$$\begin{aligned}\|\mathcal{P}_h \nabla u\|^2_{0,K_2} &\lesssim h^2_{K_2} \|\nabla \mathbf{w}_h\|^2_{0,K_2} + h_f \|\mathbf{w}_h\|^2_{0,f} \\ &\lesssim h^2_{K_2} \|\nabla \mathbf{w}_h\|^2_{0,K_2} + h^2_{K_1} \|\nabla \mathbf{w}_h\|^2_{0,K_1} + \|\mathbf{w}_h\|^2_{0,K_1} .\end{aligned}$$

Using the L^2 stability of $\mathcal{P}_h$, we further estimate

$$\begin{aligned}\|\mathcal{P}_h \nabla u\|^2_{0,K_2} &\lesssim h^2_{K_2} \|\nabla \mathbf{w}_h\|^2_{0,K_2} + h^2_{K_1} \|\nabla \mathbf{w}_h\|^2_{0,K_1} + \|\mathbf{w}_h\|^2_{0,K_1} \\ &\lesssim h^2_f \|\nabla \mathcal{P}_h \nabla u\|^2_{\omega(f)} + \|\nabla u\|^2_{0,K_1} .\end{aligned}$$

Throughout these estimates, we use the quasi-uniformity of the mesh to relate h_{K_1}, h_{K_2}, and h_f to one another. Together with (3.25) and the definition of $s^f_h(\cdot,\cdot)$ this proves the result claimed in (3.23).

To prove (3.24), we begin by applying Friedrichs' inequality (3.26) to estimate

$$\|u_h\|^2_{0,K_2} \lesssim h^2_{K_2} \|\nabla u_h\|^2_{0,K_2} + h_f \|u_h\|^2_{0,f} .$$

Using (3.23), this leads to

$$\begin{aligned}\|u_h\|^2_{0,K_2} &\lesssim h^2_{K_2} \|\nabla u_h\|^2_{0,K_2} + h_f \|u_h\|^2_{0,f} \\ &\lesssim h^2_{K_2} (\|\nabla u_h\|^2_{0,K_1} + s^f_h(u_h,u_h)) + h_f \|u_h\|^2_{0,f} .\end{aligned}$$

Next, using the finite element trace inequality (3.27), we refine the estimate to conclude

$$\begin{aligned}\|u_h\|^2_{0,K_2} &\lesssim h^2_{K_2} (\|\nabla u_h\|^2_{0,K_1} + s^f_h(u_h,u_h)) + h_f \|u_h\|^2_{0,f} \\ &\lesssim h^2_{K_2} s^f_h(u_h,u_h) + h^2_{K_1} \|\nabla u_h\|^2_{0,K_1} + \|u_h\|^2_{0,K_1} .\end{aligned}$$

Finally, employing the finite element inverse inequality (3.21) we obtain

$$\begin{aligned}\|u_h\|^2_{0,K_2} &\lesssim h^2_{K_2} s^f_h(u_h,u_h) + h^2_{K_1} \|\nabla u_h\|^2_{0,K_1} + \|u_h\|^2_{0,K_1} \\ &\lesssim h^2_{K_2} s^f_h(u_h,u_h) + \|u_h\|^2_{0,K_1} ,\end{aligned}$$

which completes the proof of the lemma. □

Recall that the mesh-dependent domain $\Omega_{+,h}$ includes simplices that are entirely contained within $\overline{\Omega}_+$, as well as layers of simplices $K \not\subset \overline{\Omega}_+$ that intersect the δ-neighborhood of Γ. Since we assumed that the extension width parameter δ is bounded by Ch, we conclude that the number of such layers is finite and independent

of the mesh size h. In [LO19] it is shown that, due to the smoothness of $\partial\Omega$ and the regularity of the mesh, any simplex $K \in \mathcal{T}_h$ with $K \subset \Omega_{+,h}$ can be reached from a simplex strictly within Ω_+ by traversing a finite number of facets. Additionally, the number of pathways to K originating from any interior simplex is uniformly bounded. Using these observations together with estimates (3.22) and (3.23), we obtain the coercivity result

$$\|\nabla u\|^2_{0,\Omega_{+,h}} \lesssim \|\nabla u\|^2_{0,\Omega_+} + s_h(u,u) \quad \forall u \in H^1(\Omega_{+,h}). \tag{3.28}$$

This result is crucial for conducting stability and error analyses associated with our unfitted finite element formulation. Additionally, the estimate provided in (3.24) proves to be a valuable tool for the analysis of problems with evolving interfaces; however, this specific application lies beyond the scope of this thesis.

Next, we turn our attention to the analysis of consistency. The consistency properties of both the elliptic portion and Nitsche terms within our finite element formulation are well established in the literature (cf. [Nit71; LT08; BH12]). Hence, our focus will primarily be on investigating the new stabilization–extension term.

In the following step, we prove key results regarding the continuity and consistency of the PG stabilization.

Lemma 3.5. *We have*

$$s_h(u,v) \lesssim \|u\|_{1,\Omega_{+,h}} \|v\|_{1,\Omega_{+,h}} \quad \forall\, u, v \in H^1(\Omega_{+,h}), \tag{3.29}$$

$$s_h(u,u) \lesssim h^2 \|u\|^2_{2,\Omega_{+,h}} \quad \forall\, u \in H^2(\Omega_{+,h}). \tag{3.30}$$

Proof. By employing the Cauchy–Schwarz inequality and the triangle inequality, we derive the estimate

$$\begin{aligned} s_h(u,v) &= \int_{\Omega_{+,h}} (\nabla u - \mathcal{P}_h \nabla u) \cdot \nabla v \mathrm{d}\mathbf{x} \leq \|\nabla u - \mathcal{P}_h \nabla u\|_{0,\Omega_{+,h}} \|\nabla v\|_{0,\Omega_{+,h}} \\ &\leq (\|\nabla u\|_{0,\Omega_{+,h}} + \|\mathcal{P}_h \nabla u\|_{0,\Omega_{+,h}}) \|\nabla v\|_{0,\Omega_{+,h}} . \end{aligned}$$

Using the L^2 stability of the projection operator $\mathcal{P}_h$ (cf. Lemma 3.3) we obtain

$$\begin{aligned} s_h(u,v) &\leq (\|\nabla u\|_{0,\Omega_{+,h}} + \|\mathcal{P}_h \nabla u\|_{0,\Omega_{+,h}}) \|\nabla v\|_{0,\Omega_{+,h}} \lesssim \|\nabla u\|_{0,\Omega_{+,h}} \|\nabla v\|_{0,\Omega_{+,h}} \\ &\leq \|u\|_{1,\Omega_{+,h}} \|v\|_{1,\Omega_{+,h}} . \end{aligned}$$

This is the continuity estimate given in (3.29). Leveraging (3.15), the H^1 stability of the projection operator $\mathcal{P}_h$, and the approximation property given by (3.19), we establish the consistency result in (3.30). Indeed, we have

$$\begin{aligned} s_h(u,u) &\lesssim \|\nabla u - \mathcal{P}_h(\nabla u)\|^2_{0,\Omega_{+,h}} + h^2 \|\nabla \mathcal{P}_h(\nabla u)\|^2_{0,\Omega_{+,h}} \lesssim h^2 \left\|\nabla^2 u\right\|^2_{0,\Omega_{+,h}} \\ &\leq h^2 \|u\|^2_{2,\Omega_{+,h}}. \end{aligned}$$

□

To formulate a convergence result, we define the norm

$$\|v\|^2_* = \|v\|^2_{1,\Omega_{+,h}} + h^{-1} \|v\|^2_{0,\Gamma} + s_h(v,v)$$

for $v \in H^1(\Omega_{+,h})$. This norm incorporates contributions from both the bulk and boundary terms, as well as the stabilization term $s_h(v,v)$.

Given a function $u \in H^1(\Omega_+)$, there exists a bounded linear operator $\mathcal{E} : H^1(\Omega_+) \to H^1(\mathbb{R}^d)$ extending u to a function $\mathcal{E}u \in H^1(\mathbb{R}^d)$. Furthermore, this operator is also bounded when considered as an operator from $H^2(\Omega_+)$ to $H^2(\mathbb{R}^d)$, as shown in [Ste71]. For simplicity, and whenever no ambiguity arises, we will identify the function u with its extension $\mathcal{E}u$ over the entire domain Ω.

The following theorem establishes our main convergence result.

Theorem 3.6. *Let $u \in H^2(\Omega_+)$ be a solution of (3.1). We associate u with its extension $\mathcal{E}u$. Assume $\delta \lesssim h$ for the extension width δ. Let u_h be a solution to (3.8) with sufficiently large α_0. Then*

$$\|u - u_h\|_* \lesssim h \|u\|_{2,\Omega_+}, \tag{3.31}$$

$$\|u - u_h\|_{0,\Omega_+} \lesssim h^2 \|u\|_{2,\Omega_+}. \tag{3.32}$$

Proof. Let I_h denote the nodal interpolation operator for $\Omega_{+,h}$, i.e., $I_h(u) \in V_h$. Utilizing the coercivity property (3.28), standard arguments (see, e.g., [HH02; BH12; BCM15]) can be applied to verify that the bilinear form

$$A_h(u,v) := a(u,v) + s_h(u,v)$$

is uniformly coercive for α_0 sufficiently large and that the bilinear form $a(\cdot,\cdot)$ is continuous on the finite element space with respect to the norm $\|\cdot\|_*$. Specifically,

$A_h(v_h, v_h) \gtrsim \|v_h\|_*^2$ for all $v_h \in V_h$ and $a(u_h, v_h) \lesssim \|u_h\|_* \|v_h\|_*$ for all $u_h, v_h \in V_h$. Therefore, we derive the estimate

$$\begin{aligned}
\|I_h(u) - u_h\|_*^2 \lesssim & A_h(I_h(u) - u_h, I_h(u) - u_h) \\
= & A_h(I_h(u), I_h(u) - u_h) - A_h(u_h, I_h(u) - u_h) \\
= & A_h(I_h(u), I_h(u) - u_h) - (a(u_h, I_h(u) - u_h) \\
& + s_h(u_h, I_h(u) - u_h)) \\
= & A_h(I_h(u), I_h(u) - u_h) - b(I_h(u) - u_h) \\
= & A_h(I_h(u), I_h(u) - u_h) - a(u, I_h(u) - u_h) \\
& - s_h(u, I_h(u) - u_h) + s_h(u, I_h(u) - u_h) \\
= & A_h(I_h(u), I_h(u) - u_h) - A_h(u, I_h(u) - u_h) \\
& + s_h(u, I_h(u) - u_h) \\
= & A_h(I_h(u) - u, I_h(u) - u_h) + s_h(u, I_h(u) - u_h) \\
= & a(I_h(u) - u, I_h(u) - u_h) + s_h(I_h(u) - u, I_h(u) - u_h) \\
& + s_h(u, I_h(u) - u_h),
\end{aligned} \tag{3.33}$$

where we use the fact that u_h solves (3.8) and u is a solution of (3.1). Let us now estimate the terms on the right-hand side of (3.33). In the first term we have by the continuity of the bilinear form $a(\cdot, \cdot)$

$$a(I_h(u) - u, I_h(u) - u_h) \lesssim \|I_h(u) - u\|_* \|I_h(u) - u_h\|_* .$$

Using the interpolation error estimate (cf., e.g., [BH12, Lemma 5] combined with Lemma 3.5)

$$\|I_h(u) - u\|_* \lesssim h \|\mathcal{E}u\|_{2,\Omega_{+,h}} \tag{3.34}$$

and the H^2 boundedness of the extension operator $\mathcal{E}$, which ensures $\|\mathcal{E}u\|_{2,\Omega_{+,h}} \lesssim \|u\|_{2,\Omega_+}$, we obtain

$$\begin{aligned}
a(I_h(u) - u, I_h(u) - u_h) &\lesssim h \|\mathcal{E}u\|_{2,\Omega_{+,h}} \|I_h(u) - u_h\|_* \\
&\lesssim h \|u\|_{2,\Omega_+} \|I_h(u) - u_h\|_* .
\end{aligned} \tag{3.35}$$

For the second term in (3.33), we use the continuity property of $s_h(\cdot, \cdot)$ as given by (3.29). We estimate

$$s_h(I_h(u) - u, I_h(u) - u_h) \lesssim \|I_h(u) - u\|_{1,\Omega_{+,h}} \|I_h(u) - u_h\|_{1,\Omega_{+,h}} .$$

By definition of the norm $\|\cdot\|_*$ and using similar arguments as for the first term, we conclude for the second term

$$\begin{aligned} s_h(I_h(u)-u, I_h(u)-u_h) &\lesssim \|I_h(u)-u\|_* \|I_h(u)-u_h\|_* \\ &\lesssim h\,\|u\|_{2,\Omega_+} \|I_h(u)-u_h\|_* . \end{aligned} \tag{3.36}$$

We use Corollary 3.2 to apply the Cauchy–Schwarz inequality in the third term on the right-hand side in (3.33). This yields

$$s_h(u, I_h(u)-u_h) \lesssim s_h^{1/2}(u,u) s_h^{1/2}(I_h(u)-u_h, I_h(u)-u_h). \tag{3.37}$$

Using the continuity property (3.29) of $s_h(\cdot,\cdot)$ and the definition of the norm $\|\cdot\|_*$, we estimate

$$s_h^{1/2}(I_h(u)-u_h, I_h(u)-u_h) \lesssim \|I_h(u)-u_h\|_{1,\Omega_{+,h}} \lesssim \|I_h(u)-u_h\|_* . \tag{3.38}$$

Furthermore, leveraging the consistency property (3.30) and the H^2 boundedness of the extension operator $\mathcal{E}$, we find

$$s_h^{1/2}(u,u) \lesssim h\,\|u\|_{2,\Omega_+} . \tag{3.39}$$

Substituting (3.38) and (3.39) into (3.37), we obtain

$$s_h(u, I_h(u)-u_h) \lesssim h\,\|u\|_{2,\Omega_+} \|I_h(u)-u_h\|_* . \tag{3.40}$$

Collecting all results from (3.33), (3.35), (3.36), and (3.40), we conclude

$$\|I_h(u)-u_h\|_*^2 \lesssim h\,\|u\|_{2,\Omega_+} \|I_h(u)-u_h\|_* .$$

The triangle inequality, together with this estimate, the interpolation error estimate (3.34), and the H^2 boundedness of the extension operator, yields

$$\|u-u_h\|_* \le \|u-I_h(u)\|_* + \|I_h(u)-u_h\|_* \lesssim h\,\|u\|_{2,\Omega_+} .$$

This proves (3.31).

To prove (3.32), we now employ a duality argument. Let z be the solution of the dual problem

$$\begin{aligned} -\Delta z &= u-u_h && \text{in } \Omega_+, \\ z &= 0 && \text{on } \Gamma. \end{aligned} \tag{3.41}$$

It is well known (cf. [Eva10, 6.3.2. Thm. 4]) that $z \in H^2(\Omega_+)$ and the stability estimate

$$\|z\|_{2,\Omega_+} \lesssim \|u - u_h\|_{0,\Omega_+} \tag{3.42}$$

holds. By $I_h(z)$ we denote the nodal interpolant of z, where z may be extended to the entire domain Ω if necessary. The interpolation operator I_h possesses standard approximation properties, which will be used in the subsequent steps of the proof.

To proceed, we multiply the first equation in (3.41) by $u - u_h$ and integrate by parts. This yields

$$\|u - u_h\|^2_{0,\Omega_+} = a(z, u - u_h). \tag{3.43}$$

Since u is the solution of the continuous problem (3.1), and u_h is the solution of the discrete problem (3.8), we have

$$b(I_h(z)) = a(u, I_h(z)),$$

and

$$b(I_h(z)) = a(u_h, I_h(z)) + s_h(u_h, I_h(z)).$$

By subtracting the last equation from the previous one, we obtain

$$0 = a(u - u_h, I_h(z)) - s_h(u_h, I_h(z)).$$

Substituting this result into (3.43), yields

$$\|u - u_h\|^2_{0,\Omega_+} = a(u - u_h, z - I_h(z)) + s_h(u_h, I_h(z)). \tag{3.44}$$

For the first term on the right-hand side of (3.44), we use the continuity property of $a(\cdot, \cdot)$, which gives

$$a(u - u_h, z - I_h(z)) \lesssim \|u - u_h\|_* \|z - I_h(z)\|_* .$$

Next, we apply the interpolation error estimate for $I_h(z)$. Using this and the H^2 boundedness of the extension operator $\mathcal{E}$, we find

$$\|z - I_h(z)\|_* \lesssim h \|\mathcal{E}z\|_{2,\Omega_{+,h}} \lesssim h \|z\|_{2,\Omega_+} .$$

Substituting this into the previous inequality and using the stability result (3.42) yields

$$a(u - u_h, z - I_h(z)) \lesssim h \|u - u_h\|_* \|u - u_h\|_{0,\Omega_+} . \tag{3.45}$$

For the second term on the right-hand side of (3.44) we use the Cauchy–Schwarz inequality to obtain

$$s_h(u_h, I_h(z)) \lesssim s_h^{1/2}(u_h, u_h) s_h^{1/2}(I_h(z), I_h(z)). \tag{3.46}$$

Using the triangle inequality, (3.29), and (3.30) we estimate

$$s_h^{1/2}(u_h,u_h) \lesssim s_h^{1/2}(u-u_h,u-u_h) + s_h^{1/2}(u,u) \lesssim \|u-u_h\|_{1,\Omega_{+,h}} + h\,\|\mathcal{E}u\|_{2,\Omega_{+,h}}\,.$$

The H^2 boundedness of the extension operator $\mathcal{E}$ and the definition of the $\|\cdot\|_*$ norm yield

$$s_h^{1/2}(u_h,u_h) \lesssim \|u-u_h\|_* + h\,\|u\|_{2,\Omega_+}\,. \tag{3.47}$$

Using the same arguments as before, we estimate

$$s_h^{1/2}(I_h(z),I_h(z)) \lesssim s_h^{1/2}(I_h(z)-z,I_h(z)-z)+s_h^{1/2}(z,z) \lesssim \|I_h(z)-z\|_{1,\Omega_{+,h}}+h\,\|z\|_{2,\Omega_+}\,.$$

For the term $\|I_h(z)-z\|_{1,\Omega_{+,h}}$, we use the interpolation error estimate (3.34) and the H^2 boundedness of the extension operator $\mathcal{E}$. This gives

$$\|I_h(z)-z\|_{1,\Omega_{+,h}} \lesssim h\,\|z\|_{2,\Omega_+}\,.$$

Thus

$$s_h^{1/2}(I_h(z),I_h(z)) \lesssim h\,\|z\|_{2,\Omega_+}\,.$$

Using the stability result (3.42), we conclude

$$s_h^{1/2}(I_h(z),I_h(z)) \lesssim h\,\|u-u_h\|_{0,\Omega_+}\,. \tag{3.48}$$

By substituting the intermediate results from (3.47) and (3.48) into (3.46), we obtain

$$s_h(u_h,I_h(z)) \lesssim (\|u-u_h\|_* + h\,\|u\|_{2,\Omega_+})h\,\|u-u_h\|_{0,\Omega_+}\,. \tag{3.49}$$

Combining the results from (3.44), (3.45), and (3.49), we arrive at

$$\begin{aligned}\|u-u_h\|_{0,\Omega_+}^2 \lesssim& h\,\|u-u_h\|_*\,\|u-u_h\|_{0,\Omega_+} + (\|u-u_h\|_* + h\,\|u\|_{2,\Omega_+})h\,\|u-u_h\|_{0,\Omega_+}\\ \lesssim& (\|u-u_h\|_* + h\,\|u\|_{2,\Omega_+})h\,\|u-u_h\|_{0,\Omega_+}\,.\end{aligned}$$

Finally, using (3.31), we have

$$\|u-u_h\|_{0,\Omega_+}^2 \lesssim h^2\,\|u\|_{2,\Omega_+}\,\|u-u_h\|_{0,\Omega_+}\,,$$

which proves (3.32). □

Remark 3.5 (Some algebraic properties)**.** *In what follows we use the notation introduced in Remark 3.3 and a standard nodal basis. Let A denote the matrix corresponding to the non-stabilized bilinear form $a(\cdot,\cdot)$. The matrix representation of the finite element formulation* (3.8) *is given by*

$$A + L - B^T\widetilde{M}^{-1}B.$$

Since $B^T\widetilde{M}^{-1}B$ is positive semi-definite, $A + L - B^T\widetilde{M}^{-1}B \leq A + L$ in the spectral sense. The coercivity of the bilinear form $a(\cdot,\cdot)$, along with the definition of the norm $\|\cdot\|_*$, implies that there exists a constant $c > 0$, independent of the mesh size h and boundary position within the mesh, such that

$$c(A + L) \leq A + L - B^T\widetilde{M}^{-1}B \leq A + L.$$

This spectral equivalence guarantees that all eigenvalues of $A + L - B^T\widetilde{M}^{-1}B$ are bounded above and below by a scaled version of those in $A + L$.

On a quasi-uniform mesh, this spectral equivalence implies that the condition number of the matrix associated with the finite element formulation (3.8) *scales like $O(h^{-2})$, which is consistent with typical second-order elliptic problems discretized using finite elements.*

Furthermore, the matrix $A + L$ exhibits a standard sparsity structure, which can be efficiently utilized to develop suitable preconditioners for solving the algebraic system.

3.4 Diffuse-interface approximation

Numerical integration over embedded surfaces in finite element discretizations can often be challenging. For instance, it may be necessary to compute coordinates and weights for quatrature points for each segment of the discretized surface. Doing so increases the complexity of the numerical implementation. To avoid these difficulties and reduce computational cost, we adopt the methodology for diffuse-interface approximations in [KB22] and follow the detailed explanation therein. Throughout this section, we assume that Ω_+ is a smooth domain fully embedded within Ω.

The position of the boundary $\Gamma \subset \Omega$ is assumed to be described by a continuous level set function $\varphi \in C(\overline{\Omega})$. The level set function is positive within Ω_+ and negative outside of it, i.e., in $\Omega\backslash\Omega_+$. Hence, $\Gamma = \{\mathbf{x} \in \Omega : \varphi(\mathbf{x}) = 0\}$. In an $O(1)$ neighborhood of Γ, we assume that the level set function is smooth and that its gradient satisfies $|\nabla\varphi| \geq c > 0$. Then, the vector field $\mathbf{n} = -\frac{\nabla\varphi}{|\nabla\varphi|}$ defines an extended unit normal pointing into the exterior of the domain Ω_+.

We approximate the integrals over the boundary Γ by volumetric integrals using a smoothed Dirac delta function δ_ε. This technique is discussed in greater detail in prior works such as [ETT05; ZT10; KB22]. For the smoothing process, we introduce a small parameter $\varepsilon > 0$ that determines the accuracy of the approximation to the Dirac delta distribution $\delta(\varphi) = \lim_{\varepsilon \searrow 0} \delta_\varepsilon(\varphi)$. Various definitions of smoothed delta functions are given in [ZT10].

Given a function $q \in C(\Omega)$, we approximate the surface integral $\int_\Gamma q(\mathbf{x})\mathrm{d}s$ by a volumetric integral of the form $\int_\Omega q(\mathbf{x})\delta_\varepsilon(\varphi(\mathbf{x}))\mathrm{d}\mathbf{x}$. To compute these approximations, we must extend quantities defined on the interface Γ into both the interior of Ω_+ and the exterior region $\Omega \backslash \Omega_+$. To remain consistent with the weak formulation, we employ constant extrapolation in the normal direction. Specifically, the extrapolation of a quantity q at a quadrature point $\mathbf{x}_Q \in \mathcal{O}(\Gamma)$ is performed via a closest-point search and evaluation of q at that closest point.

To motivate the closest-point search algorithm used in this approach, suppose that the level set function φ is an exact signed distance function (SDF). In this case, let $\mathbf{n}_Q = -\nabla\varphi(\mathbf{x}_Q)$ denote the extended outward-pointing unit normal vector at $\mathbf{x}_Q$. Then, for a point $\mathbf{x}_Q \in \Omega$, the closest point $\mathbf{x}_\Gamma$ on the interface Γ is determined by

$$\mathbf{x}_\Gamma = \mathbf{x}_Q + \varphi(\mathbf{x}_Q)\mathbf{n}_Q,$$

since $\varphi(\mathbf{x}_\Gamma) = 0$.

Recall that $\mathcal{T}_h$ denotes the triangulation of Ω and V_h denotes the finite element space corresponding to $\mathcal{T}_h$. Now, let $\varphi_h \in V_h$ be an approximate SDF. In this case, the extended outward-pointing normal vector to Ω_+ at a point $\mathbf{x}_Q$ can be approximated by $\mathbf{n}_Q = -\nabla\varphi_h(\mathbf{x}_Q)$. An approximate closest point on the interface, denoted by $\mathbf{x}_\Gamma^*$, can then be determined using a line search along

$$\hat{\mathbf{x}}(\xi) = \mathbf{x}_Q + \xi\,\mathrm{sign}(\varphi_h(\mathbf{x}_Q))\mathbf{n}_Q, \quad \xi \in \mathbb{R}.$$

Note that $\hat{\mathbf{x}}(0) = \mathbf{x}_Q$. For $\xi_\Gamma^* = |\varphi_h(\mathbf{x}_Q)|$, we have $\hat{\mathbf{x}}(\xi_\Gamma^*) = \mathbf{x}_\Gamma^*$. Since, for an exact SDF φ, the closest point is $\mathbf{x}_\Gamma = \mathbf{x}_\Gamma^*$, this provides a good approximation to the true closest point $\mathbf{x}_\Gamma$.

To evaluate the quantity q at $\mathbf{x}_\Gamma^*$, we need to determine $\mathbf{x}_\Gamma^*$ and the mesh element K_Γ such that $\mathbf{x}_\Gamma^* \in K_\Gamma$. For this purpose, we employ the following algorithm to efficiently locate $\mathbf{x}_\Gamma^*$ on a given mesh (see [KB22]):

- Let $\hat{\varphi}_h(\xi) = \varphi_h(\hat{\mathbf{x}}(\xi))$.
- Set $\xi_0 = 0$.

- For $i = 1, 2, ...$, let $\hat{\mathbf{x}}(\xi_i)$ with $\xi_i > \xi_{i-1}$ be the next intersection of $\hat{\mathbf{x}}(\xi)$ with the boundary ∂K of a mesh cell $K \in \mathcal{T}_h$. Exit the loop when $\hat{\varphi}_h(\xi_{i-1})\hat{\varphi}_h(\xi_i)$ becomes negative for $i = m_Q$.
- Solve a linear equation to find the root $\xi_\Gamma \in [\xi_{m_Q-1}, \xi_{m_Q}]$ of $\hat{\varphi}_h$.
- Set $\mathbf{x}_\Gamma = \hat{\mathbf{x}}(\xi_\Gamma)$.

In addition to determining the approximate closest point $\mathbf{x}_\Gamma^*$, the algorithm identifies the mesh cell K_Γ. The construction of the sequence $\{\hat{\mathbf{x}}(\xi_i)\}_{i=0}^{m_Q}$ for a given point $\mathbf{x}_Q = \hat{\mathbf{x}}(0)$ on a triangular mesh is illustrated in Fig. 3.1. Starting at $\hat{\mathbf{x}}(\xi_{i-1})$, which lies within a mesh cell $K \in \mathcal{T}_h$, we can efficiently locate the next intersection point $\hat{\mathbf{x}}(\xi_i)$ and its adjacent mesh cell $K' \in \mathcal{T}_h$ in the direction of the interface navigation vector $\mathbf{p}_Q = \text{sign}(\varphi_h(\mathbf{x}_Q))\mathbf{n}_Q$. By definition, the points $\hat{\mathbf{x}}(\xi_{m_Q-1})$ and $\hat{\mathbf{x}}(\xi_{m_Q})$ lie within the same mesh cell. The construction of the monotone sequence $\{\hat{\mathbf{x}}(\xi_i)\}_{i=0}^{m_Q}$ can be performed efficiently, particularly when the quadrature point $\mathbf{x}_Q$ lies in a narrow band around Γ. For affine finite elements, the root ξ_Γ, which corresponds to the closest point on the interface, can be computed efficiently using a closed-form expression, because along the line segment connecting these two points, $\hat{\varphi}_h$ behaves as a linear function. This ensures computational efficiency and accuracy in locating both the closest point and the corresponding mesh cell.

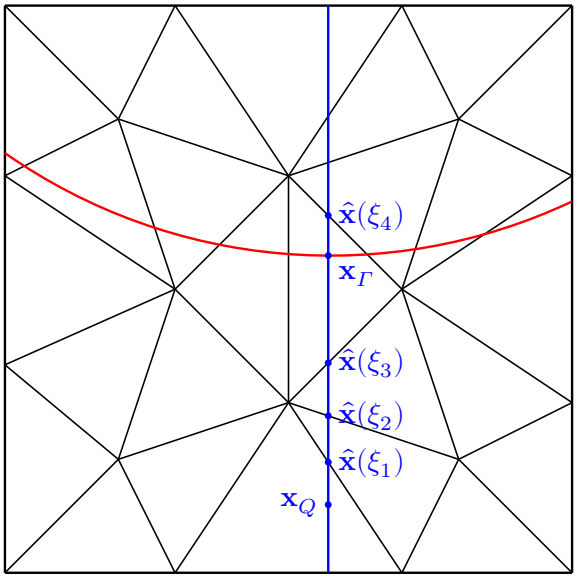

Figure 3.1: Closest point search for a quadrature point $\mathbf{x}_Q$.

Remark 3.6. *In the proposed algorithm, it is not necessary for φ_h to be an approximate SDF. The extended outward-pointing normal vector $\mathbf{n}_Q$ at a quadrature point*

$\mathbf{x}_Q$ can alternatively be constructed using other interface representation techniques, such as a volume-of-fluid function or a phase-field indicator function. This flexibility allows the algorithm to accommodate various methods of describing the interface while maintaining both efficiency and robustness.

Let $\mathcal{E}_{\text{cp}}$ denote the closest-point extension operator, which maps a quantity q at a quadrature point $\mathbf{x}_Q$ to its value at the corresponding approximate closest point $\mathbf{x}_\Gamma^*$ on the interface, i.e., $\mathcal{E}_{\text{cp}} q(\mathbf{x}_Q) = q(\mathbf{x}_\Gamma^*)$. The diffuse-interface formulation, serving as a counterpart to the sharp-interface formulation in (3.8), is expressed as

$$\begin{aligned}
&\int_{\Omega_{+,h}(\delta)} ((1 + H(\varphi_h))\nabla u_h - \mathbf{g}(u)) \cdot \nabla \phi_h \mathrm{d}\mathbf{x} \\
&- \int_\Omega \mathcal{E}_{\text{cp}}(u_h \nabla \phi_h \cdot \mathbf{n}) \delta_\varepsilon(\varphi_h) |\nabla \varphi_h| \mathrm{d}\mathbf{x} - \int_\Omega \mathcal{E}_{\text{cp}}(\phi_h \nabla u_h \cdot \mathbf{n}) \delta_\varepsilon(\varphi_h) |\nabla \varphi_h| \mathrm{d}\mathbf{x} \\
&+ \int_\Omega \alpha \mathcal{E}_{\text{cp}}(u_h \phi_h) \delta_\varepsilon(\varphi_h) |\nabla \varphi_h| \mathrm{d}\mathbf{x} \qquad (3.50) \\
= &\int_{\Omega_{+,h}} f \phi_h \mathrm{d}\mathbf{x} - \int_\Omega \mathcal{E}_{\text{cp}}(g \nabla \phi_h \cdot \mathbf{n}) \delta_\varepsilon(\varphi_h) |\nabla \varphi_h| \mathrm{d}\mathbf{x} \\
&+ \int_\Omega \alpha \mathcal{E}_{\text{cp}}(g \phi_h) \delta_\varepsilon(\varphi_h) |\nabla \varphi_h| \mathrm{d}\mathbf{x}.
\end{aligned}$$

We obtain this formulation by substituting the definitions in (3.3), (3.4), and (3.6) into (3.8) and using the volumetric approximations for surface integrals. Using the Heaviside function $H(\varphi_h)$, which depends on the level set function, we can approximate the integral over Ω_+ as an integral over $\Omega_{+,h}$.

3.5 Numerical results

In this section, we present the results of numerical experiments we conducted to evaluate the performance of the unfitted FEM with PG stabilization for solving the elliptic BVP (3.1) in two spatial dimensions. The study considers various geometries for the subdomain Ω_+ and different choices of the right-hand side f. The L^2 error of an unfitted finite element approximation within the domain Ω is defined as

$$\|u - u_h\|_{0,\Omega_+} = \sqrt{\int_\Omega H(\varphi_h) u_h \mathrm{d}\mathbf{x}},$$

with a Heaviside function $H(\varphi_h)$ based on the level set description.

In the tests involving the diffuse-interface approximation a Gaussian regularization of the Dirac delta function is used. Moreover, following [ZT10], we set

$$\delta_\varepsilon(\varphi) = \frac{1}{\varepsilon}\sqrt{\frac{\pi}{9}}\exp\left(\frac{-\pi^2\varphi^2}{9\varepsilon^2}\right),$$

where $\varepsilon = O(h)$.

All computations were carried out using a custom `C++` implementation based on the open-source finite element library MFEM [DK10b; And+21; And+24]. Visualization was performed with GLVIS [DK10a] and PARAVIEW [AGL05; Aya15].

3.5.1 Quasi-1D test problem

The first experiment considers a quasi-one-dimensional configuration of the BVP (3.1), in which the boundary of Ω_+ is rectangular. The corresponding Test Problem (TP) is defined as follows.

Test Problem 3.1. *Let* $\Omega = (0,1)^2$ *and* $\Gamma = \{0.51\} \times (0,1)$. *For* $f(x,y) = 2$ *and* $u_{ex}(x,y) = (x-0.01)(x-1.01)$ *find* u *such that*

$$\begin{aligned} \Delta u &= f && \text{in } (0,0.51)\times(0,1),\\ u &= u_{ex} && \text{on } \{0,0.51\}\times(0,1),\\ \partial_n u &= 0 && \text{on } (0,0.51)\times\{0,1\}. \end{aligned}$$

We performed grid convergence studies for the sharp- and diffuse-interface formulations of the unfitted Nitsche method with PG stabilization. In particular, we analyzed the sensitivity of numerical results to the extension width parameter δ.

For the sharp-interface method, simulations were carried out with $\delta = 0$ and $\delta = 6h$. In the diffuse-interface variant, we used $\delta = 6h$ and $\delta = \operatorname{diam}\Omega$. Results obtained with these stabilized methods are compared to those of the unstabilized unfitted Nitsche method corresponding to the weak formulation (3.5). The L^2 errors and experimental orders of convergence (EOCs) for uniform grids are summarized in Table 3.1. For reference, the first column of Table 3.4 reports the results of the unstabilized method.

Additionally, we tested the sharp-interface version with $\delta = 0$ and the unstabilized unfitted Nitsche method on successively refined quasi-uniform grids. The coarsest grid used in this study is illustrated in Fig. 3.2, while the corresponding L^2 error behavior is summarized in Table 3.2. Across all cases, second-order convergence was

observed consistently. Furthermore, numerical results exhibited minimal dependence on the value of δ. Numerical solutions computed on a uniform grid with $h = 1/1024$ are shown in Fig. 3.3. No spurious oscillations are observed near the embedded boundary.

Table 3.1: TP 3.1, L^2 convergence history of stabilized methods on uniform meshes.

h^{-1}	sharp $\delta = 0$	EOC	sharp $\delta = 6h$	EOC	diffuse $\delta = 6h$	EOC	diffuse $\delta = d_\Omega$	EOC
128	3.32e-05		3.32e-05		3.12e-05		3.12e-05	
256	8.60e-06	1.95	8.60e-06	1.95	8.15e-06	1.94	8.25e-06	1.92
512	1.96e-06	2.13	1.96e-06	2.13	1.94e-06	2.07	1.94e-06	2.09
1024	5.17e-07	1.92	5.17e-07	1.92	5.14e-07	1.92	5.14e-07	1.92
2048	1.35e-07	1.94	1.35e-07	1.94	1.35e-07	1.93	1.35e-07	1.93
4096	2.87e-08	2.23	2.87e-08	2.23	2.87e-08	2.23	2.89e-08	2.22

Table 3.2: TP 3.1, L^2 convergence on quasi-uniform meshes.

h^{-1}	Nitsche	EOC	sharp, $\delta = 0$	EOC
10	1.38e-03		3.21e-03	
20	3.76e-04	1.88	8.96e-04	1.84
40	1.03e-04	1.87	2.40e-04	1.90
80	2.36e-05	2.13	5.87e-05	2.03
160	6.49e-06	1.86	1.54e-05	1.93
320	1.48e-06	2.13	3.72e-06	2.05
640	4.07e-07	1.86	9.67e-07	1.94

3.5.2 Circular domain test problem

The second TP examines the proposed PG stabilization on a circular subdomain.

Test Problem 3.2. *Let* $\Omega = (0,1)^2$ *and* $\varphi(x,y) = 0.25 - \sqrt{(x-0.5)^2 + (y-0.5)^2}$. *Define* $\Omega_+ = \{(x,y) \in \Omega : \varphi(x,y) > 0\}$ *and* $\Gamma = \partial\Omega_+$. *For* $f(x,y) = 0$ *and* $u_{ex}(x,y) = (x-0.5)^2 - (y-0.5)^2$ *find* u *such that*

$$\begin{aligned} \Delta u &= f \quad && \text{in } \Omega_+, \\ u &= u_{ex} && \text{on } \Gamma. \end{aligned}$$

Grid convergence studies were carried out for both sharp and diffuse-interface formulations with the same values of δ as in the previous test. For comparison

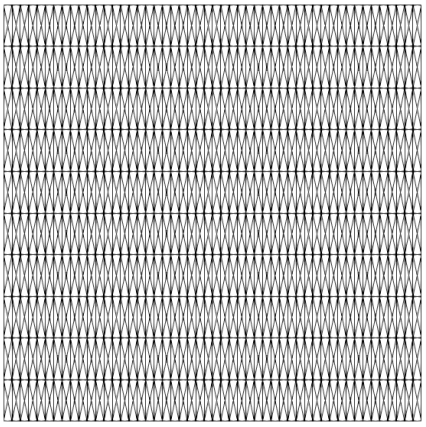

Figure 3.2: Coarse quasi-uniform mesh with $\Delta x = 0.1$ and $\Delta y = 0.02$.

purposes, we also performed simulations using the unstabilized unfitted Nitsche method. The L^2 errors and EOCs for the stabilized methods on uniform grids are presented in Table 3.3, while the results for the unstabilized unfitted Nitsche method are provided in Table 3.4 (second column).

In all cases, we see second-order convergence, with numerical results showing minimal sensitivity to variations in δ. Numerical solutions obtained using a uniform grid with $h = 1/1024$ are illustrated in Fig. 3.4. As expected, there are no oscillations at the boundary of Ω_+, confirming stability and accuracy of the proposed method.

Table 3.3: TP 3.2, L^2 convergence history of stabilized methods on uniform meshes.

h^{-1}	sharp $\delta = 0$	EOC	sharp $\delta = 6h$	EOC	diffuse $\delta = 6h$	EOC	diffuse $\delta = d_\Omega$	EOC
128	6.97e-06		8.92e-06		8.86e-06		1.24e-05	
256	1.82e-06	1.94	2.14e-06	2.06	2.11e-06	2.07	3.27e-06	1.92
512	4.63e-07	1.97	5.08e-07	2.07	4.96e-07	2.09	8.33e-07	1.97
1024	1.16e-07	2.00	1.22e-07	2.06	1.16e-07	2.10	2.06e-07	2.02
2048	2.85e-08	2.03	2.92e-08	2.06	2.63e-08	2.14	4.97e-08	2.05
4096	6.82e-09	2.06	6.92e-09	2.08	5.47e-09	2.27	1.14e-08	2.12

3.5.3 Trapezoidal domain test problem

In the final TP, we solve the elliptic BVP on a trapezoidal domain as proposed in [ACS20].

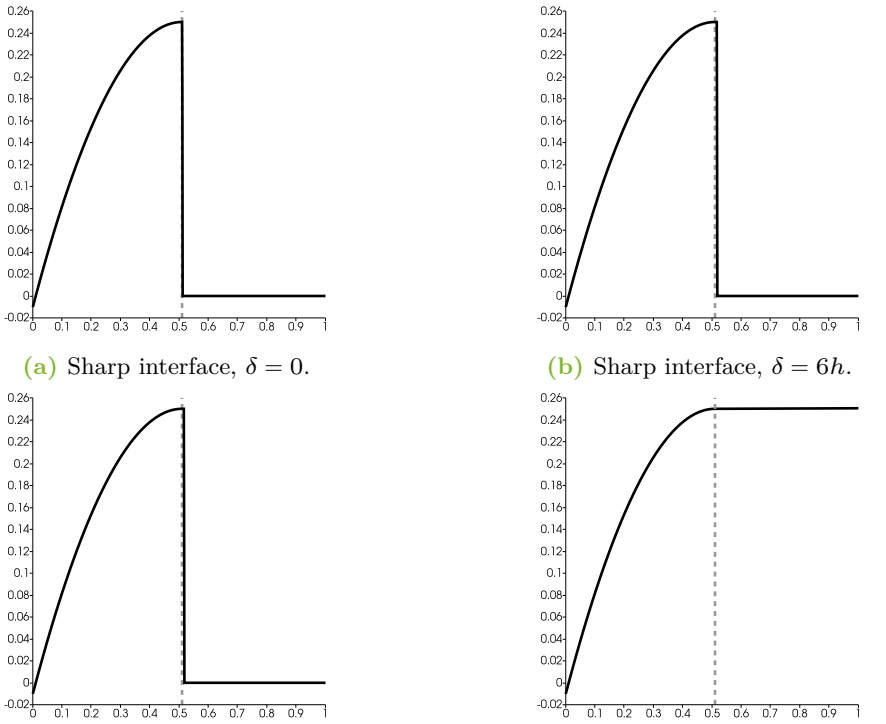

(a) Sharp interface, $\delta = 0$.

(b) Sharp interface, $\delta = 6h$.

(c) Diffuse interface, $\delta = 6h$.

(d) Diffuse interface, $\delta = \operatorname{diam} \Omega$.

Figure 3.3: Numerical solutions to TP 3.1 on a uniform grid with $h = 1/1024$. The boundary is represented by the dshed gray line.

Test Problem 3.3. *Let* $\Omega = (0,1)^2$ *and* $\varphi(x,y) = 1/\sqrt{104}(-10x+2y+4)$. *Let* $\Omega_+ = \{(x,y) \in \Omega : \varphi(x,y) > 0\}$ *and* $\Gamma = \partial\Omega_+$. *For* $f(x,y) = 4\pi^2(\cos(2\pi x) - \sin(2\pi y))$ *and* $u_{ex}(x,y) = y\sin(2\pi x) - x\cos(2\pi y)$ *find* u *such that*

$$\begin{aligned} \Delta u &= f \quad && \text{in } \Omega_+, \\ u &= u_{ex} && \text{on } \Gamma. \end{aligned}$$

In this tTP, the zero level set intersects $\partial\Omega$ arbitrarily. Therefore, we focused exclusively on the sharp-interface version of our unfitted Nitsche method with PG stabilization to study grid convergence. The extension width parameter δ was chosen to be consistent with the values used in the previous example. The L^2 errors and EOCs for the unstabilized unfitted Nitsche method and the stabilized sharp interface method with $\delta = 0$ and $\delta = 6h$ on uniform grids are presented in Table 3.5. Additionally, we tested the unstabilized Nitsche method and the unfitted FEM with PG stabilization ($\delta = 0$) on successively refined quasi-uniform meshes. The coarsest

Table 3.4: TP 3.1–3.2, L^2 convergence history of unstabilized Nitsche method on uniform meshes.

h^{-1}	TP 3.1	EOC	TP 3.2	EOC
128	1.20e-05		2.66e-06	
256	3.27e-06	1.88	6.82e-07	1.96
512	6.10e-07	2.42	1.71e-07	2.00
1024	1.81e-07	1.75	4.25e-08	2.01
2048	5.14e-08	1.82	1.03e-08	2.04
4096	8.01e-09	2.68	2.42e-09	2.09

quasi-uniform mesh is shown in Fig. 3.2. In Table 3.6, we list the L^2 errors and EOCs.

As expected, we see second-order convergence in all configurations. There is minimal sensitivity of numerical results to the extension-width parameter δ. In Fig. 3.5 we show numerical solutions obtained using a uniform grid with $h = 1/512$. Similarly to the previous case, we see no oscillations at the boundary of Ω_+.

Table 3.5: TP 3.3, L^2 convergence history on uniform meshes.

h^{-1}	Nitsche	EOC	$\delta = 0$	EOC	$\delta = 6h$	EOC
16	5.14e-03		9.59e-03		9.60e-03	
32	1.33e-03	1.95	2.71e-03	1.82	2.81e-03	1.77
64	3.32e-04	2.00	6.97e-04	1.96	7.12e-04	1.98
128	8.30e-05	2.00	1.79e-04	1.96	1.78e-04	2.00
256	2.05e-05	2.02	4.39e-05	2.03	4.40e-05	2.02
512	5.15e-06	1.99	1.07e-05	2.04	1.07e-05	2.04

Table 3.6: TP 3.3, L^2 convergence on quasi-uniform meshes.

h^{-1}	Nitsche	EOC	sharp, $\delta = 0$	EOC
10	5.44e-03		8.30e-03	
20	1.39e-03	1.97	2.33e-03	1.83
40	3.57e-04	1.96	6.16e-04	1.92
80	1.04e-04	1.78	1.60e-04	1.94

3.5.4 Conditioning of the system matrix

In addition to assessing convergence rates, we investigated the dependency of the condition number of the system matrix on the placement of the boundary of Ω_+

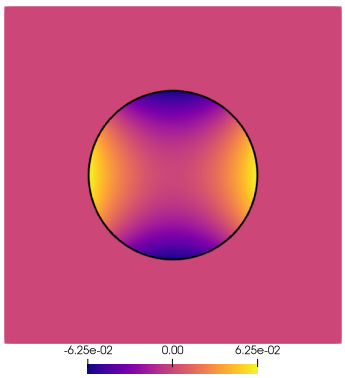

(a) Sharp interface, $\delta = 0$.

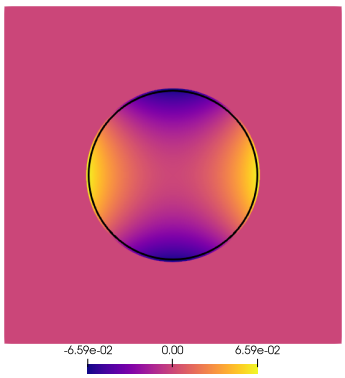

(b) Sharp interface, $\delta = 6h$.

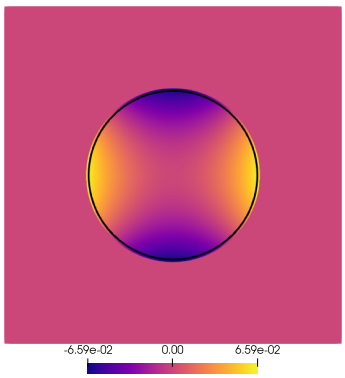

(c) Diffuse interface, $\delta = 6h$.

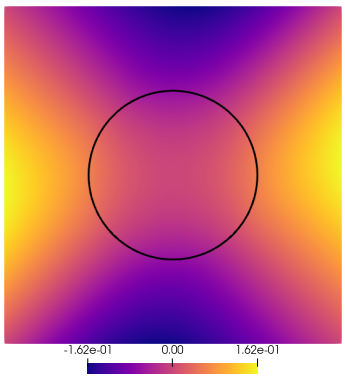

(d) Diffuse-interface, $\delta = \operatorname{diam} \Omega$.

Figure 3.4: Numerical solutions to TP 3.2 on a uniform grid with $h = 1/1024$. The boundary is represented by a black line.

within the mesh. For this study, we applied both the unstabilized unfitted Nitsche method and our proposed sharp interface method with PG stabilization (using $\delta = 0$) to TP 3.1. We kept the mesh fixed and placed the boundary Γ at $x = 0.5 + 10^{-j}$ for $j = 2, 3, \ldots, 8$. By this placement, we decreased the size of the cut cells due to closer alignment between the boundary Γ and mesh edges. The computed condition numbers for both methods are listed in Table 3.7. For the unstabilized unfitted Nitsche method, we see that the condition number increases significantly as cut cells become smaller. In contrast, for our stabilized sharp interface method with $\delta = 0$, the condition number remains uniformly bounded across all configurations. This result demonstrates the algebraic stability of our approach compared to the instability of the unfitted Nitsche method without stabilization.

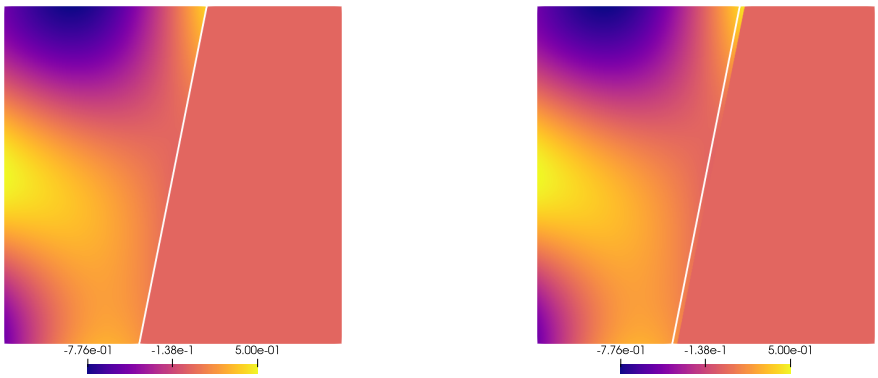

(a) sharp interface, $\delta = 0$ **(b)** sharp interface, $\delta = 6h$

Figure 3.5: Numerical solutions to TP 3.3 on a uniform grid with $h = 1/512$. The boundary is represented by a white line.

Table 3.7: Scaled condition numbers κh^2 of the system matrix for different distances between the mesh cell boundary and boundary.

$\text{dist}(\partial K, \Gamma)$	1e-08	1e-07	1e-06	1e-05	1e-04	1e-03	1e-02
Nitsche	1.43e13	1.43e11	1.43e09	1.42e07	1.36e05	9.47e02	3.22
$\delta = 0$	2.89	2.89	2.89	2.89	2.87	2.75	2.04

3.5.5 Comparison to shifted-boundary method

Finally, we compare the grid convergence behavior of the proposed sharp-interface version of our unfitted Nitsche method with PG stabilization to that of the shifted-boundary method (SBM) (cf. [MS18a; ACS20; ACS21; Sau+21; Yan+24]). For this comparison, the SBM was applied to solve Test Problems 3.2 and 3.3. We ran grid convergence studies for both TPs on uniform meshes and for TP 3.3 on quasi-uniform meshes as in previous tests. The L^2 errors and EOCs on uniform meshes are reported in Table 3.8, while the errors and EOCs for the quasi-uniform meshes are reported in Table 3.9. On average, second-order convergence was observed for all test problems. However, for the test problem involving a circular interface (TP 3.2), an unstable convergence rate was observed for the SBM. In contrast, the unfitted Nitsche method with PG stabilization achieved stable second-order convergence. To mitigate the instability in convergence rates for the SBM, one can include or exclude certain cut elements based on their volume fraction within the interior part of the domain (cf. [Yan+24]). Even though this approach improves stability, additional complexity is introduced. Specifically, excluded cut cells may require extrapolation of solution values up to the true boundary to maintain accuracy. This extrapolation step can pose challenges in implementation and may impact

computational efficiency.

Table 3.8: TP 3.2 and 3.3, L^2 convergence history for the SBM on uniform meshes.

h^{-1}	TP 3.2	EOC	TP 3.3	EOC
128	3.20e-04		4.13e-04	
256	5.53e-05	1.78	7.98e-05	2.37
512	1.14e-05	2.28	1.82e-05	2.13
1024	2.15e-06	2.41	4.36e-06	2.06
2048	4.59e-07	1.23	1.07e-06	2.03
4096	1.38e-07	1.73	2.68e-07	2.00

Table 3.9: TP 3.3, L^2 convergence history for the SBM on quasi-uniform meshes.

h^{-1}	TP 3.3	EOC
10	1.53e-02	
20	3.81e-03	2.01
40	9.56e-04	1.99
80	2.39e-04	2.00

3.6 High-order finite elements

Even though the unfitted Nitsche method with PG stabilization presented thus far achieves second-order accuracy, we can extend it to higher-order accuracy with minor adjustments. The accuracy is currently limited by the lumped-mass L^2 projection used in the stabilization, since it remains second-order accurate even for higher-order finite elements. By replacing the lumped-mass L^2 projection operator by a more accurate projection operator, we are able to achieve higher-order accuracy. One suitable alternative is nodal averaging. In this approach, we compute the coefficients $\mathbf{g}_j(u_h)$ of $\mathbf{g}(u_h)$ in (3.6) as averages of one-sided limits of gradients. For an arbitrary node $\mathbf{x}_j$ let $\mathcal{T}_j$ denote the set of all elements $K \in \mathcal{T}_h(\delta)$ that share the node $\mathbf{x}_j$. We define the coefficents as

$$\mathbf{g}_j(u_h) = \frac{1}{\sum_{K\in\mathcal{T}_j}|K|}\sum_{K\in\mathcal{T}_j}|K|\nabla u_h|_K(\mathbf{x}_j). \tag{3.51}$$

In the case of affine elements, the definitions of the coefficients in (3.7) and (3.51) are equivalent. However, for higher-order finite elements, using nodal averaging ensures optimal accuracy, cf. [Don18; KQ20].

Let us now demonstrate that optimal-order accuracy can be achieved with PG stabilization for higher-order finite elements, when the coefficients defined in equation (3.51) are used. Therefore, we investigate the grid convergence of our sharp-interface method with $\delta = 0$ and compare it to the unstabilized unfitted Nitsche method. Since the solutions of our previous test problems are quadratic in x and y, we have to define a new TP. For this purpose, we consider the following TP.

Test Problem 3.4. *Let* $\Omega = (0,1)^2$ *and* $\Gamma = \{0.51\} \times (0,1)$. *For* $f(x,y) = x^2$ *and* $u_{ex}(x,y) = {}^{x^4}/_{12}$ *find* u *such that*

$$\begin{aligned} \Delta u &= f && \text{in } (0,0.51) \times (0,1), \\ u &= u_{ex} && \text{on } \{0,0.51\} \times (0,1), \\ \partial_n u &= 0 && \text{on } (0,0.51) \times \{0,1\}. \end{aligned}$$

The L^2 errors and EOCs for polynomial degrees $p = 1,2,3$ are presented in Table 3.10 for the unstabilized unfitted Nitsche method and in Table 3.11 for the sharp interface version of our unfitted Nitsche method with PG stabilization. We observed convergence rates of approximately $p+1$ in all cases. This demonstrates that optimal accuracy for both methods is attained when higher-order finite elements are employed. Hence, the PG stabilization is effective in achieving high-order convergence rates.

Table 3.10: TP 3.4, L^2 convergence history of the unstabilized Nitsche method on uniform meshes for different polynomial approximations.

h^{-1}	$p=1$	EOC	$p=2$	EOC	$p=3$	EOC
16	4.75e-05		9.38e-07		8.40e-09	
32	1.59e-05	1.58	1.06e-07	3.14	3.91e-10	4.43
64	4.13e-06	1.94	1.20e-08	3.14	2.89e-11	3.75
128	9.62e-07	2.10	1.83e-09	2.71		
256	2.76e-07	1.80				

Table 3.11: TP 3.4, L^2 convergence history of our stabilized sharp interface method with $\delta = 0$ on uniform meshes for different polynomial approximations.

h^{-1}	$p = 1$	EOC	$p = 2$	EOC	$p = 3$	EOC
16	1.06e-04		9.52e-07		1.96e-07	
32	3.33e-05	1.67	1.07e-07	3.15	1.26e-08	3.96
64	8.83e-06	1.92	1.21e-08	3.14	6.37e-10	4.31
128	2.19e-06	2.01	1.83e-09	2.73		
256	5.89e-07	1.89				

4 Projected gradient stabilization in unfitted finite element methods for elliptic interface problems

In this chapter, we turn our attention to elliptic interface problems as introduced in Chapter 2. For accurate resolution of discontinuities across the interface, fitted finite element methods (FEMs), as presented in Chapter 2, require the mesh to be aligned not only with the outer geometry, but also with the internal interface. As discussed in Chapter 3, constructing meshes fitted to the outer geometry can already be challenging. Additionally, aligning the mesh with the internal interface further increases the computational cost. In Chapter 3, we also discussed the need for remeshing when using fitted FEMs to solve elliptic boundary value problems (BVPs) within evolving domains. The same challenge arises for elliptic interface problems with evolving interfaces or domains, which increases the overall complexity and can negatively affect efficiency and stability.

Unfitted FEMs, also known as embedded or cut FEMs, can be used to overcome these difficulties. While in fitted FEMs the mesh is aligned with the geometry, in their unfitted counterparts, a fixed mesh is constructed independently of the domain and/or interface geometry. Hence, the interface may intersect the mesh arbitrarily. Then, suitable numerical techniques are employed to enforce the interface conditions weakly while preserving accuracy. This approach removes the need for mesh alignment or remeshing, making unfitted FEMs useful when solving elliptic interface problems with complex or evolving geometries.

Building upon the foundation laid in Chapter 3, we develop and analyze a stabilized unfitted FEM for elliptic interface problems. Stabilization is essential for ensuring the robustness and stability of the discrete formulation, particularly in the presence of small cut cells that might otherwise cause ill-conditioning. As in the preceding chapter, we restrict our attention to the stationary problem to focus on the key aspects of spatial discretization and stabilization. Time discretization of evolving problems can be performed analogously to classical fitted FEMs, but without the need for remeshing.

Let $\Omega \subset \mathbb{R}^d$, $d \in \{1, 2, 3\}$, be a bounded Lipschitz domain. The domain Ω is subdivided into two disjoint subdomains Ω_1 and Ω_2 by a smooth embedded interface Γ. Denote by $\mathbf{n}$ the unit normal to Γ pointing outward from Ω_1. Recall that for a

function $v : \Omega \to \mathbb{R}$, we denote by v_k its restriction to Ω_k, $k = 1, 2$. As introduced in Section 2.2, we define the jump $[\![v]\!] = v_1 - v_2$ of v across Γ and the weighted average $\{v\} = \kappa_1 v_1 + \kappa_2 v_2$, with nonnegative weights κ_1 and κ_2 depending on $\mathbf{x} \in \Gamma$. For a vector field $\mathbf{v}(\mathbf{x})$, the jump $[\![\mathbf{v}]\!] = (\mathbf{v}_1 - \mathbf{v}_2) \cdot \mathbf{n}$ and the average $\{\mathbf{v}\} = (\kappa_1 \mathbf{v}_1 + \kappa_2 \mathbf{v}_2) \cdot \mathbf{n}$ are defined in the normal direction $\mathbf{n}$.

In this chapter, we consider the elliptic interface problem

$$-\nabla \cdot (\mu \nabla u) = f \quad \text{in } \Omega_k,\ k = 1, 2, \tag{4.1a}$$
$$u = 0 \quad \text{on } \partial\Omega, \tag{4.1b}$$
$$[\![u]\!] = 0 \quad \text{on } \Gamma, \tag{4.1c}$$
$$[\![\mu \nabla u]\!] = 0 \quad \text{on } \Gamma, \tag{4.1d}$$

where

$$\mu = \begin{cases} \mu_1 & \text{in } \Omega_1, \\ \mu_2 & \text{in } \Omega_2, \end{cases}$$

with constant diffusion coefficients $\mu_k > 0$ and a source term $f \in L^2(\Omega)$.

This chapter has already been published in [OBK25] and is structured as follows. We construct an unfitted FEM based on Nitsche's method for solving the elliptic interface problem (4.1) in Section 4.1. A stabilization term addressing potential algebraic instabilities is introduced and analyzed in Sections 4.2 and 4.3, respectively. A diffuse-interface variant is presented in Section 4.4 to handle difficulties associated with the integration over sharp, unresolved interfaces. Section 4.5 reports the results of numerical studies illustrating the performance of the proposed methods. We conclude the chapter with an extension to convection–diffusion problems in Section 4.6, followed by a high-order extension in Section 4.7.

4.1 Unfitted Nitsche method

To develop a numerical method for solving (4.1), let $\mathcal{T}_h$ be a regular, conforming triangulation of the domain Ω. For simplicity, we assume that the triangulation is fitted to Ω, that is,

$$\bigcup_{K \in \mathcal{T}_h} K = \overline{\Omega}.$$

In general cases, we can use the fictitious domain approach as in Section 3.1 to avoid fitting the triangulation to the domain. Then, in addition to the steps below, we have to follow the steps outlined in Section 3.1 to construct the numerical scheme.

For any $\delta \geq 0$, we define the subtriangulations

$$\mathcal{T}_{h,k}(\delta) = \{K \in \mathcal{T}_h \,:\, \exists\, \mathbf{x} \in K \text{ such that } \operatorname{dist}(\mathbf{x}, \Omega_k) \leq \delta\}, \quad k = 1, 2,$$

consisting of all simplices intersecting a δ-neighborhood of the respective subdomain Ω_k. The corresponding mesh-dependent domains are denoted by $\Omega_{h,k}(\delta)$ and can be defined as

$$\Omega_{h,k}(\delta) = \operatorname{int}\Big(\bigcup_{K \in \mathcal{T}_{h,k}(\delta)} K \Big), \quad k = 1, 2.$$

By construction, $\Omega_k \subset \Omega_{h,k}(\delta)$ for all $\delta \geq 0$. In particular, when $\delta = 0$, the closure of $\Omega_{h,k}(0)$ is the union of all simplices that have a nonempty intersection with the subdomain Ω_k.

Let $V_{h,k}(\delta)$ denote the finite element spaces of continuous, piecewise affine functions defined on the triangulations $\mathcal{T}_{h,k}(\delta)$, i.e.,

$$V_{h,k}(\delta) = \{v_h \in C(\Omega_{h,k}(\delta)) \,:\, v_h|_K \in P_1(K)\ \forall\, K \in \mathcal{T}_{h,k}(\delta),\ v_h = 0 \text{ on } \partial\Omega \cap \partial\Omega_{h,k}\}.$$

Following [HH02], we formulate the standard Nitsche FEM for the elliptic interface problem (4.1) as follows: Find $u_{h,k} \in V_{h,k}(0)$, $k = 1, 2$, such that

$$\begin{aligned} \int_{\Omega_1} \mu_1 \nabla u_{h,1} \cdot \nabla \phi_{h,1} \mathrm{d}\mathbf{x} + \int_{\Omega_2} \mu_2 \nabla u_{h,2} \cdot \nabla \phi_{h,2} \mathrm{d}\mathbf{x} - \int_\Gamma [\![u_h]\!] \{\mu \nabla \phi_h\} \mathrm{d}s \\ - \int_\Gamma \{\mu \nabla u_h\} [\![\phi_h]\!] \mathrm{d}s + \int_\Gamma \alpha [\![u_h]\!] [\![\phi_h]\!] \mathrm{d}s \\ = \int_{\Omega_1} f_1 \phi_{h,1} \mathrm{d}\mathbf{x} + \int_{\Omega_2} f_2 \phi_{h,2} \mathrm{d}\mathbf{x} \quad \forall\, \phi_{h,k} \in V_{h,k}(0),\ k = 1, 2. \end{aligned} \tag{4.2}$$

The averages are defined using element-wise constant weights κ_1, κ_2 representing the volume fractions

$$\kappa_k|_K = \frac{|K \cap \Omega_k|}{|K|}, \qquad k = 1, 2 \tag{4.3}$$

of cut elements $K \in \mathcal{T}_h$. The interior penalty parameter α depends on the local mesh size $h_K = \operatorname{diam}(K)$ and is given by $\alpha|_K = \alpha_0 h_K^{-1}$, where $\alpha_0 = O(1)$ is a sufficiently large constant.

For convenience, we introduce for $u, \phi \in H^1(\Omega_1) \times H^1(\Omega_2)$ the bilinear form

$$\begin{aligned} a(u, \phi) = \int_{\Omega_1} \mu_1 \nabla u_1 \cdot \nabla \phi_1 \mathrm{d}\mathbf{x} + \int_{\Omega_2} \mu_2 \nabla u_2 \cdot \nabla \phi_2 \mathrm{d}\mathbf{x} \\ - \int_\Gamma [\![u]\!] \{\mu \nabla \phi\} \mathrm{d}s - \int_\Gamma \{\mu \nabla u\} [\![\phi]\!] \mathrm{d}s + \int_\Gamma \alpha [\![u]\!] [\![\phi]\!] \mathrm{d}s, \end{aligned} \tag{4.4}$$

and the linear form

$$b(\phi) = \int_{\Omega_1} f_1\phi_1 \mathrm{d}\mathbf{x} + \int_{\Omega_2} f_2\phi_2 \mathrm{d}\mathbf{x} \tag{4.5}$$

to write (4.2) as the abstract problem

$$a(u_h, \phi_h) = b(\phi_h) \quad \forall\, \phi_h \in V_{h,1}(0) \times V_{h,2}(0). \tag{4.6}$$

Recalling the definitions of jumps and averages, the interface terms can be written as

$$\begin{aligned}\llbracket u_h \rrbracket \{\mu \nabla \phi_h\} + \{\mu \nabla u_h\} \llbracket \phi_h \rrbracket - \alpha \llbracket u_h \rrbracket \llbracket \phi_h \rrbracket \\ = q_1(u_{h,1}, u_{h,2}, \phi_{h,1}) - q_2(u_{h,1}, u_{h,2}, \phi_{h,2}),\end{aligned}$$

where

$$\begin{aligned} q_1(u_1, u_2, \phi_1) =& (u_1 - u_2)(\kappa_1\mu_1\nabla\phi_1)\cdot\mathbf{n} + (\kappa_1\mu_1\nabla u_1 + \kappa_2\mu_2\nabla u_2)\phi_1 \cdot \mathbf{n} \\ & - \alpha(u_1 - u_2)\phi_1, \end{aligned} \tag{4.7a}$$

$$\begin{aligned} q_2(u_1, u_2, \phi_2) =& (u_2 - u_1)(\kappa_2\mu_2\nabla\phi_2)\cdot\mathbf{n} + (\kappa_1\mu_1\nabla u_1 + \kappa_2\mu_2\nabla u_2)\phi_2 \cdot \mathbf{n} \\ & + \alpha(u_2 - u_1)\phi_2. \end{aligned} \tag{4.7b}$$

Using this notation, we can express the finite element formulation (4.6) as a system of two coupled problems: For $k = 1, 2$, find $u_{h,k} \in V_{h,k}(0)$ such that

$$\begin{aligned} \int_{\Omega_1} \mu_1 \nabla u_{h,1} \cdot \nabla \phi_{h,1} \mathrm{d}\mathbf{x} - \int_\Gamma q_1(u_{h,1}, u_{h,2}, \phi_{h,1}) \mathrm{d}s \\ = \int_{\Omega_1} f_1 \phi_{h,1} \mathrm{d}\mathbf{x} \quad \forall\, \phi_{h,1} \in V_{h,1}(0), \end{aligned} \tag{4.8a}$$

$$\begin{aligned} \int_{\Omega_2} \mu_2 \nabla u_{h,2} \cdot \nabla \phi_{h,2} \mathrm{d}\mathbf{x} + \int_\Gamma q_2(u_{h,1}, u_{h,2}, \phi_{h,2}) \mathrm{d}s \\ = \int_{\Omega_2} f_2 \phi_{h,2} \mathrm{d}\mathbf{x} \quad \forall\, \phi_{h,2} \in V_{h,2}(0). \end{aligned} \tag{4.8b}$$

In the following sections, we consider stabilized versions of (4.6). To formulate these versions as a system of two coupled problems, we can follow the same steps as previously to express (4.6) as (4.8).

4.2 Projected gradient stabilization

As discussed in Section 3.2, the finite element formulation (4.6) is well posed but prone to numerical instabilities arising from the presence of small cut cells. Over the past years, various stabilization techniques have been proposed to mitigate these effects; see, e.g., [Bur10; LO19].

As an alternative to traditional ghost penalty (GP) stabilization, we employ the projected gradient (PG) stabilization technique introduced for BVPs in Section 3.2. Using this approach, we can stabilize against small cut cells while simultaneously extending the solutions $u_{h,k}$ into $\Omega_{h,k}(\delta)$ for $\delta > 0$. The PG stabilization term for elliptic interface problems is defined by

$$\begin{aligned} s_h(u,\phi) = &\int_{\Omega_{h,1}(\delta)} \mu_1(\nabla u_1 - \mathbf{g}_1(u_1)) \cdot \nabla \phi_1 \mathrm{d}\mathbf{x} \\ &+ \int_{\Omega_{h,2}(\delta)} \mu_2(\nabla u_2 - \mathbf{g}_2(u_2)) \cdot \nabla \phi_2 \mathrm{d}\mathbf{x}, \end{aligned} \tag{4.9}$$

with $u, \phi \in H^1(\Omega_{h,1}(\delta)) \times H^1(\Omega_{h,2}(\delta))$.

Here, $\mathbf{g}_k(u_k)$ denotes the lumped-mass L^2 projection of the generally discontinuous gradient $\nabla u_k \in (L^2(\Omega_{h,k}(\delta)))^d$ into the finite element space $(V_{h,k}(\delta))^d$ for $k = 1, 2$. We compute the projections $\mathbf{g}_k(u_k)$ locally using the nodal basis functions $\{\Psi_j\}_{j=1,\dots,N_{h,k}}$ of $V_{h,k}(\delta)$, where $N_{h,k} = \dim(V_{h,k}(\delta))$. Then

$$\mathbf{g}_k(u_k) = \sum_{j=1}^{N_{h,k}} \mathbf{g}_{j,k}(u_k)\Psi_j, \qquad k = 1, 2,$$

and the coefficients $\mathbf{g}_{j,k}(u_k)$ are explicitly calculated as

$$\mathbf{g}_{j,k}(u_k) = \frac{\int_{\Omega_{h,k}(\delta)} \Psi_j \nabla u_k \mathrm{d}\mathbf{x}}{\int_{\Omega_{h,k}(\delta)} \Psi_j \mathrm{d}\mathbf{x}}, \qquad k = 1, 2, \tag{4.10}$$

where the integration involves only simplices sharing the node $\mathbf{x}_j$ with $\Psi_j(\mathbf{x}_j) = 1$.

By incorporating the PG stabilization term (4.9) into the finite element formulation (4.6), we obtain the stabilized formulation: Find $u_{h,k} \in V_{h,k}(\delta)$, $k = 1, 2$, such that

$$a(u_h, \phi_h) + s_h(u_h, \phi_h) = b(\phi_h) \quad \forall\, \phi_h \in V_{h,1}(\delta) \times V_{h,2}(\delta). \tag{4.11}$$

Remark 4.1. *As discussed in Remark 3.2, projection-based stabilizations are widely used in finite element formulations for convection-dominated transport problems. Therefore, it is natural to employ the same stabilization when extending the present approach to convection–diffusion equations. In Section 4.6, a numerical example illustrating this extension is provided.*

To stabilize consistently across the entire domain, we apply the stabilization globally in $\Omega_{h,k}$ rather than restricting it to a narrow band around the interface. Another, equally important, motivation is the simplicity and robustness of the implementation. Even though in most unfitted FEMs the GP stabilization is defined locally within a narrow band adjacent to the interface, global formulations have also been reported in the literature; see, e.g., [BCM15; MSW18]. In particular, the recent article [OW25] shows that a global definition of the GP may be necessary to preserve the stability of the numerical scheme in problems involving moving interfaces. This observation further supports our choice of a global stabilization strategy.

Remark 4.2 (Algebraic representation)**.** *Let us now examine the algebraic structure of the stabilization term. To this end, we consider the standard Lagrangian nodal basis associated with the finite element spaces under consideration. Let L denote the matrix corresponding to the bilinear form*

$$(\nabla\cdot,\nabla\cdot)_{L^2(\Omega_{h,1})} + (\nabla\cdot,\nabla\cdot)_{L^2(\Omega_{h,2})}.$$

By construction, L is a block-diagonal matrix composed of two standard finite element Laplacians, each defined on $\Omega_{h,k}$ and subject to mixed boundary conditions.

Let B denote the discrete gradient matrix associated with the bilinear form

$$(\nabla v_h, \mathbf{w}_h)_{L^2(\Omega_{h,1})} + (\nabla v_h, \mathbf{w}_h)_{L^2(\Omega_{h,2})},$$

where $v_h \in V_{h,1} \times V_{h,2}$ and $\mathbf{w}_h \in V_{h,1}^d \times V_{h,2}^d$. Furthermore, let $\widetilde{M}$ represent the lumped mass matrix corresponding to the finite element space $V_{h,1}^d \times V_{h,2}^d$.

Written in this notation, the matrix representation of the stabilization form $s_h(\cdot,\cdot)$ is given by

$$L - B^T\widetilde{M}^{-1}B.$$

Thus, at the algebraic level, the stabilization can be interpreted as the difference between the standard finite element Laplacian L and the mixed finite element discretization $B^T\widetilde{M}^{-1}B$ of the Laplacian operator. This interpretation highlights the close relationship between the projection-based stabilization and the underlying differential operator.

Remark 4.3. *For $\delta = \operatorname{diam}(\overline{\Omega})$, which is a valid choice, the extended subdomains $\Omega_{h,k}(\delta)$, $k = 1, 2$, coincide with Ω. In that case, the spaces $V_{h,k}(\delta)$, $k = 1, 2$, coincide with the finite element space for the entire domain. This version of the method is particularly easy to implement in an existing finite element code because it reduces to solving two coupled subproblems on the same mesh.*

4.3 Analysis of the projected gradient stabilization

In this section, we analyze the stabilized FEM (4.11) and establish several fundamental properties of the PG stabilization. For the purposes of this analysis, we assume that the mesh is shape regular and quasi-uniform. Furthermore, for the extension width δ, we impose the condition $\delta \leq Ch$, where $C \geq 0$ is a constant of order $O(1)$. To streamline notation, explicit references to δ are omitted in what follows when describing extended domains and finite element spaces. In subsequent calculations, we understand projections and inner products componentwise whenever the arguments involve vector fields.

Following (4.10), we define the operator $\mathcal{P}_{h,k} : L^2(\Omega_{h,k}) \to V_{h,k}$, which maps functions $v \in L^2(\Omega_{h,k})$ into the finite element space. The operator is expressed as

$$\mathcal{P}_{h,k} v = \sum_{j=1}^{N_{h,k}} \mathrm{g}_{j,k}(v) \Psi_j, \qquad \mathrm{g}_{j,k}(v) = \frac{\int_{\Omega_{h,k}} v \Psi_j \mathrm{d}\mathbf{x}}{\int_{\Omega_{h,k}} \Psi_j \mathrm{d}\mathbf{x}}, \qquad k = 1, 2. \tag{4.12}$$

The bilinear form associated with the PG stabilization term (4.9) employs projections given by $\mathbf{g}_k(u_k) = \mathcal{P}_{h,k} \nabla u_k$ and can be written as

$$\begin{aligned} s_h(u, v) &= \sum_{k=1}^{2} s_{h,k}(u_k, v_k), \\ s_{h,k}(u, v) &= \int_{\Omega_{h,k}} (\nabla u - \mathcal{P}_{h,k} \nabla u) \cdot \nabla v \mathrm{d}\mathbf{x}, \quad u, v \in H^1(\Omega_{h,k}). \end{aligned} \tag{4.13}$$

Remark 4.4. *A very similar stabilization term was used in [BNV22, Eq. (23)]. The difference to* (4.13) *is that the projection operator $\mathcal{P}_{h,k}$ is replaced by an extension operator $\mathcal{P}_k^{ag}$. In addition, the symmetric form*

$$s_{h,k}(u, v) = \int_{\Omega_{h,k}} \gamma (\nabla u - \mathcal{P}_k^{ag} \nabla u) \cdot (\nabla v - \mathcal{P}_k^{ag} \nabla v) \mathrm{d}\mathbf{x}, \quad u, v \in H^1(\Omega_{h,k})$$

of the stabilization term with a penalty parameter γ is employed. As we show in Lemma 4.1 below, our PG stabilization is also symmetric and positive semidefinite.

We start with the proof of the following result.

Lemma 4.1. *The bilinear form $s_{h,k}(u,v)$ is symmetric and satisifies*

$$s_{h,k}(u,u) \simeq \left\|\nabla u - \mathcal{P}_{h,k}\nabla u\right\|^2_{0,\Omega_{h,k}} + h^2 \left\|\nabla \mathcal{P}_{h,k}(\nabla u)\right\|^2_{0,\Omega_{h,k}} \quad \forall\, u \in H^1(\Omega_{h,k}). \tag{4.14}$$

Proof. Follows from Lemma 3.1 for $s_{h,k}(\cdot,\cdot)$. □

The results from Lemma 4.1 imply that $s_{h,k}(\cdot,\cdot)$ induces a semi-inner product.

Corollary 4.2. *The bilinear form $s_{h,k}(\cdot,\cdot)$ induces a semi-inner product on the space $H^1(\Omega_{h,k})$.*

In the second step, we study the stability and approximation properties of the projection operator $\mathcal{P}_{h,k}$, as defined in (4.12).

Lemma 4.3. *The mapping $\mathcal{P}_{h,k}$ is both L^2 and H^1 stable, i.e.,*

$$\left\|\mathcal{P}_{h,k}v\right\|_{0,\Omega_{h,k}} \lesssim \|v\|_{0,\Omega_{h,k}} \quad \text{and} \quad \left\|\nabla\mathcal{P}_{h,k}w\right\|_{0,\Omega_{h,k}} \lesssim \|\nabla w\|_{0,\Omega_{h,k}}$$

for any $v \in L^2(\Omega_{h,k})$, $w \in H^1(\Omega_{h,k})$, $k = 1,2$. Furthermore,

$$\left\|v - \mathcal{P}_{h,k}v\right\|_{0,\Omega_{h,k}} \lesssim h\,\|\nabla v\|_{0,\Omega_{h,k}} \quad \forall\, v \in H^1(\Omega_{h,k}).$$

Proof. Follows from Lemma 3.3 for $\mathcal{P}_{h,k}$. □

We now proceed to estimate $s_{h,k}(u,u)$ from below by a sum of local stabilization terms associated with element patches. Therefore, let $\mathcal{F}_{h,k}$ denote the set of internal facets within the subtriangulation $\mathcal{T}_{h,k}$, and define $\omega(f) = K \cup K'$ as the union of two simplices sharing a facet $f \in \mathcal{F}_{h,k}$. We define $h_f = \max\{h_K, h_{K'}\}$ as the local mesh size corresponding to the patch and introduce the localized stabilization

$$\begin{aligned} s^f_{h,k}(u,v) = &\int_{\omega(f)} [(\nabla u - \mathcal{P}_{h,k}\nabla u)\cdot(\nabla v - \mathcal{P}_{h,k}\nabla v)]\mathrm{d}\mathbf{x} \\ &+ h_f^2 \int_{\omega(f)} (\nabla\mathcal{P}_{h,k}\nabla u) : (\nabla\mathcal{P}_{h,k}\nabla v)\mathrm{d}\mathbf{x}. \end{aligned}$$

Then, (4.14) leads to the estimate

$$s_{h,k}(u,u) \gtrsim \sum_{f\in\mathcal{F}_{h,k}} s^f_{h,k}(u,u) \quad \forall\, u \in H^1(\Omega_{h,k}). \tag{4.15}$$

We are now ready to prove a key technical result.

Lemma 4.4. *For arbitrary $K_1, K_2 \in \mathcal{T}_{h,k}$ such that $K_1 \cup K_2 = \omega(f)$ for a facet $f \in \mathcal{F}_{h,k}$, the following estimates hold:*

$$\|\nabla u\|^2_{0,K_2} \lesssim \|\nabla u\|^2_{0,K_1} + s^f_{h,k}(u,u) \quad \forall\, u \in H^1(\Omega_{h,k}), \tag{4.16}$$

$$\|u_h\|^2_{0,K_2} \lesssim \|u_h\|^2_{0,K_1} + h^2 s^f_{h,k}(u_h,u_h) \quad \forall\, u_h \in V_{h,k}. \tag{4.17}$$

Proof. Follows from Lemma 3.4 for $s^f_{h,k}(\cdot,\cdot)$. □

Recall that the mesh-dependent domains $\Omega_{h,k}$ are composed of simplices fully contained within $\overline{\Omega}_k$, as well as layers of simplices $K \not\subset \overline{\Omega}_k$ that intersect the δ-neighborhood of the interface Γ. Under the assumption that δ is bounded by Ch, the number of layers is finite and independent of the mesh size h. As detailed in Section 3.3, under our assumptions any simplex $K \in \mathcal{T}_h \cap \Omega_{h,k}$ can be reached from a strictly interior simplex by traversing a finite number of facets. Additionally, the number of paths to K, originating from any interior simplex, remains uniformly bounded. This observation, along with estimates (4.16) and (4.15), yields the coercivity result

$$\|\nabla u\|^2_{0,\Omega_{h,k}} \lesssim \|\nabla u\|^2_{0,\Omega_k} + s_{h,k}(u,u) \quad \forall u \in H^1(\Omega_{h,k}). \tag{4.18}$$

This coercivity property plays a crucial role when conducting stability and error analyses for the proposed method. In addition, estimate (4.17) is particularly useful for analyzing problems with evolving interfaces. However, such problems are beyond the scope of this thesis. We now proceed to analyze consistency. While consistency results for both the elliptic terms and Nitsche contributions in the finite element formulation are well established in standard theory (cf. [Žen90; CZ98; HH02]), our focus here is on analyzing the novel stabilization–extension term introduced in [OBK25].

In the following step, we present continuity and consistency results for the PG stabilization term.

Lemma 4.5. *We have*

$$s_{h,k}(u,v) \lesssim \|u\|_{1,\Omega_{h,k}} \|v\|_{1,\Omega_{h,k}} \quad \forall\, u,v \in H^1(\Omega_{h,k}),\ v \in H^1(\Omega_{h,k}), \tag{4.19}$$

$$s_{h,k}(u,u) \lesssim h^2 \|u\|^2_{2,\Omega_{h,k}} \quad \forall\, u \in H^2(\Omega_{h,k}). \tag{4.20}$$

Proof. Follows from Lemma 3.5 for $s_{h,k}(\cdot,\cdot)$. □

To formulate a convergence result, we introduce the norm

$$\|v\|_*^2 = \sum_{k=1}^{2} \left\{ \|v_k\|_{1,\Omega_{h,k}}^2 + h^{-1} \|v_k\|_{0,\Gamma}^2 + s_{h,k}(v_k, v_k) \right\}$$

for $v \in H^1(\Omega_{h,1}) \times H^1(\Omega_{h,2})$.

There exists a bounded linear operator $\mathcal{E} = \mathcal{E}_k : H^1(\Omega_k) \to H^1(\mathbb{R}^d)$ that extends $u_k \in H^1(\Omega_k)$ to a function $\mathcal{E}u_k \in H^1(\Omega)$. As shown in [Ste71], this operator is also a bounded operator from $H^2(\Omega_k)$ to $H^2(\mathbb{R}^d)$. Where no ambiguity arises, we identify u_k with its extension $\mathcal{E}u_k$ defined over the domain Ω and associate $u \in H^1(\Omega_1) \times H^1(\Omega_2)$ with its double extension $\mathcal{E}u = (\mathcal{E}u_1, \mathcal{E}u_2)$.

The theorem below formulates the main convergence result for the proposed approach.

Theorem 4.6. *Assume that $u \in H^2(\Omega_1) \times H^2(\Omega_2)$ solves problem (4.1). We associate with u its double extension $\mathcal{E}u = \{\mathcal{E}u_1, \mathcal{E}u_2\}$. Assume $\delta \lesssim h$ for the extension width δ. Let u_h be a solution to (4.11). Then, for α sufficiently large,*

$$\|u - u_h\|_* \lesssim h \sum_{k=1}^{2} \|u\|_{2,\Omega_k}, \tag{4.21}$$

$$\|u - u_h\|_{0,\Omega_+} \lesssim h^2 \sum_{k=1}^{2} \|u\|_{2,\Omega_k}. \tag{4.22}$$

Proof. Let I_k denote the nodal interpolation operator for $\Omega_{h,k}$ and $I_h(u) \in V_{h,1} \times V_{h,2}$ the componentwise nodal interpolant of u, i.e., $I_h(u) = \{I_1(\mathcal{E}u_1), I_2(\mathcal{E}u_2)\}$. Owing to (4.18), standard arguments (cf. [HH02; BH12; Bur+15]) yield that, for α sufficiently large, the bilinear form

$$A_h(u, v) = a(u, v) + s_h(u, v)$$

is uniformly coercive and that the bilinear form $a(\cdot, \cdot)$ is continuous on the finite element space with respect to the norm $\|\cdot\|_*$. Specifically, $A_h(v_h, v_h) \gtrsim \|v_h\|_*^2$ for all $v_h \in V_h$ and $a(u_h, v_h) \lesssim \|u_h\|_* \|v_h\|_*$ for all $u_h, v_h \in V_h$. Following the arguments leading to (3.33), we therefore have

$$\begin{aligned} \|I_h(u) - u_h\|_*^2 \lesssim & A_h(I_h(u) - u_h, I_h(u) - u_h) \\ = & a(I_h(u) - u, I_h(u) - u_h) + s_h(I_h(u) - u, I_h(u) - u_h) \\ & + s_h(u, I_h(u) - u_h), \end{aligned} \tag{4.23}$$

where we use the fact that u_h solves (4.11) and u is a solution of (4.1). In the next step, we use the continuity of the bilinear form $a(\cdot,\cdot)$, the interpolation error estimate (cf., e.g., [BH12, Lemma 5] combined with Lemma 4.5)

$$\|I_h(u) - u\|_* \lesssim h \sum_{k=1}^{2} \|\mathcal{E}u\|_{2,\Omega_{h,k}}, \tag{4.24}$$

and the H^2 boundedness of the extension operator $\mathcal{E}$, ensuring $\sum_{k=1}^{2} \|\mathcal{E}u\|_{2,\Omega_{h,k}} \lesssim \sum_{k=1}^{2} \|u\|_{2,\Omega_k}$. Using these results, we estimate the first term on the right-hand side of (4.23) as

$$a(I_h(u) - u, I_h(u) - u_h) \lesssim \left(h \sum_{k=1}^{2} \|u\|_{2,\Omega_k} \right) \|I_h(u) - u_h\|_* . \tag{4.25}$$

For the second term in (4.23), we use the continuity property (4.19) of $s_h(\cdot,\cdot)$, the definition of the norm $\|\cdot\|_*$, and similar arguments as for the first term to conclude

$$s_h(I_h(u) - u, I_h(u) - u_h) \lesssim \left(h \sum_{k=1}^{2} \|u\|_{2,\Omega_k} \right) \|I_h(u) - u_h\|_* . \tag{4.26}$$

We use Corollary 4.2 to apply the Cauchy–Schwarz inequality in the third term on the right-hand side of (4.23). Together with the properties (4.19) and (4.20) of $s_h(\cdot,\cdot)$, the definition of the norm $\|\cdot\|_*$, and the H^2 boundedness of the extension operator $\mathcal{E}$, we find

$$s_h(u, I_h(u) - u_h) \lesssim h \sum_{k=1}^{2} \|u\|_{2,\Omega_k} \|I_h(u) - u_h\|_* . \tag{4.27}$$

Collecting (4.23), (4.25), (4.26), and (4.27), we conclude

$$\|I_h(u) - u_h\|_*^2 \lesssim \left(h \sum_{k=1}^{2} \|u\|_{2,\Omega_k} \right) \|I_h(u) - u_h\|_* .$$

This estimate, together with the triangle inequality, the interpolation error estimate (4.24), and the H^2 boundedness of the extension operator, proves (4.21).

To prove (4.22), we now employ a duality argument. Let z be the solution of the following dual problem:

$$\begin{aligned} -\nabla \cdot (\mu \nabla z) &= u - u_h \quad \text{in } \Omega, \\ z &= 0 \quad \text{on } \partial\Omega, \\ [\![z]\!] &= 0 \quad \text{on } \Gamma, \\ [\![\mu \nabla z]\!] &= 0 \quad \text{on } \Gamma. \end{aligned} \tag{4.28}$$

It is well known, see [Kel74], that $z \in H^2(\Omega_1) \times H^2(\Omega_2)$ and

$$\sum_{k=1}^{2} \|z\|_{2,\Omega_k} \lesssim \|u - u_h\|_{0,\Omega}. \tag{4.29}$$

Denote by $I_h(z) \in V_{h,1} \times V_{h,2}$ the componentwise nodal interpolant of (the extension of) z. The interpolation operator I_h possesses standard approximation properties, which will be utilized in subsequent steps of the proof.

To proceed, we multiply the first equation in (4.28) by $u - u_h$ and integrate by parts. Following the derivation of (3.44), this yields

$$\|u - u_h\|_{0,\Omega}^2 = a(u - u_h, z - I_h(z)) + s_h(u_h, I_h(z)), \tag{4.30}$$

since u is the solution of the continuous problem (4.1), and u_h is the solution of the discrete problem (4.11).

For the first term on the right-hand side of (4.30), we use the continuity of $a(\cdot,\cdot)$, the interpolation error estimate for $I_h(z)$, and the H^2 boundedness of the extension operator $\mathcal{E}$. This yields

$$a(u - u_h, z - I_h(z)) \lesssim h \|u - u_h\|_* \|u - u_h\|_{0,\Omega}. \tag{4.31}$$

We use the Cauchy–Schwarz inequality in the second term on the right-hand side of (4.30) to obtain

$$s_h(u_h, I_h(z)) \lesssim s_h^{1/2}(u_h, u_h) s_h^{1/2}(I_h(z), I_h(z)). \tag{4.32}$$

Using the triangle inequality, (4.19), (4.20), and the H^2 boundedness of $\mathcal{E}$, we deduce

$$s_h^{1/2}(u_h, u_h) \lesssim \|u - u_h\|_* + h \sum_{k=1}^{2} \|u\|_{2,\Omega_k}. \tag{4.33}$$

Using the same arguments as before, together with the interpolation error estimate (4.24) and the stability result (4.29), we estimate

$$s_h^{1/2}(I_h(z), I_h(z)) \lesssim h \|u - u_h\|_{0,\Omega}. \tag{4.34}$$

By substituting (4.33) and (4.34) into (4.32), we obtain

$$s_h(u_h, I_h(z)) \lesssim \left(\|u - u_h\|_* + h \sum_{k=1}^{2} \|u\|_{2,\Omega_k} \right) h \|u - u_h\|_{0,\Omega}. \tag{4.35}$$

Combining (4.30), (4.31), and (4.35), we arrive at

$$\begin{aligned}\|u-u_h\|_{0,\Omega}^2 \lesssim & h\,\|u-u_h\|_*\,\|u-u_h\|_{0,\Omega} + \left(\|u-u_h\|_* + h\sum_{k=1}^{2}\|u\|_{2,\Omega_k}\right) h\,\|u-u_h\|_{0,\Omega} \\ \lesssim & (\|u-u_h\|_* + h\sum_{k=1}^{2}\|u\|_{2,\Omega_k})h\,\|u-u_h\|_{0,\Omega}\,.\end{aligned}$$

Using (4.21), we obtain

$$\|u-u_h\|_{0,\Omega}^2 \lesssim \left(h^2\sum_{k=1}^{2}\|u\|_{2,\Omega_k}\right)\|u-u_h\|_{0,\Omega}\,,$$

which proves (4.22). □

Remark 4.5 (Some algebraic properties)**.** *Using the notation introduced in Remark 4.2 and employing a standard nodal basis, let A denote the matrix corresponding to the (non-stabilized) bilinear form $a(\cdot,\cdot)$. The matrix representation of the finite element problem* (4.11) *is*

$$A + L - B^T\widetilde{M}^{-1}B.$$

Since $B^T\widetilde{M}^{-1}B$ is positive semidefinite, it follows that

$$A + L - B^T\widetilde{M}^{-1}B \leq A + L$$

in the spectral sense. Moreover, by the coercivity of $a(\cdot,\cdot)$ and the definition of the norm $\|\cdot\|_*$, there exists a constant $c > 0$, independent of the mesh size h and of the position of the interface within the mesh, such that

$$c(A + L) \leq A + L - B^T\widetilde{M}^{-1}B \leq A + L$$

holds in the spectral sense. Hence, the eigenvalues of $A + L - B^T\widetilde{M}^{-1}B$ are bounded from above and below by scaled versions of the eigenvalues of $A + L$. This result implies that, for a quasi-uniform mesh, the condition number of $A + L - B^T\widetilde{M}^{-1}B$ scales as $O(h^{-2})$. Furthermore, the matrix $A + L$ possesses a standard sparsity pattern, which can be efficiently exploited when constructing suitable preconditioners for the linear systems arising from the finite element discretization.

4.4 Diffuse-interface approximation

The method presented so far uses integration over sharp embedded interfaces. However, in Section 3.4 we discussed difficulties arising from such integrations in the context of unfitted finite element discretizations. To overcome these difficulties, we use the methodology presented in Section 3.4.

Let us assume that the interface $\Gamma \subset \Omega$ is the zero level set of an level set function $\varphi \in C(\overline{\Omega})$, i.e., $\Gamma = \{\mathbf{x} \in \Omega : \varphi(\mathbf{x}) = 0\}$. Within Ω_1, the level set function φ is assumed to be positive, and in Ω_2 it is negative. We further assume that φ is smooth within an $O(1)$ neighborhood of Γ and that its gradient satisfies $|\nabla\varphi| \geq c > 0$ within this region. Under these assumptions, an extended unit normal to Γ, pointing outward from Ω_1, is defined by the vector field $\mathbf{n} = -\frac{\nabla\varphi}{|\nabla\varphi|}$.

To integrate a quantity q over Γ, we use smoothed Dirac delta functions $\delta_\varepsilon(\varphi)$, as introduced in Section 3.4, to approximate the surface integral $\int_\Gamma q(\mathbf{x})\mathrm{d}s$ by the volumetric integral $\int_\Omega q(\mathbf{x})\,\delta_\varepsilon(\varphi(\mathbf{x}))\,|\nabla\varphi(\mathbf{x})|\mathrm{d}\mathbf{x}$. To ensure consistency with the weak form, we use constant extrapolation in normal direction from the interface. Using the closest point extension operator $\mathcal{E}_{\mathrm{cp}}$ defined in Section 3.4 to extend the interface terms (4.7), we also have consistency with the jump conditions (4.1c) and (4.1d). Specifically,

$$\mathcal{E}_{\mathrm{cp}}q_1(u_1, u_2, \phi_1) - \mathcal{E}_{\mathrm{cp}}q_2(u_1, u_2, \phi_2) = 0 \qquad \text{for } \mathbf{x} \in \Omega$$

if

$$[\![u]\!] = [\![\mu\nabla u]\!] = [\![\phi]\!] = 0 \qquad \text{at } \mathbf{x}_\Gamma(\mathbf{x}) \in \Gamma.$$

Consequently, the contribution of the diffuse Nitsche integrals to the weak formulation vanishes when the jump conditions are satisfied.

Let $\varphi_h \in V_h$ denote an approximation to φ in the finite element space. A diffuse-

interface counterpart to the sharp-interface formulation (4.11) is given by

$$\begin{aligned}
&\int_{\Omega_{h,1}(\delta)} \mu_1((1+H(\varphi_h))\nabla u_{h,1} - \mathbf{g}_1(u_h)) \cdot \nabla \phi_{h,1} \mathrm{d}\mathbf{x} \\
&- \int_{\Omega} \mathcal{E}_{\mathrm{cp}}(u_{h,1}, u_{h,2}, \phi_{h,1}) \delta_\varepsilon(\varphi_h) |\nabla \varphi_h| \mathrm{d}\mathbf{x} \\
&+ \int_{\Omega_{h,2}(\delta)} \mu_1((2-H(\varphi_h))\nabla u_{h,2} - \mathbf{g}_2(u,h)) \cdot \nabla \phi_{h,2} \mathrm{d}\mathbf{x} \\
&+ \int_{\Omega} \mathcal{E}_{\mathrm{cp}}(u_{h,1}, u_{h,2}, \phi_{h,2}) \delta_\varepsilon(\varphi_h) |\nabla \varphi_h| \mathrm{d}\mathbf{x} \\
= &\int_{\Omega_1} f_1 \phi_{h,1} \mathrm{d}\mathbf{x} + \int_{\Omega_2} f_2 \phi_{h,2} \mathrm{d}\mathbf{x} \quad \forall \{\phi_{h,1},\, \phi_{h,2}\} \in V_{h,1}(\delta) \times V_{h,2}(\delta).
\end{aligned} \tag{4.36}$$

This formulation is obtained by substituting the definitions in (4.4), (4.5), and (4.9) into (4.11) and approximating the surface integrals by volumetric integrals. Using the Heaviside function $H(\varphi_h)$, depending on the level set function, we can express the integral over Ω_k as an integral over $\Omega_{h,k}$.

4.5 Numerical results

This section presents results of numerical experiments for the unfitted FEM with PG stabilization applied to the elliptic interface problem (4.1) in two spatial dimensions. We consider several configurations of the diffusion coefficient μ, the right-hand side f, boundary conditions, and interface geometries. The L^2 error for an unfitted finite element approximation on Ω is defined by

$$\|u_h - u\|_{0,\Omega} = \sqrt{\int_{\Omega} \left(H(\varphi) u_{h,1} + (1 - H(\varphi_h)) u_{h,2} - u\right)^2 \mathrm{d}\mathbf{x}},$$

with a Heaviside function $H(\varphi)$ based on the level set description.

Following [ZT10], we use an Gaussian approximation of the Dirac delta function in the tests involving the diffuse-interface approximation. Hence,

$$\delta_\varepsilon(\varphi) = \frac{1}{\varepsilon}\sqrt{\frac{\pi}{9}} \exp\left(\frac{-\pi^2 \varphi^2}{9\varepsilon^2}\right),$$

where $\varepsilon = O(h)$.

All computations were performed using a custom `C++` implementation based on the open-source finite element library MFEM [DK10b; And+21; And+24]. Visualization was carried out with GLVIS [DK10a] and PARAVIEW [AGL05; Aya15].

4.5.1 Straight interface and smooth solution

In the first numerical test, we apply the proposed methods to a Test Problem (TP) featuring a smooth exact solution and a straight interface. The TP is defined as follows.

Test Problem 4.1. *Let* $\Omega = (0,1)^2$ *and* $\Gamma = \{(x,y) \in \overline{\Omega} : x = 0.51\}$. *Set* $\mu_1 = 10^{-8}$, $\mu_2 = 1$ *and* $f_1 = 2 \cdot 10^{-8}$, $f_2 = 2$. *For* $u_{ex} = \{u_1, u_2\}$ *with*

$$u_1(x,y) = (x - 0.01)(1.01 - x) = u_2(x,y),$$

find u *such that*

$$\begin{aligned} -\nabla \cdot (\mu \nabla u) &= f && \text{in } \Omega, \\ u &= u_{ex} && \text{on } \{0,1\} \times (0,1), \\ \partial_n u &= 0 && \text{on } (0,1) \times \{0,1\}, \\ [\![u]\!] &= 0 && \text{on } \Gamma, \\ [\![\mu \nabla u]\!] &= 0 && \text{on } \Gamma. \end{aligned}$$

This TP is called quasi-one-dimensional since the exact solution is independent of y. In addition to the convergence rate, we studied the dependence of the L^2 error on the extension-width parameter δ. We ran simulations of the sharp-interface and diffuse-interface variants of the unfitted FEM with PG stabilization on successively refined uniform grids. For the sharp-interface formulation, we used $\delta = 0$ and $\delta = 6h$, while for the diffuse-interface formulation, we used $\delta = 6h$ and $\delta = d_\Omega$, where $d_\Omega = \operatorname{diam}(\overline{\Omega})$. The L^2 errors and experimental orders of convergence are reported in Table 4.1. For comparison, we also ran simulations with the Hansbo & Hansbo (H^2) method (see [HH02]), corresponding to (4.6); we list the results in the first two columns of Table 4.5. In addition, we tested the sharp-interface version with $\delta = 6h$ on a sequence of quasi-uniform meshes. The coarsest of these meshes is shown in Fig. 3.2. The results obtained on quasi-uniform meshes are summarized in Table 4.2. We see almost no dependence on the extension-width parameter δ. The observed experimental order of convergence (EOC) is approximately two in all cases. Numerical solutions obtained on a uniform mesh with $h = 1/1024$ are shown in Fig. 4.1. In all cases, we see a smooth transition without any oscillations between u_1 and u_2 at the interface.

4.5.2 Straight interface and non-smooth solution

The second example features a non-smooth exact solution with a kink across the interface, while using the same domain and interface as the previous TP. Following [HH02], we define the TP as follows.

Table 4.1: TP 4.1, L^2 convergence history of stabilized methods on uniform meshes.

h^{-1}	sharp $\delta = 0$	EOC	sharp $\delta = 6h$	EOC	diffuse $\delta = 6h$	EOC	diffuse $\delta = d_\Omega$	EOC
128	4.02e-05		4.02e-05		4.02e-05		4.02e-05	
256	1.01e-05	1.99	1.01e-05	1.99	1.01e-05	1.99	1.01e-05	1.99
512	2.54e-06	1.99	2.54e-06	1.99	2.54e-06	1.99	2.54e-06	1.99
1024	6.35e-07	2.00	6.35e-07	2.00	6.35e-07	2.00	6.35e-07	2.00
2048	1.59e-07	2.00	1.59e-07	2.00	1.59e-07	2.00	1.59e-07	2.00
4096	3.96e-08	2.01	3.99e-08	1.99	3.98e-08	2.00	3.99e-08	1.99

Test Problem 4.2. *Let* $\Omega = (0,1)^2$ *and* $\Gamma = \{(x,y) \in \overline{\Omega} : x = 0.51\}$. *Set* $\mu_1 = 0.5$, $\mu_2 = 3$ *and* $f_1 = f_2 = 1$. *For* $u_{ex} = \{u_1, u_2\}$ *with*

$$u_1(x,y) = \frac{9}{14}(x - 0.01) - (x - 0.01)^2,$$
$$u_2(x,y) = \frac{5}{84} + \frac{9}{84}(x - 0.01) - \frac{1}{6}(x - 0.01)^2,$$

find u *such that*

$$\begin{aligned} -\nabla \cdot (\mu \nabla u) &= f && \text{in } \Omega, \\ u &= u_{ex} && \text{on } \{0,1\} \times (0,1), \\ \partial_n u &= 0 && \text{on } (0,1) \times \{0,1\}, \\ [\![u]\!] &= 0 && \text{on } \Gamma, \\ [\![\mu \nabla u]\!] &= 0 && \text{on } \Gamma. \end{aligned}$$

The analytical solution $u(x,y)$ equals u_1 for $x \leq 0.51$ and u_2 for $x \geq 0.51$, remains independent of y, and exhibits a kink at $x = 0.51$. Using the same configurations as in the previous example, we ran grid-convergence studies. The L^2 errors and EOCs obtained on uniform grids for our stabilized method are reported in Table 4.3. For comparison, the results for the unstabilized H^2 method are listed in Table 4.5. In addition to the test on uniform meshes, we ran simulations on quasi-uniform meshes. The results obtained on these meshes are listed in Table 4.2. In all cases, we observe second-order L^2 convergence with almost no dependence on the extension-width parameter δ. Figure 4.2 displays numerical solutions obtained with $h = 1/1024$. In all cases, we see good agreement of u_1 and u_2, without any oscillations, at the interface.

Table 4.2: TP 4.1 and 4.2, L^2 convergence of the sharp-interface method with $\delta = 0$ on quasi-uniform meshes.

h^{-1}	TP 4.1	EOC	4.2	EOC
10	4.23e-03		3.09e-03	
20	1.15e-03	1.88	8.36e-04	1.89
40	2.98e-04	1.94	2.16e-04	1.95
80	7.60e-05	1.98	5.50e-05	1.97
160	1.92e-05	1.98	1.39e-05	1.98
320	4.82e-06	1.99	3.48e-06	2.00
640	1.21e-06	1.99	8.72e-07	2.00

Table 4.3: TP 4.2, L^2 convergence history of stabilized methods on uniform meshes.

h^{-1}	sharp $\delta = 0$	EOC	sharp $\delta = 6h$	EOC	diffuse $\delta = 6h$	EOC	diffuse $\delta = d_\Omega$	EOC
128	2.91e-05		2.91e-05		2.67e-05		2.67e-05	
256	7.31e-06	1.99	7.31e-06	1.99	8.29e-06	1.69	8.29e-06	1.69
512	1.83e-06	2.00	1.83e-06	2.00	1.38e-06	2.59	1.38e-06	2.59
1024	4.57e-07	2.00	4.57e-07	2.00	4.16e-07	1.73	4.16e-07	1.73
2048	1.03e-07	2.15	1.03e-07	2.15	9.79e-08	2.09	9.79e-07	2.09
4096	2.29e-08	2.17	2.29e-08	2.17	2.75e-08	1.83	2.75e-08	1.83

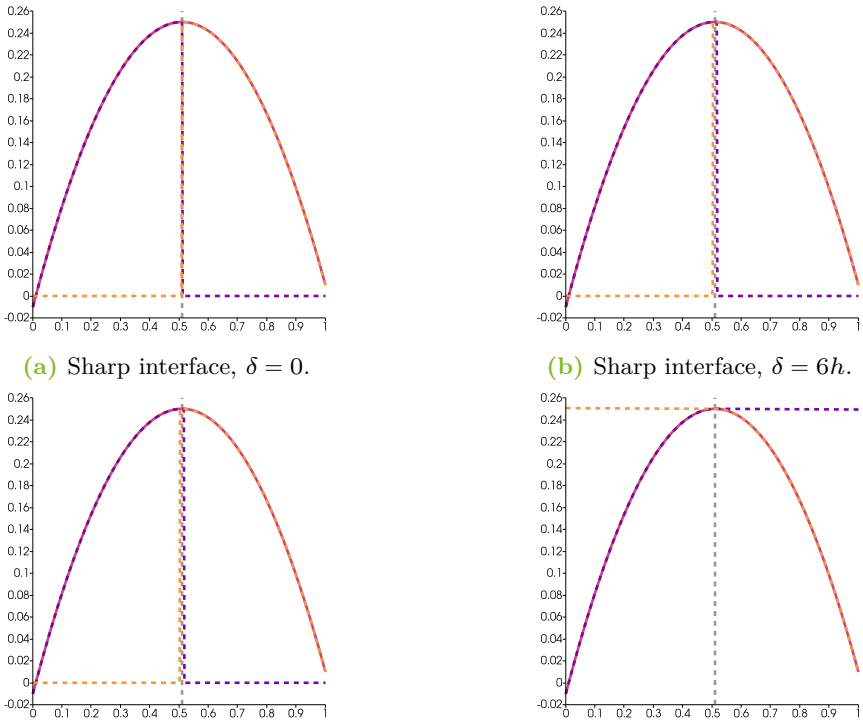

(a) Sharp interface, $\delta = 0$.

(b) Sharp interface, $\delta = 6h$.

(c) Diffuse interface, $\delta = 6h$.

(d) Diffuse interface, $\delta = \operatorname{diam} \Omega$.

Figure 4.1: Numerical solutions (u in pink, extended u_1 in purple, extended u_2 in orange) to TP 4.1 on a uniform grid with $h = 1/1024$. The interface is represented by the dashed grey line.

4.5.3 Circular interface and non-smooth solution

To demonstrate the efficiency for arbitrary interfaces, let us now apply the unfitted FEM with PG stabilization to a fully two-dimensional configuration with a circular interface, cf. [HH02].

Test Problem 4.3. *Let $\Omega = (-1,1)^2$ and let Γ be the zero level set of the signed distance function (SDF) $\varphi(x,y) = 0.75 - \sqrt{x^2+y^2}$. Set $\mu_1 = 1$, $\mu_2 = 10^3$ and $f_1 = f_2 = 4$. For $u_{ex} = \{u_1, u_2\}$ with*

$$u_1(x,y) = x^2 - y^2,$$
$$u_2(x,y) = \frac{x^2 - y^2}{1000} - \frac{0.5625}{1000} + 0.5625,$$

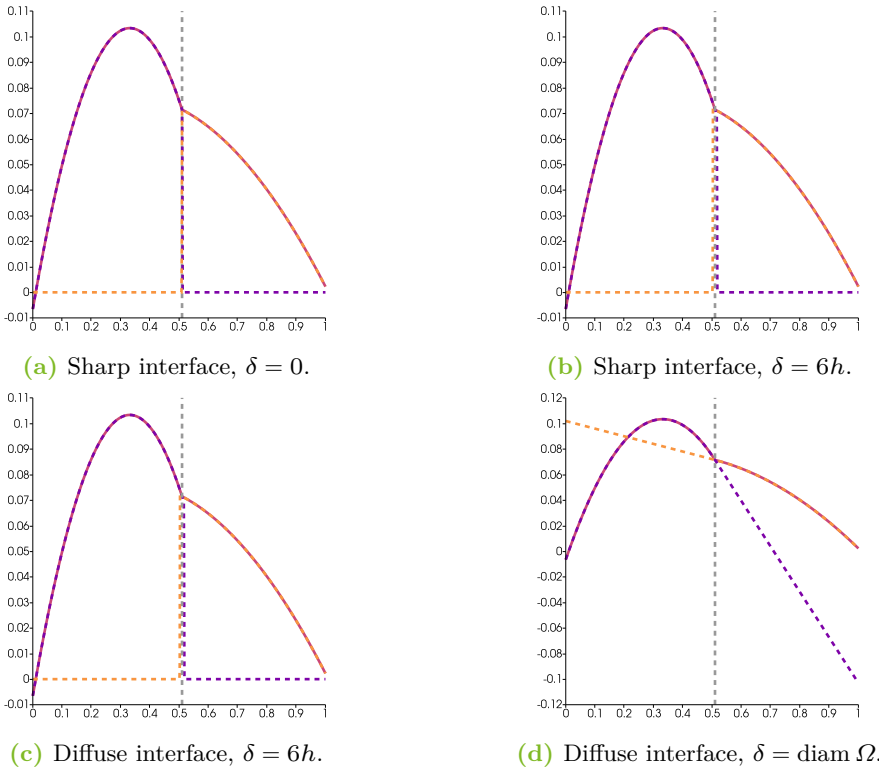

(a) Sharp interface, $\delta = 0$.

(b) Sharp interface, $\delta = 6h$.

(c) Diffuse interface, $\delta = 6h$.

(d) Diffuse interface, $\delta = \operatorname{diam} \Omega$.

Figure 4.2: Numerical solutions (u in pink, extended u_1 in purple, extended u_2 in orange) to TP 4.2 on a uniform grid with $h = 1/1024$. The interface is represented by the dashed grey line.

find u such that

$$\begin{aligned} -\nabla \cdot (\mu \nabla u) &= f && \text{in } \Omega, \\ u &= u_{ex} && \text{on } \partial\Omega, \\ [\![u]\!] &= 0 && \text{on } \Gamma, \\ [\![\mu \nabla u]\!] &= 0 && \text{on } \Gamma. \end{aligned}$$

To study the grid convergence of both the sharp- and diffuse-interface versions of the proposed method with PG stabilization, we ran simulations on successively refined grids using the same parameter settings as above. The L^2 errors and EOC on uniform meshes are reported in Table 4.4. For comparison, the results obtained with the unstabilized H^2 method under identical conditions are listed in the last two columns of Table 4.5. In all cases, we observed second-order L^2 convergence. Numerical solutions obtained with the diffuse-interface formulation using $\delta = 6h$ and $\delta = d_\Omega$ on a uniform mesh with $h = 1/512$ are displayed in Figs. 4.3 and 4.4,

respectively. Both solutions show good agreement of u_1 and u_2 along the circular interface without the occurrence of spurious oscillations.

Table 4.4: TP 4.3, L^2 convergence history of stabilized methods on uniform meshes.

h^{-1}	sharp $\delta = 0$	EOC	sharp $\delta = 6h$	EOC	diffuse $\delta = 6h$	EOC	diffuse $\delta = d_\Omega$	EOC
128	2.74e-04		2.96e-04		2.90e-04		3.30e-04	
256	6.87e-05	2.00	7.16e-05	2.05	6.86e-05	2.08	8.15e-05	2.02
512	1.72e-05	2.00	1.76e-05	2.02	1.61e-05	2.09	1.97e-05	2.05
1024	4.31e-06	2.00	4.35e-06	2.02	3.60e-06	2.16	4.56e-06	2.11

Table 4.5: TP 4.1 – 4.3, L^2 convergence history of the H^2 method on uniform meshes.

h^{-1}	TP 4.1	EOC	TP 4.2	EOC	TP 4.3	EOC
128	1.03e-05		7.47e-06		1.08e-04	
256	2.59e-06	1.99	1.86e-06	2.01	2.69e-05	2.01
512	6.48e-07	2.00	4.64e-07	2.00	6.72e-06	2.00
1024	1.62e-07	2.00	1.15e-07	2.01	1.69e-06	1.99
2048	4.05e-08	2.00	1.93e-08	2.57		
4096	9.55e-09	2.08	4.64e-09	2.06		

4.5.4 Conditioning of the system matrix

In addition to accuracy, we analyzed the sensitivity of the condition number of the system matrix to the interface placement within the mesh. We applied the unstabilized H^2 method and the sharp-interface version of our unfitted FEM with PG stabilization using $\delta = 0$ to TP 4.1. To assess the sensitivity, we modified the placement of the interface, placing it at $x = 0.5 + 10^{-j}$ for $j = 2, 3, \dots, 8$, while keeping the mesh fixed. This placement decreased the size of the cut cells by closer alignment between the interface and the mesh edges. The condition numbers for both methods are listed in Table 4.6. For the unstabilized H^2 method, we see significant increases in the condition number as the cut cells become smaller, whereas for the method with PG stabilization the condition number remains uniformly bounded. This demonstrates the stabilizing effect of the bilinear form $s_h(\cdot, \cdot)$.

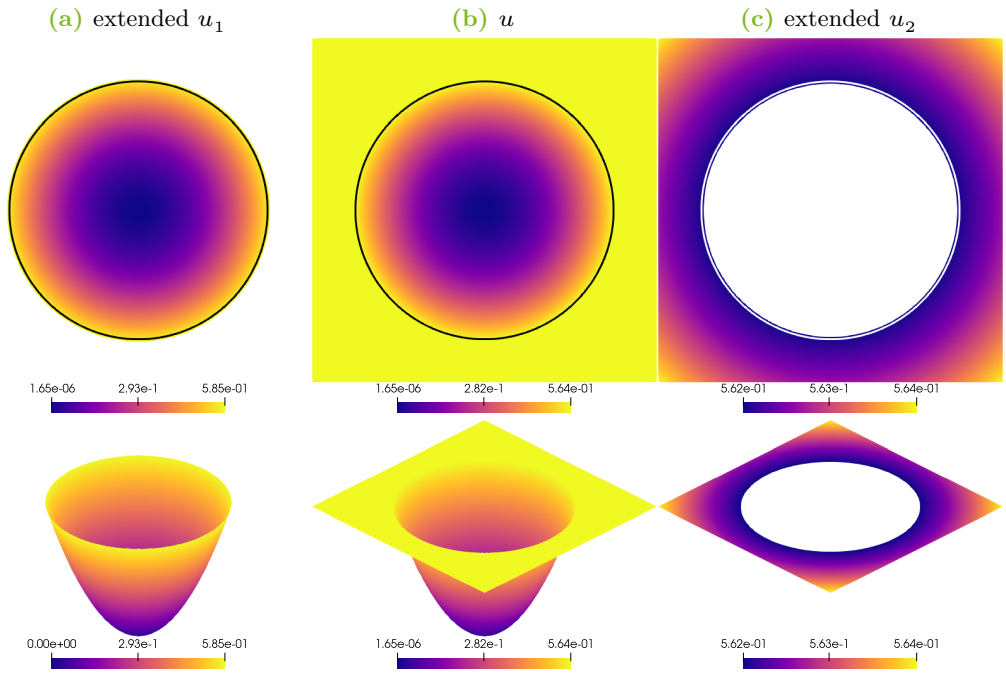

Figure 4.3: Numerical solutions to TP 4.3 (uniform mesh, $h = 1/512$, diffuse-interface method, $\delta = 6h$). First row: top views, the interface is represented by a black/white line. Second row: elevation is proportional to the value of the plotted function.

Table 4.6: Scaled condition numbers κh^2 of the system matrix for different distances between the mesh-cell boundary and the domain boundary.

$\mathrm{dist}(\partial K, \Gamma)$	1e-08	1e-07	1e-06	1e-05	1e-04	1e-03	1e-02
H^2	5.48e13	5.56e11	5.56e09	5.51e07	5.05e05	2.81e03	16.37
$\delta = 0$	22.32	22.32	22.32	22.31	22.23	21.49	15.99

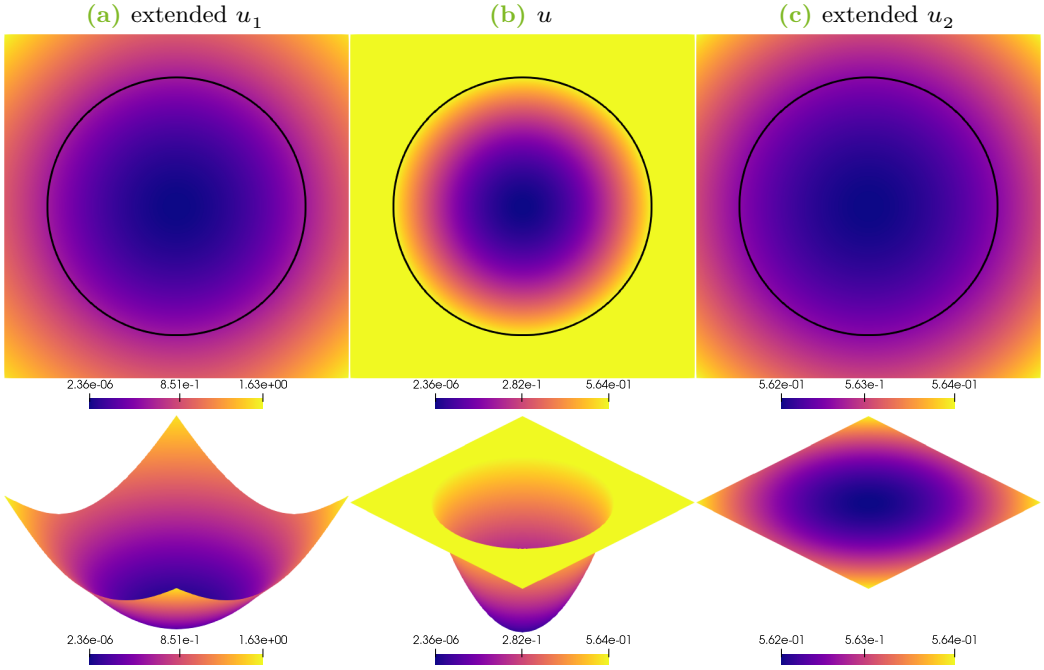

Figure 4.4: Numerical solutions to TP 4.3 (uniform mesh, $h = 1/512$, diffuse-interface method, $\delta = d_\Omega$). First row: top views, the interface is represented by a black line. Second row: elevation is proportional to the value of the plotted function.

4.6 Stationary convection-diffusion problem with steep gradients

In Remark 4.1, we stated that PG stabilization can be naturally extended to problems involving convective terms. Let us now demonstrate this using a stationary convection-diffusion problem with steep gradients. We consider the partial differential equation (PDE)

$$\begin{aligned} \mathbf{v} \cdot \nabla u - \nabla \cdot (\mu \nabla u) &= 0 && \text{in } \Omega_k, \quad k = 1, 2, \\ u &= g_D && \text{on } \partial\Omega, \\ [\![u]\!] &= 0 && \text{on } \Gamma, \\ [\![\mathbf{v}u - \mu \nabla u]\!] &= 0 && \text{on } \Gamma, \end{aligned}$$

where $\mathbf{v} \in \mathbb{R}^d$ is a constant velocity and g_D denotes Dirichlet data on $\partial\Omega$.

To extend the sharp-interface formulation, we add the convective contribution

$$\mathbf{v} \cdot \left[\int_{\Omega_1} \nabla u_{h,1} \phi_{h,1} \mathrm{d}\mathbf{x} + \int_{\Omega_2} \nabla u_{h,2} \phi_{h,2} \mathrm{d}\mathbf{x} \right]$$

to the left-hand side of (4.11). In contrast to pure elliptic interface problems, we now have to introduce a parameter for the stabilization term. Following [VRK25], we scale the stabilization term $s_h(\cdot, \cdot)$ by

$$\beta_h = \max \left\{ 1, \frac{|\mathbf{v}|\, h}{2\mu} \right\}. \tag{4.37}$$

In Example 2 of [JK07], a widely recognized benchmark for stationary convection-diffusion problems is introduced. This problem involves the domain $\Omega = (0, 1)^2$ and the velocity vector $\mathbf{v} = (\cos(-\pi/3), \sin(-\pi/3))^\top$. The Dirichlet boundary data for this problem are given by

$$g_D(x, y) = \begin{cases} 0 & \text{if } x = 1 \text{ or } y \leq 0.7, \\ 1 & \text{otherwise.} \end{cases}$$

Thus, g_D is discontinuous at $(x_0, y_0) = (0, 0.7)$. The interface $\Gamma = \{(x, y) \in \overline{\Omega} : ax + by = c\}$ is the straight line through (x_0, y_0) parallel to $\mathbf{v}$. While in the original setup the diffusion coefficient is constant in Ω, we choose piecewise-constant diffusion coefficients with $\mu_1 = 10^{-3}$ in $\Omega_1 = \{(x, y) \in \Omega : ax + by < c\}$ and $\mu_2 = 10^{-8}$ in $\Omega_2 = \{(x, y) \in \Omega : ax + by > c\}$.

Numerical solutions computed on a uniform mesh with $h = 1/1024$ are depicted in Fig. 4.5. In the plots of the solutions obtained without stabilization and with constant stabilization, we see oscillations in the entire domain, while for β_h computed with (4.37) oscillations occur only in layers at the boundary and interface. These results highlight that failure to adequately stabilize discrete convective terms leads to global spurious oscillations even when the effects caused by small cut cells are cured. On the other hand, stabilizing against cut cells with the proposed parameter β_h also effectively stabilizes the convective terms and confines violations of the discrete maximum principle (DMP) to localized layers of elements with steep gradients. Hence, no further modifications of the discretized weak form are needed. In addition to the localization, the 3D plots in Fig. 4.5 show that the magnitude of undershoots and overshoots is reduced. If strict adherence to the DMP is essential, one may remove such violations entirely using algebraic flux-correction techniques; see, e.g.,[Kuz12; BJK16; Loh+17; HKA19; KQ20; KH23].

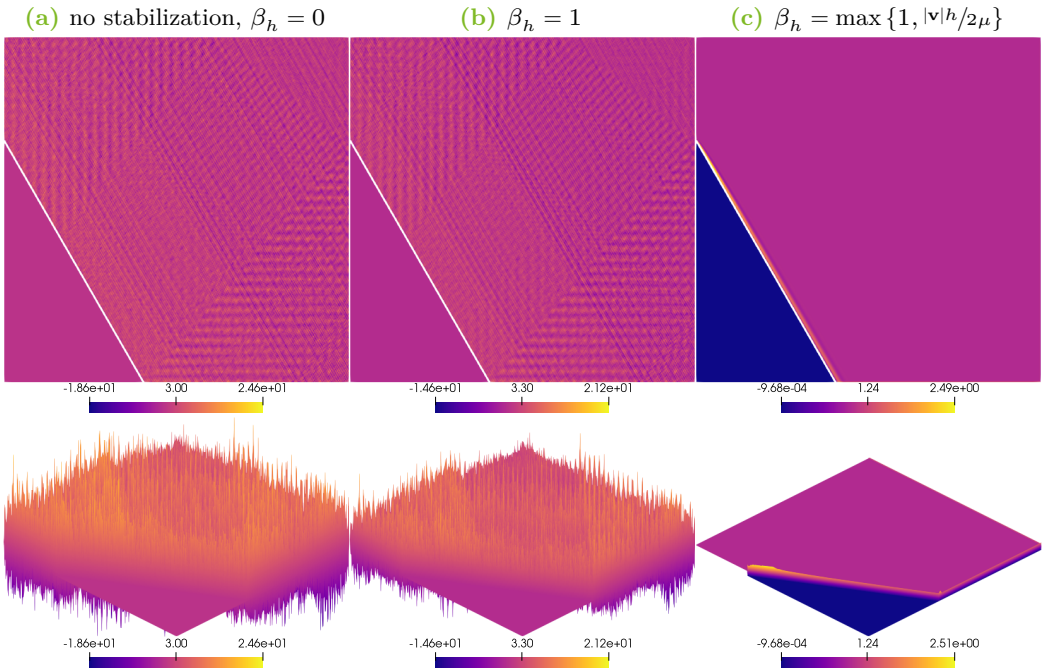

Figure 4.5: Numerical solutions to the stationary interface convection-diffusion problem (uniform mesh, $h = 1/2048$, $\delta = 0$). First row: top views, the interface is represented by a white line. Second row: elevation is proportional to the value of the plotted function.

4.7 High-order finite elements

Let us now conclude this chapter with a high-order extension. As discussed in Section 3.6, the approach using lumped-mass L^2 projection achieves at most second-order accuracy. Following the idea for the high-order extension in PG stabilization for elliptic BVPs, we replace the lumped-mass L^2 projection by nodal averaging to attain higher-order accuracy. Then, the coefficients $\mathbf{g}_{j,k}(u_k)$ of $\mathbf{g}_k(u_k)$ in (4.9) are computed by averaging one-sided limits of the gradient ∇u_k. Let $\mathcal{T}_j$ denote the set of all $K \in \mathcal{T}_h(\delta)$ sharing the node $\mathbf{x}_j$. We define

$$\mathbf{g}_{j,k}(u_k) = \frac{1}{\sum_{K\in\mathcal{T}_j}|K|}\sum_{K\in\mathcal{T}_j}|K|\nabla u_k|_K(\mathbf{x}_j), \quad k = 1,2. \tag{4.38}$$

Recall that for affine elements the definitions for the coefficients in (4.10) and (4.38) coincide. However, for higher-order finite elements, employing nodal averaging ensures optimal accuracy.

Let us now demonstrate that optimal-order accuracy is attainable when using PG stabilization with high-order finite elements. Since the solutions of the previous TPs are piecewise quadratic in x and y, we define a new TP with a piecewise quartic solution and a straight interface.

Test Problem 4.4. *Let $\Omega = (0,1)^2$ and $\Gamma = \{0.51\}\times(0,1)$. For $\mu_1 = 0.5$, $\mu_2 = 2$, $f_1(x,y) = 4(x-0.01)^2$, $f_2(x,y) = {}^{108}/_{11}(x-0.01)^2$ and $u_{ex} = \{u_1, u_2\}$ with*

$$\begin{aligned} u_1(x,y) &= \frac{7}{12}(x-0.01)^2 - \frac{2}{3}(x-0.01)^4, \\ u_2(x,y) &= \frac{25}{176} + \frac{47}{176}(x-0.01)^2 - \frac{9}{22}(x-0.01)^4, \end{aligned}$$

find u such that

$$\begin{aligned} -\nabla\cdot(\mu\nabla u) &= f && \text{in } \Omega, \\ u &= u_{ex} && \text{on } \{0,1\}\times(0,1), \\ \partial_n u &= 0 && \text{on } (0,1)\times\{0,1\}, \\ [\![u]\!] &= 0 && \text{on } \Gamma, \\ [\![\mu\nabla u]\!] &= 0 && \text{on } \Gamma. \end{aligned}$$

We used (4.38) to compute the coefficients and ran grid-convergence studies for the H^2 method and the sharp-interface method with PG stabilization using $\delta = 0$. The L^2 errors and EOCs for polynomial degrees $p = 1,2,3$ are listed in Table 4.7 for the unstabilized method and in Table 4.8 for the stabilized method. In all scenarios, we

see a convergence rate of $p+1$. This indicates that optimal-order convergence is attained for both methods when high-order finite elements are used. Therefore, PG stabilization is effective also for high-order finite element approximations.

Table 4.7: TP 4.4, L^2 convergence history of the unstabilized Nitsche method on uniform meshes for different polynomial approximations.

h^{-1}	H^2	EOC	H^2	EOC	H^2	EOC
	$p=1$		$p=2$		$p=3$	
32	1.67e-04		9.79e-07		3.60e-09	
64	4.19e-05	1.99	1.24e-07	2.98	2.26e-10	3.99
128	1.05e-05	2.00	1.56e-08	2.99	1.42e-11	3.99
256	2.63e-06	2.00	1.95e-09	3.00		
512	6.57e-07	2.00				

Table 4.8: TP 4.4, L^2 convergence history of our stabilized sharp-interface method with $\delta = 0$ on uniform meshes for different polynomial approximations.

h^{-1}	sharp	EOC	sharp	EOC	sharp	EOC
	$p=1$		$p=2$		$p=3$	
32	6.51e-04		9.92e-07		6.05e-09	
64	1.70e-04	1.94	1.24e-07	3.00	3.86e-10	3.97
128	4.35e-05	1.97	1.56e-08	2.99	2.45e-11	3.99
256	1.10e-05	1.98	1.95e-09	3.00		
512	2.77e-06	1.99				

5 Modeling and simulating tumor growth

In Chapter 1, we already discussed the importance of mathematical models to understand tumor dynamics. Taking different influences into account, these models provide insights into different aspects of the tumor growth. In order to fully understand tumor growth, it is not sufficient to formulate mathematical models. It is important to study these models both analytically and numerically. Theoretical studies of the models allow simplifications, yield general predictions and can be used to verify the models. In contrast, numerical studies give us the opportunity to make concrete predictions for specific data. However, before such simulations can be applied in biology or medicine, the numerical schemes must be verified.

In this chapter, we focus on a tumor growth model introduced in [EKS19]. The model describes the nutrient-driven evolution of a tumor while neglecting other influencing factors. In this model, the tumor is taken to consist of two main regions. The inner region, also called the necrotic core, lacks nutrients required for growth and therefore contains mainly dead tumor cells. This necrotic core is surrounded by a thin rim of actively proliferating cells. It is important to note that we do not seek biological accuracy here. We rather establish properties of simple formulations and show how numerical methods can be applied to such problems. While adding to the complexity, additional influencing factors can be incorporated into the model.

In Section 5.1, we introduce the tumor model and employ the concept of formal asymptotic expansions to derive a thin-rim limit model. A rigorous proof for this limit process is given in Section 5.2 for stationary rotationally symmetric solutions. We discretize a generalized form of the thin-rim limit problem using an unfitted finite element method (FEM) in Section 5.3 and adopt the projected gradient (PG) stabilization introduced in Chapter 3. The chapter concludes with numerical examples in Section 5.4. Using some of the test cases introduced in [EKS19], we compare the numerical solutions obtained with our unfitted FEM with PG stabilization to the results obtained with the parametric finite element scheme and the diffuse interface scheme introduced in [EKS19]. In addition, we study the convergence of our method numerically.

5.1 Modeling tumor growth

Let $U \subset \mathbb{R}^d$ be a bounded domain. Within U, let $\Omega(t)$ be a smooth bounded, time-dependent domain that remains compactly contained. By $\Gamma(t)$ we denote the boundary of $\Omega(t)$ and by $\mathbf{n}$ the outer unit normal. We define the space-time domain as $Z = \{(x,t) : x \in \Omega(t)\}$, with its spatial boundary denoted by $\partial Z = \{(x,t) : x \in \Gamma(t)\}$.

Let n and m denote the volume fractions of living and dead tumor cells, respectively. In addition, denote by c the nutrient concentration. Following [EKS19], we can formulate a dimensionless model that describes tumor growth as

$$\begin{aligned}
\partial_t n + \nabla \cdot (\mathbf{v} n) &= (k_b(c) - k_d(c))n && \text{in } Z, && (5.1a)\\
\partial_t m + \nabla \cdot (\mathbf{v} m) &= k_d(c)n - \varepsilon\lambda m && \text{in } Z, && (5.1b)\\
n + m &= 1 && \text{in } Z, && (5.1c)\\
\varepsilon^2 \nabla \cdot (D(n)\nabla c) &= K(c)n && \text{in } Z, && (5.1d)\\
\mathbf{v} &= \frac{-\nabla p}{\mu(n;\varepsilon)} && \text{in } Z, && (5.1e)\\
n(\cdot, 0) &= 1 && \text{in } \Omega(0), && (5.1f)\\
c &= 1 && \text{on } \partial Z, && (5.1g)\\
p &= -\varepsilon^2 \gamma(n)\kappa && \text{on } \partial Z, && (5.1h)\\
q_{\mathbf{n}} &= \mathbf{v} \cdot \mathbf{n} && \text{on } \partial Z. && (5.1i)
\end{aligned}$$

Biological interpretations of the functions and variables are provided in Table 5.1.

This model describes the nutrient-driven birth and death of tumor cells, as well as the degradation of necrotic cells. Since the nutrient transport occurs on a faster time scale than proliferation and death of cells, we treat this problem as quasi-steady. The dynamic evolution of the tumor is driven by the pressure within the tumor.

In (5.1), we introduced the scaling parameter ε leading to a distinguished limit model as $\varepsilon \to 0$. Additionally, we assume

$$\mu(n;\varepsilon) \sim \mu_0(n) \text{ for } n = O(1), n > 0, \quad \mu(0;\varepsilon) \sim \varepsilon\mu_1 \text{ as } \varepsilon \to 0, \tag{5.2}$$

with a constant μ_1 to converge to that limit. This assumption is justified by the observation that necrotic material exhibits significantly lower viscosity compared to living tissue.

Before we derive a limit model by employing formal asymptotic expansions, we establish bounds for the densities of living tumor cells n and necrotic tumor cells m.

Table 5.1: Biological interpretations in (5.1).

n	volume fraction of living tumor cells
m	volume fraction of dead tumor cells
c	nutrient concentration within the tumor
$\Omega(t)$	tumor area
$\Gamma(t)$	tumor boundary
k_b	cellular birth rate (increasing in c)
k_d	cellular death rate (decreasing in c)
$\varepsilon\lambda$	degradation rate of dead cells
$K(c)/\varepsilon^2$	nutrient consumption rate
$D(n)$	nutrient diffusivity
$\mu(n;\varepsilon)$	tissue viscosity
$\varepsilon^2\gamma(n)$	cell-cell adhesion
$\mathbf{v}$	velocity field of the tissue movement
p	tissue pressure within the tumor
κ	mean curvature of tumor boundary, negative for spheres
$\mathbf{n}$	unit outward normal of the tumor boundary
$q_{\mathbf{n}}$	normal velocity of the tumor boundary
ε	scaling parameter

Proposition 5.1. *If $0 \leq n \leq 1$ for $t = 0$, then*

$$0 \leq n \leq 1 \quad \textit{almost everywhere in } \Omega(t).$$

Proof. By adding equations (5.1a) and (5.1b), and using the constraint (5.1c), we obtain

$$\nabla \cdot \mathbf{v} = k_b(c)n - \varepsilon\lambda(1-n). \tag{5.3}$$

Substituting this into (5.1a) yields

$$\partial_t n + \mathbf{v} \cdot \nabla n = -k_d(c)n + n(1-n)(k_b(c) + \varepsilon\lambda). \tag{5.4}$$

Let $f : \mathbb{R} \to \mathbb{R}$ be an arbitrary Lipschitz function. For the time derivative of the integral of $f(n)$ over the domain $\Omega(t)$ + we obtain

$$\begin{aligned}
\frac{\mathrm{d}}{\mathrm{d}t}\int_{\Omega(t)} f(n) &= \int_{\Gamma(t)} f(n)\mathbf{v}\cdot\mathbf{n} + \int_{\Omega(t)} f'(n)\partial_t n \\
&= \int_{\Omega(t)} f'(n)\partial_t n + \nabla\cdot(f(n)\mathbf{v}) \\
&= \int_{\Omega(t)} f'(n)(\partial_t n + \nabla n\cdot\mathbf{v}) + f(n)\nabla\cdot\mathbf{v}.
\end{aligned}$$

Substituting (5.3) and (5.4) into this expression yields

$$\begin{aligned}\frac{\mathrm{d}}{\mathrm{d}t}\int_{\Omega(t)} f(n) = \int_{\Omega(t)} &[-k_d(c)nf'(n) + k_b(c)n\left((1-n)f'(n) + f(n)\right) \\ &+\varepsilon\lambda(1-n)\left(nf'(n) - f(n)\right)].\end{aligned} \tag{5.5}$$

To establish bounds for n, we first choose $f(n) = (n-1)_+ = \max(0, n-1)$. Substituting this specific choice into (5.5), we obtain

$$\frac{\mathrm{d}}{\mathrm{d}t}\int_{\Omega(t)} (n-1)_+ = \int_{\Omega(t)} -\left(k_d(c)n - \varepsilon\lambda(1-n)\right)\chi_{\{n>1\}} \leq 0,$$

where $\chi_{\{n>1\}}$ is the indicator functions that equals 1 when $n > 1$ and 0 otherwise. Since the time derivative of the integral is nonpositive, it follows that $n \leq 1$ almost everywhere in $\Omega(t)$ for all $t > 0$ if $n \leq 1$ almost everywhere in $\Omega(0)$. To derive a lower bound for n we choose $f(n) = (-n)_+ = \max(0, -n)$. Substituting this into (5.5), we find

$$\begin{aligned}\frac{\mathrm{d}}{\mathrm{d}t}\int_{\Omega(t)} (-n)_+ &= \int_{\Omega(t)} \left(k_d(c)n - k_b(c)n\right)\chi_{\{n<0\}} \\ &= \int_{\Omega(t)} -\left(k_d(c) - k_b(c)\right)(-n)_+ \\ &\leq \int_{\Omega(t)} \left(k_d(c) - k_b(c)\right)_- (-n)_+.\end{aligned}$$

This implies that if $n \geq 0$ holds almost everywhere in $\Omega(0)$, this property remains valid for all subsequent times $t > 0$. Combining these two bounds for n, we obtain $0 \leq n \leq 1$ almost everywhere in $\Omega(t)$, provided these bounds are satisfied initially. □

This proposition, together with (5.1c), gives us the same result for the density of dead tumor cells m.

Corollary 5.2. *If $0 \leq m \leq 1$ holds for $t = 0$, then*

$$0 \leq m \leq 1 \quad \textit{almost everywhere in } \Omega(t).$$

Let us now derive the limit problem as $\varepsilon \to 0$. We follow the derivation given in [EKS19] and refine some of the arguments therein. Before we start, we note that the asymptotic structure of the problem consists of two distinct regions: a boundary layer near the tissue edge and a core region. In this framework, nutrient

consumption leads to a concentration of living tumor cells within the boundary layer, while dead tumor cells dominate in the necrotic core region.

In a first step, we perform a time rescaling $t \rightsquigarrow \frac{t}{\varepsilon}$. This rescaling also implies $\mathbf{v} \rightsquigarrow \varepsilon\mathbf{v}$, $q_{\mathbf{n}} \rightsquigarrow \varepsilon q_{\mathbf{n}}$, and $p \rightsquigarrow \varepsilon^2 p$. For clarity, we introduce new variables for these rescaled quantities. We write

$$p = \varepsilon^2 P, \quad \mathbf{v} = \varepsilon \mathbf{V}, \quad q_{\mathbf{n}} = \varepsilon Q_{\mathbf{n}}.$$

We observe that $Q_{\mathbf{n}}$ depends only on the position along the interface and on time t. Furthermore, $Q_{\mathbf{n}}$ is assumed to be constant in the normal direction away from the interface $\Gamma(t)$.

Using this rescaling in (5.1), we obtain

$$\begin{aligned}
\varepsilon \partial_t n + \varepsilon \nabla \cdot (\mathbf{V} n) &= (k_b(c) - k_d(c))n && \text{in } Z, && \text{(5.6a)}\\
\varepsilon \partial_t m + \varepsilon \nabla \cdot (\mathbf{V} m) &= k_d(c) n - \varepsilon \lambda m && \text{in } Z, && \text{(5.6b)}\\
n + m &= 1 && \text{in } Z, && \text{(5.6c)}\\
\varepsilon^2 \nabla \cdot (D(n) \nabla c) &= K(c) n && \text{in } Z, && \text{(5.6d)}\\
\mathbf{V} &= \frac{-\varepsilon \nabla P}{\mu(n;\varepsilon)} && \text{in } Z, && \text{(5.6e)}\\
n(\cdot, 0) &= 1 && \text{in } \Omega(0), && \text{(5.6f)}\\
c &= 1 && \text{on } \partial Z, && \text{(5.6g)}\\
P &= -\gamma(n)\kappa && \text{on } \partial Z, && \text{(5.6h)}\\
Q_{\mathbf{n}} &= \mathbf{V} \cdot \mathbf{n} && \text{on } \partial Z. && \text{(5.6i)}
\end{aligned}$$

In particular, this implies

$$-\varepsilon^2 \nabla \cdot \frac{1}{\mu(n;\varepsilon)} \nabla P = \varepsilon \nabla \cdot \mathbf{V} = k_b(c) n - \varepsilon \lambda (1 - n), \tag{5.7}$$

$$\varepsilon \partial_t n + \varepsilon \mathbf{V} \cdot \nabla n = -k_d(c) n + n(1-n)(k_b(c) + \varepsilon \lambda). \tag{5.8}$$

The second equality in (5.7) is derived by adding equation (5.6a) to equation (5.6b), while the first equality in (5.7) is obtained by calculating the divergence of the velocity field from equation (5.6e). To derive equation (5.8), we substitute the second equality from (5.7) into equation (5.6a).

We now consider a family of solutions to (5.6), characterized by a smooth evolution of domains $(\Omega_\varepsilon(t))_{t>0}$ with smooth boundaries $\Gamma_\varepsilon(t)$, normal velocity fields $Q_{\mathbf{n},\varepsilon}$, and functions n_ε, m_ε, $\mathbf{V}_\varepsilon$, P_ε, and c_ε defined on the spatial domain Z_ε.

To study the asymptotic behavior as $\varepsilon \to 0$, we assume that the solution components can be expressed using formal asymptotic expansions. Specifically, we represent $n_\varepsilon(x,t)$ away from the interface $\Gamma_\varepsilon(t)$ by an outer expansion

$$n_\varepsilon(x,t) = n_o^{(0)}(x,t) + \varepsilon n_o^{(1)}(x,t) + \varepsilon^2 n_o^{(2)}(x,t) + ...$$

where $n_o^{(i)}(x,t)$ are smooth functions representing successive terms in the expansion.

In addition, we assume that $n_\varepsilon(x,t)$ can be described by an inner expansion

$$n_\varepsilon(x,t) = n^{(0)}(\xi,y,t) + \varepsilon n^{(1)}(\xi,y,t) + \varepsilon^2 n^{(2)}(\xi,y,t) + ...$$

within a small neighborhood of $\Gamma_\varepsilon(t)$. Here, y denotes the projection of the point x onto the interface $\Gamma_\varepsilon(t)$, while

$$\xi = \frac{d_\varepsilon(x,t)}{\varepsilon},$$

where $d_\varepsilon(x,t) = -\operatorname{dist}(x,\Gamma_\varepsilon(t))$, is the negative distance of x to the interface, scaled by $\varepsilon > 0$.

A similar formal expansion, again with respect to $\Gamma_\varepsilon(t)$, is assumed for the other solution components $m_\varepsilon(x,t)$, $\mathbf{V}_\varepsilon(x,t)$, $P_\varepsilon(x,t)$, and $c_\varepsilon(x,t)$.

Finally, we assume that $\Gamma_\varepsilon(t)$ converges to some smooth evolution of hypersurfaces $(\Gamma(t))_{t>0}$. Consequently, the signed distance function (SDF) $d_\varepsilon(x,t)$ can be expressed as $d_\varepsilon(x,t) = d_0(x,t) + O(\varepsilon)$, where $d_0(x,t)$ represents the negative distance to $\Gamma(t)$. We will see below that only the zeroth-order term d_0 and geometric quantities of $\Gamma(t)$ contribute up to the relevant order. For simplicity, we omit explicit references to ε-dependence in these quantities and write, for example, d instead of d_ε.

Using the fact that $\partial_t d(x,t) = -Q_{\mathbf{n}}(y(x),t)$, we obtain for the time derivative of the inner expansion of n_ε

$$\varepsilon \partial_t n_\varepsilon = \partial_\xi n^{(0)} \partial_t d + O(\varepsilon) = \partial_\xi(-Q_{\mathbf{n}} n^{(0)}) + O(\varepsilon).$$

Additionally, using $V_{\mathbf{n}}(\xi,y,t) = \mathbf{V}^{(0)}(\xi,y,t)\cdot\mathbf{n}(y,t)$, where $V_{\mathbf{n}}$ represents the normal component of the velocity at leading order, yields

$$\begin{aligned}\varepsilon\nabla\cdot(\mathbf{V}_\varepsilon n_\varepsilon) &= \varepsilon(\partial_\xi(\mathbf{V}_\varepsilon n_\varepsilon))\cdot\nabla\xi \\ &= \mathbf{n}\cdot\partial_\xi(n^{(0)}\mathbf{V}^{(0)}) + O(\varepsilon) = \partial_\xi(n^{(0)}V_{\mathbf{n}}) + O(\varepsilon).\end{aligned}$$

Introducing $W_{\mathbf{n}}(\xi, y, t) = V_{\mathbf{n}}(\xi, y, t) - Q_{\mathbf{n}}(y, t)$, equations (5.6a)–(5.6c) then yield in terms of inner expansions to leading order

$$\partial_\xi(W_{\mathbf{n}} n^{(0)}) = (k_b(c^{(0)}) - k_d(c^{(0)}))n^{(0)}, \tag{5.9a}$$

$$\partial_\xi(W_{\mathbf{n}} m^{(0)}) = k_d(c^{(0)})n^{(0)}, \tag{5.9b}$$

$$n^{(0)} + m^{(0)} = 1, \tag{5.9c}$$

and in particular

$$\partial_\xi W_{\mathbf{n}} = k_b(c^{(0)})n^{(0)}. \tag{5.10}$$

According to the definition above, $W_{\mathbf{n}}$ depends solely on the signed distance ξ to the interface $\Gamma(t)$. In contrast, $V_{\mathbf{n}}$ and P depend not only on the distance to the interface but also on the position along the interface and the time t. This is a consequence of the decoupling of P and hence of the Galilean invariance of the problem.

Using an analogous expansion for the nutrient diffusion, we obtain

$$\varepsilon^2 \nabla \cdot (D(n_\varepsilon)\nabla c_\varepsilon) = \partial_\xi(D(n^{(0)})\partial_\xi c^{(0)}) + O(\varepsilon).$$

Substituting this result into equation (5.6d), we find

$$\partial_\xi(D(n^{(0)})\partial_\xi c^{(0)}) = K(c^{(0)})n^{(0)}.$$

Next, assuming $n^{(0)} > 0$ and using (5.2), we derive from (5.6e)

$$\mathbf{V}^{(0)} = \frac{-1}{\mu_0(n^{(0)})}\varepsilon\partial_\xi P^{(0)}\nabla\xi = \frac{-1}{\mu_0(n^{(0)})}\partial_\xi P^{(0)}\mathbf{n}.$$

Consequently, the normal component of the velocity is

$$\mathbf{V}_{\mathbf{n}} = \frac{-1}{\mu_0(n^{(0)})}\partial_\xi P^{(0)}, \tag{5.11}$$

and by (5.7)

$$-\partial_\xi\left(\frac{1}{\mu_0(n^{(0)})}\partial_\xi P^{(0)}\right) = k_b(c^{(0)})n^{(0)}.$$

The boundary conditions (5.6g)–(5.6i) imply at $\xi = 0$

$$c^{(0)} = 1, \qquad P^{(0)} = -\gamma(n^{(0)})\kappa, \qquad W_{\mathbf{n}} = 0.$$

Using equation (5.9a) together with (5.10), we obtain for $n^{(0)}(0) = n^{(0)}(0, y, t)$ from the boundary conditions

$$\begin{aligned}(k_b(1) - k_d(1))n^{(0)}(0) &= (\partial_\xi(W_{\mathbf{n}} n^{(0)}))(0)\\ &= (\partial_\xi W_{\mathbf{n}})(0)n^{(0)}(0) + W_{\mathbf{n}}(0)(\partial_\xi n^{(0)})(0)\\ &= k_b(1)n^{(0)}(0)n^{(0)}(0).\end{aligned}$$

From this, and using equation (5.9c), we deduce

$$n^{(0)}(0) = \frac{k_b(1) - k_d(1)}{k_b(1)}, \qquad m^{(0)}(0) = \frac{k_d(1)}{k_b(1)}.$$

In what follows we write γ_0 for $\gamma(n^{(0)})$.

For simplicity, we drop the index (0) and denote the derivative with respect to ξ by a prime. We derive the system

$$\begin{aligned} W_{\mathbf{n}} n' &= k_b(c)n(1-n) - k_d(c)n, \\ W_{\mathbf{n}}' &= k_b(c)n, \\ -(D(n)c')' &= -K(c)n, \end{aligned}$$

to be solved in the domain $(-\infty, 0)$, subject to the boundary conditions

$$n(0) = \frac{k_b(1) - k_d(1)}{k_b(1)}, \quad c(0) = 1, \quad W_{\mathbf{n}}(0) = 0, \quad W_{\mathbf{n}}'(0) = k_b(1) - k_d(1).$$

Formally, this is the required number of boundary conditions for a well-posed system. We therefore expect unique solutions $n, W_{\mathbf{n}}, c$, and $m = 1 - n$ that depend solely on ξ.

For these solutions, we anticipate the following asymptotic behavior as $\xi \to -\infty$:

$$n \to 0, \quad m \to 1, \quad c \to c_\infty, \quad W_{\mathbf{n}} \to -Q,$$

where $c_\infty > 0$ and $Q > 0$ are positive constants that must be determined as part of solving the system.

Let us now turn our attention to the pressure P. By (5.11) we have

$$P' = -\mu_0(n)V_\nu.$$

Integrating this equation over $(\xi, 0)$ yields

$$-\gamma_0\kappa - P(\xi) = \int_\xi^0 -\mu_0(n)V_{\mathbf{n}}.$$

Using the relation $V_{\mathbf{n}} = Q_{\mathbf{n}} + W_{\mathbf{n}}$ we obtain

$$\begin{aligned} P(\xi) &= \int_\xi^0 \mu_0(n(\zeta))(Q_{\mathbf{n}} + W_{\mathbf{n}}(\zeta))\mathrm{d}\zeta - \gamma_0\kappa \\ &= Q_{\mathbf{n}} \int_\xi^0 \mu_0(n(\zeta))\mathrm{d}\zeta + \int_\xi^0 \mu_0(n(\zeta))W_{\mathbf{n}}(\zeta)\mathrm{d}\zeta - \gamma_0\kappa, \end{aligned}$$

since $Q_{\mathbf{n}}$ is independent of ξ. For $\xi \to -\infty$ we have

$$P \to aQ_{\mathbf{n}} - b - \gamma_0 \kappa,$$

with positive constants

$$a = \int_{-\infty}^{0} \mu_0(n(\zeta))\mathrm{d}\zeta, \quad b = -\int_{-\infty}^{0} \mu_0(n(\zeta))W_{\mathbf{n}}(\zeta)\mathrm{d}\zeta.$$

This completes the inner expansion.

We now proceed with the outer expansion, focusing on the region far from the interface $\Gamma(t)$. In this outer region, the living tumor cell density n is small in orders of ε, which implies $n_o^{(0)} = 0$. This is indeed justified since $n \to 0$ for $\xi \to -\infty$ in the inner expansion. Consequently, we derive the governing equations for the outer variables to leading order as

$$\nabla \cdot \mathbf{V}_o^{(0)} = -\lambda, \tag{5.12}$$

$$\mathbf{V}_o^{(0)} = \frac{-\nabla P_o^{(0)}}{\mu_1}, \tag{5.13}$$

and

$$\Delta c_o^{(0)} = 0.$$

The solutions in this outer region are expected to smoothly transition into those of the inner region near $\Gamma(t)$, ensuring consistency between both expansions. Therefore, matching with the inner expansion gives us the boundary conditions $c_o^{(0)} = c_\infty$ and

$$\mathbf{V}_o^{(0)} \cdot \mathbf{n} = Q_{\mathbf{n}} - Q, \tag{5.14}$$

$$P_o^{(0)} = aQ_{\mathbf{n}} - b - \gamma_0 \kappa. \tag{5.15}$$

Thus, by dropping the subscript index o and superscript index (0), we have for c that it is constant with $c = c_\infty$. Translating (5.12)–(5.13) and (5.14)–(5.15) by b, we obtain for the tissue pressure P

$$\begin{aligned} \Delta P &= \lambda\mu_1 && \text{in } \Omega(t), \\ Q_{\mathbf{n}} &= \mathbf{V} \cdot \mathbf{n} + Q && \text{on } \Gamma(t), \\ P &= aQ_{\mathbf{n}} - \gamma_0 \kappa && \text{on } \Gamma(t). \end{aligned}$$

Rewriting the boundary conditions and using (5.13) yields

$$\Delta P = \lambda\mu_1 \qquad \text{in } \Omega(t), \tag{5.16a}$$

$$\frac{P}{a} + \frac{1}{\mu_1}\partial_{\mathbf{n}} P + \frac{\gamma_0\kappa}{a} = Q \qquad \text{on } \Gamma(t), \tag{5.16b}$$

$$Q_{\mathbf{n}} = \frac{P}{a} + \frac{\gamma_0\kappa}{a} \qquad \text{on } \Gamma(t). \tag{5.16c}$$

Finally, with $u = P$, $\alpha = a$, $V = Q_{\mathbf{n}}$, $\beta = \gamma_0/a$ and scaling such that $\mu_1 = \lambda = 1$ we derive

$$\Delta u = 1 \qquad \text{in } \Omega(t), \tag{5.17a}$$

$$\nabla u \cdot \mathbf{n} + \frac{u}{\alpha} + \beta\kappa = Q \qquad \text{on } \Gamma(t), \tag{5.17b}$$

$$V = \frac{u}{\alpha} + \beta\kappa \qquad \text{on } \Gamma(t). \tag{5.17c}$$

The biological interpretations of the variables in this thin-rim limit are listed in Table 5.2.

Table 5.2: Biological interpretations in (5.17).

u	tissue pressure within the tumor
$\Omega(t)$	tumor area
$\Gamma(t)$	tumor boundary
V	normal velocity of the tumor boundary
κ	mean curvature of the tumor boundary, negative for spheres
$\mathbf{n}$	unit outward normal of the tumor boundary
α,β, Q	positive constants depending on (5.1)

To analyze the behavior of the tumor model described by (5.1), we focus on studying the thin-rim limit problem (5.17). A finite element discretization of this limit problem is presented in Section 5.3. Subsequently, numerical studies demonstrating the behavior and properties of the mathematical model are performed in Section 5.4.

5.2 Rigorous proof of the thin-rim limit in stationary rotational symmetric case

We now aim to prove the convergence of solutions of (5.1) to solutions of (5.17). For this rigorous proof, we restrict ourselves to the case of stationary rotationally symmetric solutions and specific choices for the rates.

We begin with the derivation of the stationary rotationally symmetric form of (5.1) and assume that $R_{\min} \le R = R_\varepsilon \le R_{\max}$ for $\varepsilon > 0$. First, we derive the rotationally symmetric form of (5.1). As in Section 5.1, we apply a time rescaling $t \rightsquigarrow \frac{t}{\varepsilon}$ and let Z denote the space-time domain $Z = \{(r,t) : r \in (0, R(t))\}$, where r represents the radial coordinate. For rotationally symmetric solutions of equation (5.6), we consider functions depending only on r and t. We formulate (5.6) in the rotationally symmetric form as

$$
\begin{aligned}
\varepsilon \partial_t n + \varepsilon \frac{1}{r} \partial_r (rvn) &= (k_b(c) - k_d(c))n && \text{in } Z,\\
\varepsilon \partial_t m + \varepsilon \frac{1}{r} \partial_r (rvm) &= k_d(c)n - \varepsilon \lambda m && \text{in } Z,\\
n + m &= 1 && \text{in } Z,\\
\varepsilon^2 \frac{1}{r} \partial_r (rD(n)\partial_r c) &= K(c)n && \text{in } Z,\\
v &= \frac{-\varepsilon \partial_r p}{\mu(n;\varepsilon)} && \text{in } Z,\\
n(\cdot, 0) &= 1 && \text{in } (0, R(0)),\\
c(R(\cdot), \cdot) &= 1 && \text{in } (0, \infty),\\
p(R(\cdot), \cdot) &= \gamma(n) \frac{1}{R(\cdot)} && \text{in } (0, \infty),\\
q(\cdot) &= v(R(\cdot)) && \text{in } (0, \infty).
\end{aligned}
$$

Here, we write $n = n_\varepsilon(r,t)$ and similarly for m, c, and p. The radial velocity field is denoted by $v = v(r,t)$, which now depends only on the radial coordinate r and time t. To simplify notation in the following presentation, we denote radial derivatives by a prime. Owing to the rotational symmetry and regularity assumptions, the conditions

$$
c'(0) = p'(0) = 0
$$

hold at the center $r = 0$. These boundary conditions reflect the fact that there is no flux at the center of symmetry in a radially symmetric configuration.

In the case of stationary solutions, we derive

$$\varepsilon \frac{1}{r}(rvn)' = (k_b(c) - k_d(c))n \quad \text{in } (0,R), \tag{5.18a}$$

$$\varepsilon \frac{1}{r}(rvm)' = k_d(c)n - \varepsilon\lambda m \quad \text{in } (0,R), \tag{5.18b}$$

$$n + m = 1 \quad \text{in } (0,R), \tag{5.18c}$$

$$\varepsilon^2 \frac{1}{r}(rD(n)c')' = K(c)n \quad \text{in } (0,R), \tag{5.18d}$$

$$v = \frac{-\varepsilon p'}{\mu(n;\varepsilon)} \quad \text{in } (0,R). \tag{5.18e}$$

These equations are subject to the boundary conditions

$$c(R) = 1, \quad p(R) = \gamma(n)\frac{1}{R}, \quad v(R) = 0, \tag{5.19a}$$

$$c'(0) = p'(0) = 0. \tag{5.19b}$$

By adding (5.18a) to (5.18b) and using the identity (5.18c), we derive

$$\varepsilon \frac{1}{r}(rv)' = k_b(c)n - \varepsilon\lambda(1-n) \quad \text{in } (0,R). \tag{5.20}$$

On the other hand, for the limit system (5.16) without rescaling we derive in the case of stationary solutions

$$\begin{aligned} \Delta P &= \lambda\mu_1 && \text{in } \Omega, \\ P &= -\gamma_0\kappa && \text{on } \Gamma, \\ 0 &= Q - \frac{1}{\mu_1}\partial_{\mathbf{n}} P && \text{on } \Gamma. \end{aligned}$$

Therefore, in the rotational symmetric case, these equations reduce to

$$\frac{1}{r}(rP')' = \lambda\mu_1 \quad \text{in } (0,R_*), \tag{5.21a}$$

$$P(R_*) = \frac{\gamma_0}{R_*}, \tag{5.21b}$$

$$P'(R_*) = \mu_1 Q, \tag{5.21c}$$

$$P'(0) = 0. \tag{5.21d}$$

In what follows, we make some assumptions on the coefficients. In particular, we assume that

(A1) D is uniformly bounded from above and below,

(A2) $k_b(c) = H(c - c_b)$ with $1 > c_b > 0$,

(A3) $k_d(c) = 1 - \sigma H(c - c_d)$ with $1 > c_d > c_b > 0$, $1 > \sigma > 0$,

(A4) $K(c) = \omega(c) + \beta k_b(c)$ with $\omega(0) = 0$, $\omega(c) > 0$ for $c > 0$, and $\omega(c) < 0$ for $c < 0$,

(A5) $\mu(n; \varepsilon) = \mu_0 n + \varepsilon \mu_1$.

Remark 5.1. *These assumptions are motivated by a similar tumor growth model postulated in [WK97]. The proof of Theorem 5.3 will indeed show that some assumptions like (A1)–(A5) are necessary for the validity of the result.*

Let us now introduce the concept of weak-star convergence. For a Banach space X, we denote the dual space of X, i.e., the space of linear functionals on X, by $X' = \mathcal{L}(X; \mathbb{R})$. For a sequence in X' we define weak-star convergence as follows; see, e.g., [Alt16]).

Definition 5.1. *Let $(x'_k)_{k\in\mathbb{N}} \subset X'$. The sequence converges weak-star to $x' \in X'$ for $k \to \infty$ if for all $x \in X$*

$$x'_k(x) \to x'(x) \quad \text{for } k \to \infty.$$

We write

$$x'_k \overset{*}{\rightharpoonup} x' \quad \text{for } k \to \infty.$$

Next, we use the concept of weak-star convergence in the space $X' = L^\infty(0, R)$ as the dual space of $L^1(0, R)$.

We are now ready to formulate our key result.

Theorem 5.3. *Let Assumptions (A1)–(A5) hold. Assume that $R_{\min} \le R = R_\varepsilon \le R_{\max}$, $0 \le n_\varepsilon \le 1$, and $n_\varepsilon(R) > 0$ for $\varepsilon > 0$. For the sequence of the pressure component $(p_\varepsilon)_\varepsilon$ of solutions of (5.18) subject to (5.19) there exists a subsequence, also denoted by $(p_\varepsilon)_\varepsilon$, such that for $\varepsilon \to 0$ we have*

$$p_\varepsilon \overset{*}{\rightharpoonup} p$$

in $L^\infty(0, R)$, where p is a translation of the solution P of (5.21) and Q compatible to (5.18) and (5.19) is given.

The assumptions on n are motivated by the biological interpretation of this variable as well as by Proposition 5.1. Particularly, $n \leq 1$ follows directly from the proof of Proposition 5.1.

We also obtain results for the convergence of other components of the solutions; these results are given below. To improve readability and ensure clarity, we divide the proof of Theorem 5.3 into several parts. First, we prove certain properties and bounds for the components of the solutions of (5.18). These results serve as foundations to deduce the convergence to solutions of the limit problem (5.21).

In the following lemmas, we assume that m, n, c, p, v are the components of the solution of (5.18). For brevity, we omit the general assumptions on R and n in the lemmas; however, these assumptions are the same as in Theorem 5.3. We begin with an explicit representation for the nutrient concentration c and establish some properties.

Lemma 5.4. *Let Assumptions (A1), (A2), and (A4) hold. The nutrient concentration c is monotone increasing and is explicitly given as*

$$c(r) = 1 - \frac{1}{\varepsilon^2} \int_r^R \frac{1}{D(n(s))s} \int_0^s \rho(K(c)n)(\rho) \mathrm{d}\rho \mathrm{d}s. \tag{5.22}$$

In addition, $0 \leq c \leq 1$.

Proof. Integrating equation (5.18d) over the interval $(0, r)$, we obtain

$$\varepsilon^2 (D(n)c')(r) = \frac{1}{r} \int_0^r \rho(K(c)n)(\rho) \mathrm{d}\rho.$$

Performing an additional integration of this result over the interval (r, R), we derive the explicit representation

$$c(r) = 1 - \frac{1}{\varepsilon^2} \int_r^R \frac{1}{D(n(s))s} \int_0^s \rho(K(c)n)(\rho) \mathrm{d}\rho \mathrm{d}s.$$

This expression establishes (5.22).

To show that $c \geq 0$ holds, assume there exists a point $r_1 > 0$ such that $c(r_1) = 0$. Then it follows from Assumptions (A4) and (A2) that $K(c(r_1)) = \omega(c(r_1)) = 0$. Furthermore, assume $c(r) \leq 0$ for $0 \leq r < r_1$ and hence $K(c(r)) = \omega(c(r)) \leq 0$. Using the explicit representation of c' and Assumption (A1), we find $c'(r) \leq 0$ for $0 \leq r < r_1$. This implies $c(r) = 0$ for $0 \leq r < r_1$. Next, assume we have $0 < r_1 < r_2$ with $c(r_1) = c(r_2) = 0$, $c(r) < 0$ for $r_1 < r < r_2$ and $c(r) \geq 0$ for $0 < r \leq r_1$. Then

we have with the explicit representation of c' and Assumption (A1) that $c'(r_1) \geq 0$. This is a contradiction to the assumption. Since the boundary condition (5.19a) gives $c(R) > 0$, we conclude that $c(r) \geq 0$ for $0 \leq r \leq R$.

Additionally, the explicit representation of $c(r)$ implies that $c(r)$ is monotone increasing in r. Hence, the maximum is reached at $R = r$. Since the boundary condition (5.19a) specifies $c(R) = 1$, we conclude $c(r) \leq 1$ for all $r \in (0, R)$. Combining these results establishes the bounds $0 \leq c \leq 1$ □

Additionally, (5.22) implies

$$c(r) = 1 - \frac{1}{\varepsilon^2} \int_0^R \rho K(c(\rho)) n(\rho) \int_{\max(r,\rho)}^R \frac{1}{sD(n(s))} \mathrm{d}s\mathrm{d}\rho \tag{5.23}$$

Now we focus on the velocity. Before we derive bounds for v, we note that integrating (5.20) over $(0, r)$ yields

$$\varepsilon r v(r) = \int_0^r s k_b(c(s)) n(s) - s\varepsilon\lambda(1 - n(s))\mathrm{d}s. \tag{5.24}$$

Lemma 5.5. *Let Assumptions (A1)–(A4) apply. For the radial velocity v there exists $v_{\min}$ independent of ε, such that $v_{\min} \leq v \leq 0$.*

Proof. Integrating equation (5.18a) over $(0, r)$, we obtain

$$\varepsilon r(vn)(r) = \int_0^r s(k_b(c(s)) - k_d(c(s)))n(s)\mathrm{d}s. \tag{5.25}$$

The monotonicity of $c(r)$, combined with the assumptions (A2) and (A3), implies that $k_b(c(s)) - k_d(c(s))$ is monotone increasing in s. Using the boundary condition (5.19a), together with equation (5.25), we obtain

$$0 = \int_0^R s(k_b(c(s)) - k_d(c(s)))n(s)\mathrm{d}s.$$

This integral equality implies that there exists a $c_* \in (c(0), c(R))$ such that

$$\begin{cases} k_b(c) - k_d(c) < 0 & c < c_*, \\ k_b(c) - k_d(c) \geq 0 & c > c_*. \end{cases}$$

Thus, there exists a minimal point $r_* \in (0, R)$, where $c(r_*) = c_*$. In view of this result, the right-hand side of equation (5.25) is decreasing for $r < r_*$ and

nondecreasing for $r > r_*$, while for $r = 0$ and $r = R$, due to the boundary conditions, the right-hand side is equal to zero. Since $n(r), r, \varepsilon \geq 0$, it follows from (5.25) that $v(r) \leq 0$.

In (5.24), we estimate

$$\begin{aligned} \varepsilon r v(r) &= \int_0^r s k_b(c(s)) n(s) - s\varepsilon\lambda(1 - n(s)) \mathrm{d}s \\ &\geq \int_0^r -s\lambda\varepsilon \mathrm{d}s = -\varepsilon\lambda\frac{r^2}{2}. \end{aligned}$$

Dividing through by $r > 0$, we find

$$v(r) \geq -\lambda\frac{r}{2}.$$

Since $r \leq R$, this implies

$$v(r) \geq -\lambda\frac{R}{2}.$$

Thus, the velocity field v is bounded below by $\frac{-\lambda R}{2}$. □

The lemma above, together with Assumptions (A2) and (A3), establishes the existence of a point r_b such that $c(r_b) = c_b$, where $r_b < R$. Additionally, since $c_d \geq c_b$ is assumed, it establishes also the existence of $r_d < R$ such that $c(r_d) = c_d$. Indeed, we find that c_* in Lemma 5.5 is c_b. In particular, for $c < c_b$ we have $k_b(c) - k_d(c) = -1 \leq 0$ and for $c > c_b$ we obtain $k_b(c) - k_d(c) = \sigma H(c - c_d) \geq 0$. Since $c(R) = 1 > c_d \geq c_b$, Lemma 5.4 then establishes the existence of r_d. We proceed with investigating some properties of the density of living tissue cells n.

Lemma 5.6. *The density of living tissue cells n at the boundary is given as*

$$n(R) = \frac{\sigma + \varepsilon\lambda}{1 + \varepsilon\lambda}. \tag{5.26}$$

Proof. Using equation (5.18a) together with (5.20), we obtain

$$n(r)(k_b(c(r))n(r) - \varepsilon\lambda(1 - n(r))) = (k_b(c(r)) - k_d(c(r)))n(r) - \varepsilon(vn')(r),$$

which then yields

$$\varepsilon(vn')(r) = k_b(c(r))n(r)(1 - n(r)) + \varepsilon\lambda n(r)(1 - n(r)) - k_d(c(r))n(r). \tag{5.27}$$

Since $v(R) = 0$ and $c(R) = 1$, substituting $r = R$ into equation (5.27) gives

$$0 = k_b(1)n(R)(1 - n(R)) + \varepsilon\lambda n(R)(1 - n(R)) - k_d(1)n(R),$$

Factoring out $n(R)$, we obtain

$$n(R)\left(k_b(1)(1-n(R))+\varepsilon\lambda(1-n(R))-k_d(1)\right)=0.$$

This implies either $n(R)=0$, which is a contradiction to the assumption $n(R)>0$, or

$$k_b(1)(1-n(R))+\varepsilon\lambda(1-n(R))-k_d(1)=0,$$

which then simplifies to

$$n(R)=\frac{\sigma+\varepsilon\lambda}{1+\varepsilon\lambda}.$$

This proves (5.26). □

In a next step we use Lemma 5.4 to derive further properties for the density of living tissue cells n.

Lemma 5.7. *Let Assumptions (A1), (A2), and (A4) hold. Then,*

$$\int_{r_b}^{R}\frac{\rho}{R}(R-\rho)n(\rho)\mathrm{d}\rho\leq C\varepsilon^2.$$

Proof. The explicit representation (5.23) for c implies at $r=0$ that

$$c(0)=1-\frac{1}{\varepsilon^2}\int_0^R\rho K(c(\rho))n(\rho)\int_\rho^R\frac{1}{sD(n(s))}\mathrm{d}s\mathrm{d}\rho.$$

Since $c(0)\geq 0$ by Lemma 5.4, this implies

$$\begin{aligned}1&\geq\frac{1}{\varepsilon^2}\int_0^R\rho\beta H(c(\rho)-c_b)n(\rho)\int_\rho^R\frac{1}{sD(n(s))}\mathrm{d}s\mathrm{d}\rho\\&\geq C\frac{1}{\varepsilon^2}\int_{r_b}^R\rho n(\rho)\int_\rho^R\frac{1}{s}\mathrm{d}s\mathrm{d}\rho\\&\geq C\frac{1}{\varepsilon^2}\int_{r_b}^R\frac{\rho}{R}(R-\rho)n(\rho)\mathrm{d}\rho.\end{aligned}$$

Thus we conclude

$$\int_{r_b}^{R}\frac{\rho}{R}(R-\rho)n(\rho)\mathrm{d}\rho\leq C\varepsilon^2.$$

□

Lemma 5.8. *There holds*

$$0 \leq \int_0^R k_b(c(r))n(r)r\mathrm{d}r = \int_0^R k_d(c(r))n(r)r\mathrm{d}r \leq \varepsilon\lambda\frac{R^2}{2}.$$

Proof. Since we assume that $n \geq 0$ holds, we derive from (5.20) by integration over $(0, R)$

$$0 = \int_0^R r(k_b(c(r))n(r) - \varepsilon\lambda(1 - n(r)))\mathrm{d}r \geq \int_0^R k_b(c(r))n(r)r\mathrm{d}r - \varepsilon\lambda\frac{R^2}{2}.$$

This allows use to deduce the upper bound

$$\int_0^R k_b(c(r))n(r)r\mathrm{d}r \leq \varepsilon\lambda\frac{R^2}{2}.$$

On the other hand, since $n \leq 1$ holds by our assumption, we obtain from (5.20)

$$0 = \int_0^R r(k_b(c(r))n(r) - \varepsilon\lambda(1 - n(r)))\mathrm{d}r \leq \int_0^R k_b(c(r))n(r)r\mathrm{d}r.$$

Integration of (5.18a) over $(0, R)$ gives together with the boundary condition (5.19a)

$$0 = \int_0^R (k_b - k_d)(c(r))n(r)r\mathrm{d}r.$$

This implies the same inequalities for k_d. □

After establishing several results for the density of living tumor cells n, we now focus on analyzing the critical point r_b, where the nutrient concentration c satisfies $c(r_b) = c_b$. In a next step, we show that the distance between r_b and R is of order $O(\varepsilon)$.

Lemma 5.9. *Let Assumptions (A1)–(A4) apply. Then* $0 \leq R - r_b \leq C\varepsilon$ *with a positive constant* C *independent of* ε.

Proof. As shown in Lemma 5.8, we have

$$\int_0^R k_d(c(r))rn(r)\mathrm{d}r = \int_0^R k_b(c(r))rn(r)\mathrm{d}r.$$

Using Assumption (A2), we obtain

$$\int_0^R k_d(c(r))rn(r)\mathrm{d}r = \int_{r_b}^R rn(r)\mathrm{d}r.$$

This implies, together with the assumption $n \leq 1$ that

$$\int_0^R k_d(c(r))rn(r)\mathrm{d}r \leq R(R-r_b).$$

Using Lemma 5.8 we deduce

$$0 \leq R(R-r_b).$$

Owing to the assumption that $R_{\min} \leq R \leq R_{\max}$, we conclude $0 \leq R - r_b$.

To derive the second bound, we use the explicit representation of c given in (5.23) togehter with the Assumptions (A1) and (A2) to estimate

$$\begin{aligned}
c_b =& 1 - \frac{1}{\varepsilon^2}\int_0^R \rho K(c(\rho))n(\rho)\int_{\max(r_b,\rho)}^R \frac{1}{sD(n(s))}\mathrm{d}s\mathrm{d}\rho \\
\leq& 1 - \frac{1}{\varepsilon^2}\int_0^R \rho K(c(\rho))n(\rho)\frac{R-\max(r_b,\rho)}{RD_{\max}}\mathrm{d}\rho \\
\leq& 1 - \frac{c_0}{\varepsilon^2}(R-r_b)K(c_b)\int_{r_b}^R \rho n(\rho)\mathrm{d}\rho \\
\leq& 1 - \frac{C}{\varepsilon}(R-r_b)K(c_b),
\end{aligned}$$

where the last estimate follows by Lemma 5.8. This shows the second bound of the lemma. □

In the next step we give a representation for the pressure p.

Lemma 5.10. *Let Assumptions (A1)–(A4) apply. The pressure p is given as*

$$p(r) = \frac{\gamma(n(R))}{R} + \frac{1}{\varepsilon^2}\int_r^R \frac{\mu(n(s),\varepsilon)}{s}\int_0^s \rho(k_b(c)n - \varepsilon\lambda(1-n))(\rho)\mathrm{d}\rho\mathrm{d}s.$$

Furthermore, p is monotone increasing.

Proof. Using (5.18e) and (5.24), we obtain

$$-\varepsilon^2 p'(r) = \frac{\mu(n,\varepsilon)}{r}\int_0^r \rho(k_b(c)n - \varepsilon\lambda(1-n))(\rho)\mathrm{d}\rho.$$

Next, integrating this expression for p' over (r, R) and using the boundary condition (5.19a), we derive

$$\begin{aligned} p(r) &= \frac{\gamma(n(R))}{R} + \frac{1}{\varepsilon^2}\int_r^R \frac{\mu(n(s),\varepsilon)}{s}\int_0^s \rho(k_b(c)n - \varepsilon\lambda(1-n))(\rho)\mathrm{d}\rho\mathrm{d}s \\ &= \frac{\gamma(n(R))}{R} + \frac{1}{\varepsilon^2}\int_0^R \rho(k_b(c)n - \varepsilon\lambda(1-n))(\rho)\int_{\max\{\rho,r\}}^R \frac{\mu(n(s),\varepsilon)}{s}\mathrm{d}s\mathrm{d}\rho, \end{aligned}$$

and conclude

$$p(0) = \frac{\gamma(n(R))}{R} + \frac{1}{\varepsilon^2}\int_0^R \rho(k_b(c)n - \varepsilon\lambda(1-n))(\rho)\int_\rho^R \frac{\mu(n(s),\varepsilon)}{s}\mathrm{d}s\mathrm{d}\rho.$$

Since $p' = \frac{-\mu(n,\varepsilon)}{\varepsilon}v \geq 0$ holds by Lemma 5.5, p is monotone increasing and therefore bounded from above by $p(R)$ which is given by the boundary condition.

□

We are now in a position to establish some convergence results. Recall that in the above Lemmas we omitted the index ε of R, n, v, and p. Let n_ε, v_ε and p_ε denote the components of the solution. In what follows we assume that $R = R_\varepsilon$ converges to some R_*. We begin with first convergence results for the density of the living tumor cells.

Lemma 5.11. *Let Assumptions (A1)–(A4) apply. There exists a subsequence of the sequence of solutions $(n_\varepsilon)_\varepsilon$, denoted by $(n_\varepsilon)_\varepsilon$ again, such that*

$$\int_0^{R_\varepsilon} \frac{s}{\varepsilon} n_\varepsilon(s)\eta(s)\mathrm{d}s \to \vartheta(\eta) = \alpha\eta(R_*) \quad \forall \eta \in C^0(0, R_{\max})$$

holds for $\varepsilon \to 0$ with $\alpha = \lim_{\varepsilon\to 0}\int_0^{R_\varepsilon}\frac{s}{\varepsilon}n_\varepsilon(s)\mathrm{d}s$.

Proof. We have by (5.18a) and the assumption $c_d \geq c_b$

$$\begin{aligned} -\int_0^{r_b}\frac{r n_\varepsilon(r)}{\varepsilon}\eta(r)\mathrm{d}r &= \int_0^{r_b}(r v_\varepsilon n_\varepsilon)'(r)\eta(r)\mathrm{d}r \\ &= -\int_0^{r_b}(r v_\varepsilon n_\varepsilon)(r)\eta'(r)\mathrm{d}r + r_b v_\varepsilon(r_b)n_\varepsilon(r_b)\eta(r_b). \end{aligned}$$

Since v_ε is nonpositive and uniformly bounded from below by Lemma 5.5, it follows

$$\int_0^{r_b} (rv_\varepsilon n_\varepsilon)(r)\eta'(r)\mathrm{d}r \leq -\max|\eta'| \int_0^{r_b} (rv_\varepsilon n_\varepsilon)(r)\mathrm{d}r$$

and

$$\int_0^{r_b} (rv_\varepsilon n_\varepsilon)(r)\eta'(r)\mathrm{d}r \geq \max|\eta'| \int_0^{r_b} (rv_\varepsilon n_\varepsilon)(r)\mathrm{d}r.$$

Using Lemma 5.5, we estimate

$$\int_0^{r_b} (rv_\varepsilon n_\varepsilon)(r)\eta'(r)\mathrm{d}r \leq \max|\eta'|\frac{\lambda {R_\varepsilon}^2}{2} \int_0^{r_b} rn_\varepsilon(r)\mathrm{d}r,$$
$$\int_0^{r_b} (rv_\varepsilon n_\varepsilon)(r)\eta'(r)\mathrm{d}r \geq -\max|\eta'|\frac{\lambda {R_\varepsilon}^2}{2} \int_0^{r_b} rn_\varepsilon(r)\mathrm{d}r.$$

Hence Lemma 5.8 implies

$$-C\varepsilon \leq \int_0^{r_b} (rv_\varepsilon n_\varepsilon)(r)\eta'(r)\mathrm{d}r \leq C\varepsilon.$$

Since $r_b \to R_*$ by Lemma 5.9, we have

$$\int_0^{R_\varepsilon} \frac{rn_\varepsilon(r)}{\varepsilon}\eta(r)\mathrm{d}r \to \alpha\eta(R_*).$$

This completes the proof of the lemma. □

In addition to this convergence of the weighted density of living tumor cells, we can also establish a convergence result for a different weighted density incorporating the cellular birth rate k_b.

Lemma 5.12. *Let Assumptions (A1)–(A4) apply. For the sequence $(n_\varepsilon)_\varepsilon$ there exists a subsequence, also denoted by $(n_\varepsilon)_\varepsilon$, such that*

$$\int_0^{R_\varepsilon} \frac{s}{\varepsilon}k_b(c_\varepsilon(s))n_\varepsilon(s)\eta(s)\mathrm{d}s \to \tilde{\alpha}\eta(R_*) \quad \forall \eta \in C^0([0, R_{\max}+1]),$$

holds for $\varepsilon \to 0$ with $\tilde{\alpha} = \lim_{\varepsilon\to 0} \int_0^{R_\varepsilon} \frac{s}{\varepsilon}n_\varepsilon(s)k_b(c_\varepsilon(s))\mathrm{d}s$.

Proof. In Lemma 5.8 we have already shown that $\frac{1}{\varepsilon}\int_0^{R_\varepsilon} sk_b(c_\varepsilon(s)n_\varepsilon(s)\mathrm{d}s$ is uniformly bounded. Hence, $\int_0^{R_\varepsilon} \frac{s}{\varepsilon}k_b(c_\varepsilon(s))n_\varepsilon(s)\eta(s)\mathrm{d}s$ is also uniformly bounded. Now let η

be an arbitrary function in $C_c^0([0, R_*))$. Since $r_{b,\varepsilon} \to R_\varepsilon$ by Lemma 5.9 and therefore $r_{b,\varepsilon} \to R_*$, there exists an $\varepsilon_0 > 0$ such that for $\varepsilon < \varepsilon_0$ we have $\eta = 0$ in $(r_{b,\varepsilon}, R_\varepsilon)$. Then we conclude

$$\int_0^{R_\varepsilon} \frac{s}{\varepsilon} k_b(c_\varepsilon(s)) n_\varepsilon(s) \eta(s) \mathrm{d}s \to 0.$$

Now let η be an arbitrary function in $C_c^0((R_*, \infty))$. Then we have

$$\int_0^{R_\varepsilon} \frac{s}{\varepsilon} k_b(c_\varepsilon(s)) n_\varepsilon(s) \eta(s) \mathrm{d}s = 0.$$

This gives the concentration at R_*. □

We now establish convergence for the velocity v_ε.

Lemma 5.13. *Let Assumptions (A1)–(A4) hold and set $v_\varepsilon \equiv 0$ in $(R_\varepsilon, R_{\max} + 1)$. For the sequence of velocity solutions $(v_\varepsilon)_\varepsilon$ there exists subsequence, denoted by $(v_\varepsilon)_\varepsilon$ again, such that for $\varepsilon \to 0$*

$$v(r) \to -\lambda \frac{r}{2}$$

in $L^q(0, R_*)$ for $q < \infty$.

Proof. By (5.20) we have

$$rv(r) = \int_0^r s k_b(c(s)) \frac{n(s)}{\varepsilon} - s\lambda(1 - n(s)) \mathrm{d}s$$

and thus

$$\int_0^{R_\varepsilon} |(rv_\varepsilon(r))'| \mathrm{d}r \leq C < \infty.$$

Hence the mapping $r \mapsto rv_\varepsilon(r)$ is uniformly bounded in $W^{1,1}(0, R_{\max} + 1)$ and therefore $rv_\varepsilon(r) \to \tilde{v}(r) \in BV(0, R_{\max} + 1)$ in $L^q(0, R_{\max} + 1)$, where $q < \infty$ and $BV(0, R_{\max} + 1)$ is the space of functions of bounded variation on $(0, R_{\max} + 1)$.

Using (5.24) together with Lemma 5.12, we obtain

$$\tilde{v}(r) = -\lambda \frac{r^2}{2}$$

for $r < R$. Hence $v(r) \to -\lambda r/2$. □

The lemma above allows us to compute $\tilde{\alpha}$ in Lemma 5.12. In particular, Lemma 5.11, together with the boundary condition $v_\varepsilon(R_\varepsilon) = 0$ and (5.24) imply $\tilde{\alpha} = \lambda^{R^2}/2$.

We conclude the proof of Theorem 5.3 by proving weak-star convergence of p_ε in the following lemma.

Lemma 5.14. *Let Assumptions (A1)–(A5) apply. Let $p \in C^\infty(0, R_*)$ be a solution of*

$$\frac{1}{r}(rp'(r))' = \lambda\mu_1$$

satisfying the boundary conditions

$$p'(0) = 0, \quad p(R_*) = \beta + \gamma_0 R_*^{-1}$$

with a constant

$$\beta = \lim_{\varepsilon\to 0} \int_r^{R_\varepsilon} \frac{\mu_0 n_\varepsilon(s)}{\varepsilon} v_\varepsilon(s)\mathrm{d}s < \infty.$$

Then there exists a subsequence of $(p_\varepsilon)_\varepsilon$, also denoted by $(p_\varepsilon)_\varepsilon$, such that for $\varepsilon \to 0$

$$p_\varepsilon \overset{*}{\rightharpoonup} p$$

in $L^\infty(0, R_{\max})$.

Proof. We have

$$\begin{aligned} p_\varepsilon(r) &= \int_r^{R_\varepsilon} \frac{\mu(n_\varepsilon(s), \varepsilon)}{\varepsilon} v_\varepsilon(s)\mathrm{d}s + \frac{\gamma(n_\varepsilon(R_\varepsilon))}{R_\varepsilon} \\ &= \int_r^{R_\varepsilon} \mu_1 v_\varepsilon(s)\mathrm{d}s + \int_r^{R_\varepsilon} \frac{\mu_0 n_\varepsilon(s)}{\varepsilon} v_\varepsilon(s)\mathrm{d}s + \frac{\gamma(n_\varepsilon(R))}{R_\varepsilon} \\ &\to \int_r^{R_*} \mu_1 v(s)\mathrm{d}s + \lim_{\varepsilon\to 0} \int_r^{R_\varepsilon} \frac{\mu_0 n_\varepsilon(s)}{\varepsilon} v_\varepsilon(s)\mathrm{d}s + \frac{\gamma_0}{R_*}. \end{aligned}$$

The convergence of the first integral follows from Lemma 5.13, while the convergence of $\gamma(n_\varepsilon(R_\varepsilon))$ to $\gamma_0 = \gamma(\sigma)$ follows directly since $n_\varepsilon(R_\varepsilon) \to \sigma$ by Lemma 5.6. Additionally, the convergence of

$$\int_r^{R_\varepsilon} \frac{\mu_0 n_\varepsilon(s)}{\varepsilon} v_\varepsilon(s)\mathrm{d}s$$

for $\epsilon \to 0$ follows, since the integral is uniformly bounded. This limit, denoted by β, is independent of r by the same arguments as in Lemma 5.11.

Furthermore, (5.18e) implies

$$p_\varepsilon'(r) = \frac{-\mu_0 n_\varepsilon(r)}{\varepsilon} v_\varepsilon(r) - \mu_1 v_\varepsilon(r)$$

and hence Lemma 5.13 implies

$$p_\varepsilon(r) \to \mu_1 \lambda \frac{r^2}{4} + p(0) = p(r).$$

This implies the convergence of p_ε to a solution of

$$\frac{1}{r}(rp'(r))' = \lambda\mu_1$$

with the boundary conditions $p'(0) = 0$ and $p(R_*) = \beta + \gamma_0 R_*^{-1}$. □

The weak-star convergence shown in Lemma 5.14 together with a translation by β establishes the convergence claimed in Theorem 5.3.

In addition to this convergence result, we can calculate the radius of the limit problem from given model data. For given parameters Q and λ we obtain

$$R_* = \frac{2Q}{\lambda}.$$

Since Q is defined as the limit of the boundary value for v_ϵ, this equation implies the convergence of R_ε to R_* for at least a subsequence under the assumption that R_ε is uniformly bounded. To prove the first statement, $R_* = {}^{2Q}/_{\lambda}$, we use the first derivative of P

$$P'(r) = \frac{1}{r} R\mu_1 \left(Q - \frac{\lambda R_*}{2}\right) + \frac{\lambda\mu_1}{2} r.$$

Since the solution is radially symmetric, $P'(0) = 0$ and therefore

$$R_*\mu_1 \left(Q - \frac{\lambda R_*}{2}\right) = 0.$$

This condition can hold only if

$$R_* = \frac{2Q}{\lambda}.$$

Hence, the equation for the radius holds.

5.3 Finite element discretization

In this section, we introduce a generalization of the thin-rim limit problem (5.17). The generalization is achieved by introducing a parameter $\gamma \in \mathbb{R}$, which allows us to remove the mean curvature term from the Robin boundary condition while retaining it in the interface evolution. The resulting generalized model is given by

$$\Delta u = 1 \qquad \text{in } \Omega(t), \tag{5.28a}$$

$$\nabla u \cdot \mathbf{n} + \frac{u}{\alpha} + \beta\kappa = Q \qquad \text{on } \Gamma(t), \tag{5.28b}$$

$$V = \frac{u}{\alpha} + (\beta + \gamma)\kappa \qquad \text{on } \Gamma(t). \tag{5.28c}$$

As discussed in Section 2.3, computing the curvature from a level set representation can be challenging. Several approaches have been proposed in the literature; see, e.g, [Hys06; Hys07; GR11; TK12; RE14]. These methods rely either on recovery strategies for the gradient (cf. [ZZ92a; ZZ92b]) or on the evaluation of Laplace–Beltrami derivatives. To avoid the direct computation of the mean curvature, we restrict ourselves to the case $\beta = 0$. Nevertheless, we retain β in the following construction of the numerical scheme.

Before we discretize the system, we first introduce the geometric setting. We assume that there exists a fixed computational domain $U \subset \mathbb{R}^d$ such that the evolving domain $\Omega(t)$ remains compactly contained in U and that $\Gamma(t) \cap \partial U = \emptyset$.

Let $\varphi : U \to \mathbb{R}$ denote a level set function representing the interface $\Gamma(t)$, with

$$\varphi(\mathbf{x}) < 0 \text{ for } \mathbf{x} \in \Omega(t), \quad \varphi(\mathbf{x}) = 0 \text{ for } \mathbf{x} \in \Gamma(t), \quad \varphi(\mathbf{x}) > 0 \text{ elsewhere.}$$

The kinematic condition for the tumor boundary yields the level set evolution equation

$$\partial_t \varphi + V\mathbf{n} \cdot \nabla\varphi = 0.$$

Substituting the velocity law (5.28c) and noting that $\mathbf{n} = \frac{\nabla\varphi}{|\nabla\varphi|}$, we obtain

$$\partial_t \varphi + \left((\beta + \gamma)\kappa + \frac{1}{\alpha}u\right)|\nabla\varphi| = 0. \tag{5.29}$$

Since $\kappa = -\nabla \cdot \frac{\nabla\varphi}{|\nabla\varphi|}$, the evolution of φ is governed by

$$\partial_t \varphi - (\beta + \gamma)|\nabla\varphi|\nabla \cdot \left(\frac{\nabla\varphi}{|\nabla\varphi|}\right) = \frac{-|\nabla\varphi|}{\alpha}u.$$

To extend the evolution into the whole domain, we have to define a proper extension of u. We define $\widetilde{\mathcal{E}_{\text{cp}}}$ as the closest-point extension operator, mapping a scalar quantity q defined on U to its value at the closest point $\mathbf{x}_\Gamma$ on the interface, $\widetilde{\mathcal{E}_{\text{cp}}} q(\mathbf{x}) = q(\mathbf{x}_\Gamma)$. Using this extension, we derive

$$\partial_t \varphi - (\beta + \gamma)|\nabla\varphi|\nabla \cdot \left(\frac{\nabla\varphi}{|\nabla\varphi|}\right) = \frac{-|\nabla\varphi|}{\alpha}\widetilde{\mathcal{E}_{\text{cp}}} u.$$

We impose homogeneous Neumann boundary conditions on ∂U when U is sufficiently large. Hence,

$$\begin{aligned}
\Delta u &= 1 && \text{in } \Omega(t),\\
\nabla u \cdot \mathbf{n} + \frac{u}{\alpha} + \beta\kappa &= Q && \text{on } \Gamma(t),\\
\partial_t \varphi - (\beta + \gamma)|\nabla\varphi|\nabla \cdot \left(\frac{\nabla\varphi}{|\nabla\varphi|}\right) &= \frac{-|\nabla\varphi|}{\alpha}\widetilde{\mathcal{E}_{\text{cp}}} u && \text{in } U,\\
\nabla\varphi \cdot \mathbf{n} &= 0 && \text{on } \partial U.
\end{aligned}$$

Multiplying with sufficiently smooth functions $\phi \in H^1(U)$ and $\psi \in H^1(\Omega(t))$ and integrating, we obtain

$$\int_{\Omega(t)} \nabla u \cdot \nabla\psi \mathrm{d}\mathbf{x} + \int_{\Gamma(t)} \frac{1}{\alpha} u\psi \mathrm{d}s = \int_{\Omega(t)} -\psi \mathrm{d}\mathbf{x} + \int_{\Gamma(t)} (Q - \beta\kappa)\psi \mathrm{d}s, \tag{5.30a}$$

$$\int_U \frac{\partial_t \varphi}{|\nabla\varphi|}\phi + (\beta + \gamma)\frac{\nabla\varphi \cdot \nabla\phi}{|\nabla\varphi|}\mathrm{d}\mathbf{x} = \int_U \frac{\widetilde{\mathcal{E}_{\text{cp}}} u}{\alpha}\phi \mathrm{d}\mathbf{x}. \tag{5.30b}$$

To begin with the discretization, consider a conforming triangulation $\mathcal{T}_h$ of U. For simplicity, we assume that $\mathcal{T}_h$ is fitted to U, i.e., $\bigcup_{K\in\mathcal{T}_h} K = \overline{U}$. We define the time-dependent subtriangulation

$$\mathcal{T}_h(\Omega(t)) = \{K \in \mathcal{T}_h : K \cap \Omega(t) \neq \emptyset\},$$

consisting of all simplices intersecting $\Omega(t)$, and time-dependent domain

$$\Omega_h(t) = \operatorname{int}\Big(\bigcup_{K\in\mathcal{T}_h(\Omega(t))} K\Big).$$

Let V_h denote the finite element space of continuous piecewise affine functions defined on the triangulation $\mathcal{T}_h$. This finite element space is defined by

$$V_h = \{v_h \in C(\overline{U}) : v_h|_K \in P_1(K)\ \forall\, K \in \mathcal{T}_h\}.$$

Denote by $V_h'(t)$ finite element space of continuous piecewise affine functions defined on the sub-triangulation $\mathcal{T}_h(\Omega(t))$. The semi-discrete form of (5.30) then reads as: For $t > 0$ find $(u_h(\cdot,t), \varphi_h(\cdot,t)) \in V_h'(t) \times V_h$ such that

$$\begin{aligned}\int_{\Omega(t)} \nabla u_h \cdot \nabla \psi_h \mathrm{d}\mathbf{x} + \int_{\Gamma(t)} \frac{1}{\alpha} u_h \psi_h \mathrm{d}s \\ = \int_{\Omega(t)} -\psi_h \mathrm{d}\mathbf{x} + \int_{\Gamma(t)} (Q - \beta\kappa_h)\psi_h \mathrm{d}s \quad \forall \psi_h \in V_h'(t),\end{aligned} \tag{5.31a}$$

$$\int_U \frac{\partial_t \varphi_h}{|\nabla \varphi_h|}\phi_h + (\beta+\gamma)\frac{\nabla\varphi_h \cdot \nabla\phi_h}{|\nabla\varphi_h|}\mathrm{d}\mathbf{x} = \int_U \frac{\widetilde{\mathcal{E}_{\mathrm{cp}} u_h}}{\alpha}\phi_h \mathrm{d}\mathbf{x} \quad \forall \phi_h \in V_h. \tag{5.31b}$$

We now discretize in time using time steps $0 = t_0 < t_1 < t_2 < \ldots$ and a semi-implicit approach (cf. [DD00; Bän+23]). The discrete problem reads as: For $n \in \mathbb{N}$, find $(u_h^n, \phi_h^n) \in V_h'(t_n) \times V_h$ such that

$$\begin{aligned}\int_{\Omega(t_n)} \nabla u_h^n \cdot \nabla \psi_h \mathrm{d}\mathbf{x} + \int_{\Gamma(t_n)} \frac{1}{\alpha} u_h^n \psi_h \mathrm{d}s \\ = \int_{\Omega(t_n)} -\psi_h \mathrm{d}\mathbf{x} + \int_{\Gamma(t_n)} (Q - \beta\kappa_h^n)\psi_h \mathrm{d}s \quad \forall \psi_h \in V_h'(t_n),\end{aligned} \tag{5.32a}$$

$$\begin{aligned}\int_U \frac{\varphi_h^n - \varphi_h^{n-1}}{(t^n - t^{n-1})|\nabla\varphi_h^{n-1}|}\phi_h + (\beta+\gamma)\frac{\nabla\varphi_h^n \cdot \nabla\phi_h}{|\nabla\varphi_h^{n-1}|}\mathrm{d}\mathbf{x} \\ = \int_U \frac{\widetilde{\mathcal{E}_{\mathrm{cp}} u_h^{n-1}}}{\alpha}\phi_h \mathrm{d}\mathbf{x} \quad \forall \phi_h \in V_h,\end{aligned} \tag{5.32b}$$

where u_h^0 is the solution of (5.32a) for $t_0 = 0$ and φ_h^0 is an approximation in V_h to the level set function corresponding to $\Gamma(0)$.

In (5.32a) we integrate over $\Omega(t_n)$, $n \geq 0$. It might be possible that $\Omega(t_n)$ intersects some simplex $K \in \mathcal{T}_h(\Omega(t_n))$ only minimally. As already discussed in the previous chapters (cf. Sections 3.2 and 4.2), this integration over small cut cells can lead to instabilities. To avoid these, we adopt the PG stabilization technique introduced for Dirichlet boundary value problems (BVPs) in Chapter 3 and for elliptic interface problems in Chapter 4. Therefore we add the stabilization term defined in (3.10) in Chapter 3 with $\Omega_{+,h} = \Omega_h(t_n)$ to the left hand side in (5.32a). Using this stabilization, we obtain for $n \geq 0$

$$\begin{aligned}\int_{\Omega(t_n)} \nabla u_h^n \cdot \nabla \psi_h \mathrm{d}\mathbf{x} + \int_{\Gamma(t_n)} \frac{1}{\alpha} u_h^n \psi_h \mathrm{d}s + \int_{\Omega_h(t_n)} (\nabla u_h^n - \mathcal{P}_h \nabla u_h^n) \cdot \nabla \psi_h \mathrm{d}\mathbf{x} \\ = \int_{\Omega(t_n)} -\psi_h \mathrm{d}\mathbf{x} + \int_{\Gamma(t_n)} (Q - \beta\kappa_h^n)\psi_h \mathrm{d}s \quad \forall \psi_h \in V_h'(t_n),\end{aligned} \tag{5.33}$$

where $\mathcal{P}_h$ is defined as in (3.9) in Chapter 3.

To complete the construction of the numerical scheme, we give some more details on the computations of the mean curvature κ_h and the extension $\widetilde{\mathcal{E}_{\text{cp}}}u_h$. To compute the initial mean curvature κ_h^0 of $\Gamma(0)$, we employ an L^2 projection approach (see [Hys07]). Let $\{\Psi_j\}_{j=1,\dots,N_h}$ denote the nodal basis of V_h. Assuming that $\phi(\mathbf{x},0)$ is an SDF, the coefficients κ_i^0 of $\kappa_h^0 = \sum_{i=1}^{N_h} \kappa_i^0 \Psi_i$ satisfy

$$\kappa_i^0 = \frac{\int_U \nabla \cdot \left(\sum_{j=0}^{N_h} \mathbf{n}_j^0 \Psi_j\right) \Psi_i \mathrm{d}\mathbf{x}}{\int_U \Psi_i \mathrm{d}\mathbf{x}}, \qquad \mathbf{n}_j^0 = \frac{\int_U \nabla\varphi(\cdot,0)\Psi_j \mathrm{d}\mathbf{x}}{\int_U \Psi_j \mathrm{d}\mathbf{x}}. \tag{5.34}$$

At each time step, we can either compute κ_h directly or update it using a discrete version of the weak form of (5.29) reading as

$$\int_U \frac{\varphi_h^{n+1} - \varphi_h^n}{(t^{n+1}-t^n)|\nabla\varphi_h^n|}\phi_h + (\beta+\gamma)\kappa_h^{n+1}\phi_h \mathrm{d}\mathbf{x} = \int_U \frac{\widetilde{\mathcal{E}_{\text{cp}}}u_h^n}{\alpha}\phi_h \mathrm{d}\mathbf{x}.$$

Using mass lumping, we compute the coefficients

$$\kappa_i^{n+1} = \frac{1}{\int_U (\beta+\gamma)\Psi_i \mathrm{d}\mathbf{x}} \left(\int_U \frac{\widetilde{\mathcal{E}_{\text{cp}}}u_h^n}{\alpha}\Psi_i \mathrm{d}\mathbf{x} - \int_U \frac{\varphi_h^{n+1} - \varphi_h^n}{(t^{n+1}-t^n)|\nabla\varphi_h^n|}\Psi_i \right). \tag{5.35}$$

The strategy used in Section 3.4 is not suitable for computing the extension $\widetilde{\mathcal{E}_{\text{cp}}}u_h$, since the closest point search is efficient only within a narrow band. Instead, we employ a continuous Galerkin counterpart of the method proposed in [UK18]. The extension problems then reads as: Find $u_h^* \in V_h$ such that

$$-\int_U (\nabla\varphi \otimes \nabla\varphi)\nabla u_h^* \cdot \nabla\phi_h \mathrm{d}\mathbf{x} - \int_{\Gamma(t_n)} \eta(u_h^* - u_h^n)\phi_h \mathrm{d}s = 0 \quad \forall \phi_h \in V_h. \tag{5.36}$$

We then define $\widetilde{\mathcal{E}_{\text{cp}}}u_h^n = u_h^*$.

The complete algorithm operates as follows:

1) Compute the initial mean curvature κ^0 from (5.34).
2) Solve (5.33) for u_h^0 at $t_0 = 0$.
3) Compute the extension of u_h^n using (5.36).
4) Update the level set function φ_h by (5.32b).
5) Update the mean curvature using (5.35).

6) Compute the updated solution u_h^n from (5.33).

7) Repeat Steps 3)–6) for successive time steps.

In the case $\beta = 0$, steps 1) and 5) are skipped.

5.4 Numerical results

In this section, we present the results of numerical studies we performed to assess the performance of the finite element approximation introduced in the previous section. The study considers a qualitative comparison of the results with those obtained in [EKS19] as well as a grid convergence study.

We used a custom `C++` implementation based on the open-source finite element library MFEM [DK10b; And+21; And+24] for all simulations. The solutions were visualized the numerical solutions with ParaView [AGL05; Aya15].

5.4.1 Qualitative comparison

We performed simulations using similar configurations as used in [EKS19]. A uniform grid with $h = 1/256$ and a time step size $\Delta t = 1\text{e}^{-3}$ was employed. In both examples, we set $Q = 1.0$ and use an initial elliptic geometry with height 1.0 and length 0.5.

The results obtained for $(\alpha, \beta, \gamma) = (0.1, 0, 0.1)$ and $(\alpha, \beta, \gamma) = (1.0, 0, 0.1)$ are shown in Figs. 5.1 and 5.2, respectively. In both cases, we observe close agreement with the results in [EKS19]. The minimal and maximal values for the tissue pressure u_h produced by our method lie in comparable ranges to the values obtained with the parametric and diffuse-interface approaches presented in [EKS19]. Moreover, the evolution of the domain exhibits closely related qualitative features. For all three methods, the diameter and the fingering effects exhibit comparable parameter-dependent behavior. These observations indicate that the unfitted FEM with PG stabilization introduced here yields results that are consistent with those produced by both the diffuse-interface method and the parametric finite element scheme proposed in [EKS19].

5.4.2 Grid-convergence study

In addition to the qualitative comparison, we studied the grid convergence of the proposed method. We chose $(\alpha, \beta, \gamma) = (0.1, 0, 0.1)$, $Q = 1.0$, and the same initial

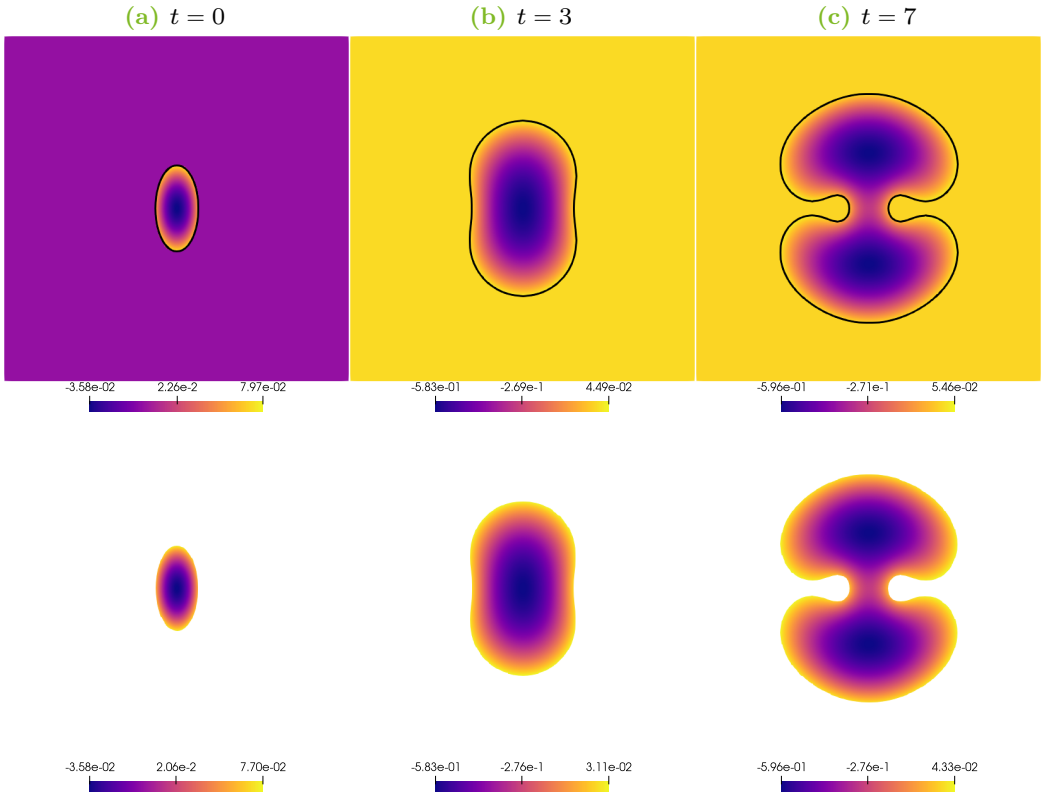

Figure 5.1: Numerical solutions to the thin-rim limit model obtained with $\alpha = 0.1$ and $\gamma = 0.1$. Top row: Tissue pressure and zero level set (black line) with $u_h = 0$ in $U \backslash \Omega(t_n)$. Bottom row: Tissue pressure in $\Omega(t_n)$.

geometry as in the previous subsection. Simulations were carried out on successively refined uniform grids with $\Delta t \approx h^2/10$ up to the time $T = 0.1024$.

The L^2 error between two solutions for the tissue pressure at refinement levels h and $2h$ is defined as

$$\mathrm{err}(u_h(T)) = \left(\int_{\{\varphi_h(T) \geq 0\}} (u_h(T) - u_{2h}(T))^2 \mathrm{d}\mathbf{x} \right)^{1/2}.$$

Likewise, the L^2 error between two level set functions on subsequent grids is given by

$$\mathrm{err}(\varphi_h(T)) = \left(\int_U (\varphi_h(T) - \varphi_{2h}(T))^2 \mathrm{d}\mathbf{x} \right)^{1/2}.$$

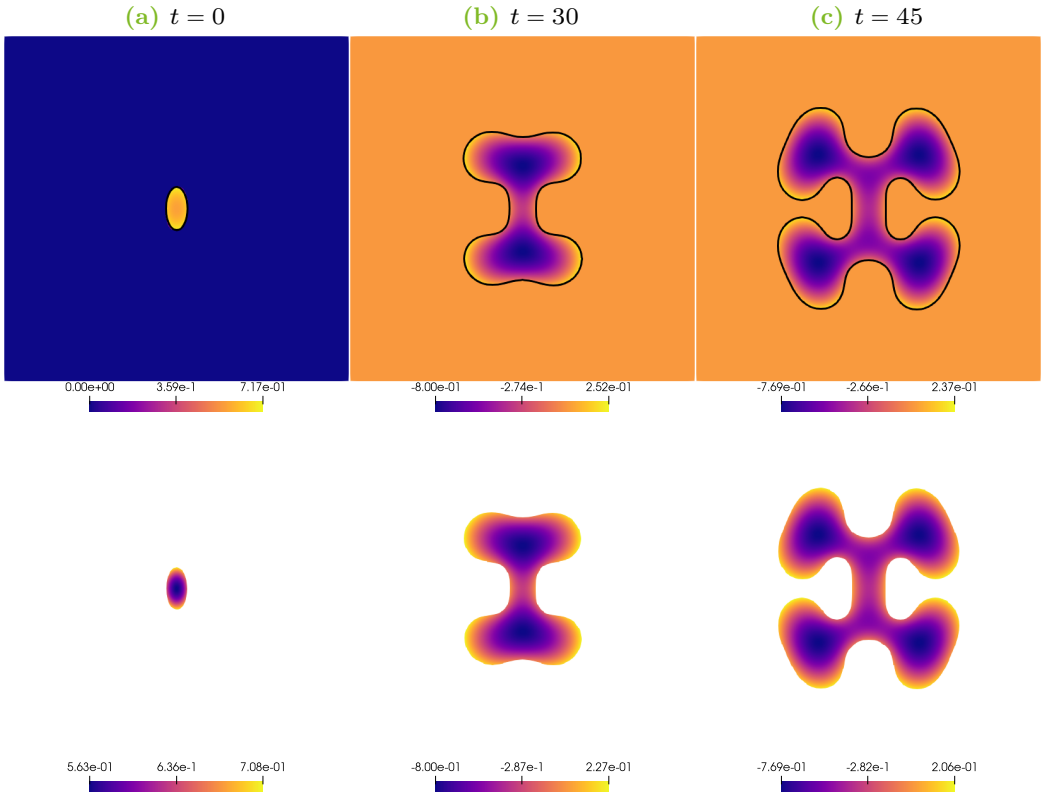

Figure 5.2: Numerical solutions to the thin-rim limit model obtained with $\alpha = 1.0$ and $\gamma = 0.1$. Top row: Tissue pressure and zero level set (black line) with $u_h = 0$ in $U \backslash \Omega(t_n)$. Bottom row: Tissue pressure in $\Omega(t_n)$.

Table 5.3: L^2 convergence history on uniform meshes, $\alpha = 0.1$ and $\gamma = 0.1$.

level	err(φ_h)	EOC	err(u_h)	EOC
1	2.26e-01		1.35e-03	
2	1.28e-01	0.82	3.88e-04	1.70
3	2.68e-02	2.26	9.81e-04	1.98
4	1.37e-02	0.92	2.25e-05	2.12

The L^2 errors and experimental orders of convergence (EOCs) for the tissue pressure u_h and the level set function φ_h are listed in Table 5.3. We observe second order convergence for the tissue pressure and an average convergence order of approximately 1.5 for the level set function. Since the temporal discretization uses a first-order operator splitting, this exceeds the expected first-order convergence.

6 Conclusions

Motivated by tumor growth models, this thesis focused on stabilization techniques for unfitted finite element methods (FEMs). After briefly introducing the model problems and fundamental concepts, we presented and analyzed a stabilization method for unfitted FEMs. The approach modifies the discrete formulation of elliptic boundary value problems (BVPs) and interface problems by adding a bilinear form based on projected gradients. We provided a detailed theoretical analysis of the resulting unfitted FEMs and verified the theoretical results in numerical experiments. Finally, we examined a tumor growth model introduced in [EKS19]. In addition to theoretical considerations, we applied the proposed unfitted FEM to a thin-rim limit model.

In this chapter, we summarize the ideas and results of the thesis. Moreover, we outline several directions for future research within the scope of this work.

6.1 Summary

In Chapter 3, we presented a stabilization technique for unfitted FEMs for elliptic BVPs, relying on gradient projections. After a brief introduction to the unfitted Nitsche method (see [Nit71; BET11; Cho24]) in Section 3.1, we formulated the projected gradient (PG) stabilization for affine finite elements in Section 3.2. The subsequent Section 3.3 presented an in-depth analysis for the unfitted FEMs with PG stabilization. In Lemma 3.1 and Corollary 3.2, we proved that the bilinear form associated with the stabilization term is symmetric and induces a semi-inner product. This property enabled the proof of Theorem 3.6, establishing an $O(h^2)$ error estimate in the L^2 norm for the solution of the discrete problem. Next, Section 3.4 introduced a diffuse-interface approximation to replace surface integrals over sharp embedded boundaries by volumetric approximations. To this end, we used regularized delta functions and a closest-point extension algorithm from [KB22] to compute volumetric integrals based on level set descriptions. The numerical experiments in Section 3.5 illustrate the stabilizing effects of the method. Different extension widths were used to study their influence on the error and to compare diffuse-interface and sharp-interface variants of the method. We also compared the condition number of the system matrix for the unfitted Nitsche method with that

of the proposed unfitted FEM with PG stabilization. The chapter concluded with a comparison to the shifted-boundary method (SBM) (see [MS18a; ACS20; ACS21]) and an extension to higher-order elements in Section 3.6.

Following [OBK25], Chapter 4 adapted the concept of PG stabilization to elliptic interface problems. Using the same structure as in the previous chapter, we started with a brief introduction to unfitted FEMs for interface problems in Section 4.1 (see [HH02]). The stabilization method introduced in [OBK25] was presented in Section 4.2 and analyzed in Section 4.3. Using tools developed in Chapter 3, we proved an $O(h^2)$ a priori error estimate in the L^2 norm for the solution of the discrete problem in Theorem 4.6. Section 4.4 introduced a diffuse-interface formulation that replaces interface integrals by volumetric approximations. The numerical results in Section 4.5 support the theoretical analysis. In particular, we demonstrated numerically that the condition number of the system matrix for the unfitted FEM with PG stabilization is independent of the position of the interface relative to the background mesh. Moreover, in Section 4.6, we applied the method to a convection–diffusion interface problem. To suppress spurious oscillations arising from convection, we introduced a stabilization parameter following [VRK25]. The chapter ended with an extension to higher-order elements in Section 4.7.

The PG stabilization introduced fits naturally into the class of ghost penalty (GP) stabilizations. In contrast to other GP approaches, such as continuous interior penalty (CIP), the proposed method for affine finite elements operates, on the algebraic level, with standard FEM matrices and is therefore straightforward to implement within existing FEM codes. Another important advantage of the PG approach is its natural extension to convection–diffusion interface problems. The PG stabilization term can be shown to stabilize not only against small cut cells, but also to stabilize convective terms (cf. [VRK25]). Moreover, algebraic flux correction techniques can be incorporated straightforwardly, without requiring any modifications of the underlying scheme.

In Chapter 5, we focused on a tumor growth model. Following [EKS19], Section 5.1 introduced a mathematical model for tumor growth and derived a thin-rim limit model using the method of formal asymptotic expansions. In Section 5.2, the case of stationary rotationally symmetric solutions was studied in detail. In this setting, Theorem 5.3 established weak-star convergence of solutions in L^∞. The proof was decomposed into several lemmas and worked out thoroughly. Establishing the weak-star convergence in a specific setting, we took a step toward a mathematical justification of the formal asymptotic expansions presented in [EKS19] and [Eyl19]. Section 5.3 introduced a generalized thin-rim model. We discretized it with an unfitted finite element approach. To mitigate adverse effects caused by small cut cells, we incorporated PG stabilization. The numerical experiments in Section 5.4

confirmed the effectiveness of the method. Using two different parameter sets, we compared our results with those from [EKS19]. For a particular parameter set, we conducted a grid convergence study and observed average experimental orders of convergence (EOCs) of approximately 1.5 for the interface and 2 for the tissue pressure in the L^2 norm. In contrast to the parametric and diffuse-interface method presented in [EKS19], our proposed approach does not rely on an explicit discretization of the tumor, thereby eliminating the need for frequent remeshing during the time integration.

6.2 Outlook

Various topics for future research projects arise from the results presented here. Since the methods presented in Chapters 3 and 4 rely on the same underlying concept and exhibit strong similarities, many of the corresponding research topics are closely related. The numerical results in Sections 3.5 and 4.5 suggest that the condition number of the system matrix is independent of the interface or boundary position within the background mesh. A rigorous theoretical study of this observation remains open. In Sections 3.6 and 4.7, we modified the stabilization technique to achieve higher-order accuracy. The numerical experiments indicate that optimal-order convergence is obtained. However, the proofs in Sections 3.3 and 4.3 rely on properties specific to affine finite elements and the lumped-mass L^2 projection. Consequently, these arguments do not extend directly to higher-order elements and nodally averaged gradients. Developing an optimal-order a priori analysis for higher-order versions of the method therefore remains an important topic.

Another possible direction is the extension of the method to other classes of partial differential equations (PDEs). While we used projected gradients to stabilize the effects of small cut cells for elliptic PDEs, the concept was originally introduced for the stabilization of convective terms (see [CB97; CB02; JKL06; JK10; VRK25]). As noted in Remarks 3.2 and 4.1, incorporating PG stabilization into unfitted FEMs for convection dominated transport problems is a natural next step. Similarly, applying the technique to unfitted FEMs for parabolic PDEs is a reasonable and potentially fruitful direction.

Turning to the tumor growth setting of Chapter 5, one possible research topic is to establish stronger regularity properties for the solutions. For the thin-rim limit model (5.17), we expect H^2 regularity for the pressure. It would be interesting to derive analogous regularity statements for the pressure variable in the full tumor growth model (5.1). Such results may enable convergence statements in spaces of higher regularity. In Section 5.2, convergence was proven only for the special case

of stationary rotationally symmetric solutions. Since the formal asymptotics in Section 5.1 applies to the general case, it is reasonable to conjecture that convergence can be shown in the general setting as well.

Once the applicability of unfitted FEMs with PG stabilization to hyperbolic and parabolic PDEs has been established, a further research direction is the application of the method to the full tumor growth model (5.1). However, since this model does not account for all mechanisms relevant to tumor growth, such an investigation represents only an initial step. To gain deeper insight into tumor dynamics, the method should eventually be applied to more comprehensive models that incorporate additional biological processes. Moreover, realistic simulations will require three-dimensional computations. While the theoretical results in this thesis are independent of the number of spatial dimensions, an efficient implementation in 2D/3D will require investigating optimization opportunities from a high-performance computing perspective. In addition parallelization and GPU acceleration, it would be worthwhile to develop customized algorithms for boosting performance. Remarks 3.5 and 4.5 discussed the structure of the algebraic system obtained from the unfitted FEMs with PG stabilization. For example, the system matrices exhibit sparsity patterns, potentially allowing for the design of tailored sparse preconditioners to improve solver performance.

List of Figures

List of Tables

Acronyms

BVP	boundary value problem
CIP	continuous interior penalty
DMP	discrete maximum principle
EOC	experimental order of convergence
FEM	finite element method
GP	ghost penalty
H^2	Hansbo & Hansbo
PDE	partial differential equation
PG	projected gradient
SBM	shifted-boundary method
SDF	signed distance function
TP	Test Problem

Bibliography

[AS95] D. Adalsteinsson and J. A. Sethian. "A fast level set method for propagating interfaces". In: *J. Comput. Phys.* 118.2 (1995), pp. 269–277. DOI: 10.1006/jcph.1995.1098.

[AS99] D. Adalsteinsson and J. A. Sethian. "The fast construction of extension velocities in level set methods". In: *J. Comput. Phys.* 149.1 (1999), pp. 2–22. DOI: 10.1006/jcph.1995.1098.

[AB12] J. A. Adam and N. Bellomo. *A Survey of Models for Tumor-Immune System Dynamics*. Modeling and Simulation in Science, Engineering and Technology. Birkhäuser, 2012. ISBN: 978-0-8176-8119-7. DOI: 10.1007/978-0-8176-8119-7. Originally published in 1996.

[AGL05] J. Ahrens, B. Geveci, and C. Law. "Paraview: An end-user tool for large data visualization". In: *Visualization Handbook*. Ed. by C. D. Hansen and C. R. Johnson. Butterworth-Heinemann, 2005, pp. 717–731. ISBN: 978-0-12-387582-2. DOI: 10.1016/B978-012387582-2/50038-1.

[Alt16] H. W. Alt. *Linear Functional Analysis*. Universitext. Springer, 2016. ISBN: 978-1-4471-7280-2. DOI: 10.1007/978-1-4471-7280-2.

[And+21] R. Anderson, J. Andrej, A. Barker, J. Bramwell, J.-S. Camier, J. Cerveny, V. Dobrev, Y. Dudouit, A. Fisher, T. Kolev, W. Pazner, M. Stowell, V. Tomov, I. Akkerman, J. Dahm, D. Medina, and S. Zampini. "MFEM: A modular finite element methods library". In: *Comput. Math. Appl.* 81 (2021), pp. 42–74. DOI: 10.1016/j.camwa.2020.06.009.

[And+24] J. Andrej, N. Atallah, J.-P. Bäcker, J.-S. Camier, D. Copeland, V. Dobrev, Y. Dudouit, T. Duswald, B. Keith, D. Kim, T. Kolev, B. Lazarov, K. Mittal, W. Pazner, S. Petrides, S. Shiraiwa, M. Stowell, and V. Tomov. "High-performance finite elements with MFEM". In: *Int. J. High Perform. Comput. Appl.* 38.5 (2024), pp. 447–467. DOI: 10.1177/10943420241261981.

[Ant+24] N. Antonelli, R. Aristio, A. Gorgi, R. Zorrilla, R. Rossi, G. Scovazzi, and R. Wüchner. "The shifted boundary method in isogeometric analysis". In: *Comput. Methods Appl. Mech. Eng.* 430 (2024), p. 117228. DOI: 10.1016/j.cma.2024.117228.

[AM04] R. P. Araujo and D. L. S. McElwain. "A history of the study of solid tumour growth: The contribution of mathematical modelling". In: *Bull. Math. Biol.* 66 (2004), pp. 1039–1091. DOI: 10.1016/j.bulm.2003.11.002.

[ACS20] N. Atallah, C. Canuto, and G. Scovazzi. "The second-generation Shifted Boundary Method and its numerical analysis". In: *Comput. Methods Appl. Mech. Eng.* 372 (2020), p. 113341. DOI: 10.1016/j.cma.2020.113341.

[ACS21] N. Atallah, C. Canuto, and G. Scovazzi. "Analysis of the shifted boundary method for the Poisson problem in domains with corners". In: *Math. Comput.* 90.331 (2021), pp. 2041–2069. DOI: 10.1090/mcom/3641.

[ACS22] N. Atallah, C. Canuto, and G. Scovazzi. "The high-order shifted boundary method and its analysis". In: *Comput. Methods Appl. Mech. Eng.* 394 (2022), p. 114885. DOI: 10.1016/j.cma.2022.114885.

[ABI12] R. F. Ausas, G. C. Buscaglia, and S. R. Idelsohn. "A new enrichment space for the treatment of discontinuous pressures in multi-fluid flows". In: *Int. J. Numer. Meth. Fluid.* 70.7 (2012), pp. 829–850. DOI: 10.1002/fld.2713.

[Aya15] U. Ayachit. *The ParaView Guide: A Parallel Visualization Application*. Kitware, Inc., 2015. ISBN: 978-1-930934-30-6. DOI: 10.5555/2789330.

[BNV22] S. Badia, E. Neiva, and F. Verdugo. "Linking ghost penalty and aggregated unfitted methods". In: *Comput. Methods Appl. Mech. Eng.* 388 (2022), p. 114232. DOI: 10.1016/j.cma.2021.114232.

[BVM18] S. Badia, F. Verdugo, and A. F. Martín. "The aggregated unfitted finite element method for elliptic problems". In: *Comput. Methods Appl. Mech. Eng.* 336 (2018), pp. 533–553. DOI: 10.1016/j.cma.2018.03.022.

[Bän01] E. Bänsch. "Finite element discretization of the Navier–Stokes equations with a free capillary surface". In: *Numer. Math.* 88 (2001), pp. 203–235. DOI: 10.1007/PL00005443.

[Bän+23] E. Bänsch, K. Deckelnick, H. Garcke, and P. Pozzi. *Interfaces: Modeling, Analysis, Numerics*. Vol. 51. Oberwolfach Seminars. Birkhäuser, 2023. ISBN: 978-3-031-35550-9. DOI: 10.1007/978-3-031-35550-9.

[BS20] E. Bänsch and A. Schmidt. "Free boundary problems in fluids and materials". In: *Geometric Partial Differential Equations - Part I*. Ed. by A. Bonito and R. H. Nochetto. Vol. 21. Handbook of Numerical Analysis. Elsevier, 2020, pp. 555–619. ISBN: 978-0-444-64003-1. DOI: 10.1016/bs.hna.2019.05.004.

[BJK16] G. R. Barrenechea, V. John, and P. Knobloch. "Analysis of Algebraic Flux Correction Schemes". In: *SIAM J. Numer. Anal.* 54.4 (2016), pp. 2427–2451. DOI: 10.1137/15M1018216.

[BGN13] J. W. Barrett, H. Garcke, and R. Nürnberg. "Eliminating spurious velocities with a stable approximation of viscous incompressible two-phase Stokes flow". In: *Comput. Methods Appl. Mech. Eng.* 267 (2013), pp. 511–530. DOI: 10.1016/j.cma.2013.09.023.

[BGN20] J. W. Barrett, H. Garcke, and R. Nürnberg. "Parametric finite element approximations of curvature-driven interface evolutions". In: *Geometric Partial Differential Equations - Part I*. Ed. by A. Bonito and R. H. Nochetto. Vol. 21. Handbook of Numerical Analysis. Elsevier, 2020, pp. 275–423. ISBN: 978-0-444-64003-1. DOI: 10.1016/bs.hna.2019.05.002.

[Bas17] C. Basting. "Optimization-Based Finite Element Methods for Evolving Interfaces". Dissertation. TU Dortmund University, 2017. DOI: 10.17877/DE290R-18051.

[BK13] C. Basting and D. Kuzmin. "A minimization-based finite element formulation for interface-preserving level set reinitialization". In: *Computing* 95.1 (2013), pp. 13–25. DOI: 10.1007/s00607-012-0259-z.

[BK14] C. Basting and D. Kuzmin. "Optimal control for mass conservative level set methods". In: *J. Comput. Phys.* 270 (2014), pp. 343–352. DOI: 10.1016/j.cam.2013.12.040.

[BKS17] C. Basting, D. Kuzmin, and J. N. Shadid. "Optimal control for reinitialization in finite element level set methods". In: *Int. J. Numer. Meth. Fluid.* 84.5 (2017), pp. 292–305. DOI: 10.1002/fld.4348.

[BW13] S. Basting and M. Weismann. "A hybrid level set–front tracking finite element approach for fluid–structure interaction and two-phase flow applications". In: *J. Comput. Phys.* 255 (2013), pp. 228–244. DOI: 10.1016/j.jcp.2013.08.018.

[BW14] S. Basting and M. Weismann. "A hybrid level set/front tracking approach for finite element simulations of two-phase flows". In: *J. Comput. Appl. Math.* 270 (2014), pp. 471–483. DOI: 10.1016/j.cam.2013.12.014.

[BH08] R. Becker and P. Hansbo. "A simple pressure stabilization method for the Stokes equation". In: *Comm. Numer. Methods Eng.* 24.11 (2008), pp. 1421–1430. DOI: 10.1002/cnm.1041.

[BP00] N. Bellomo and L. Preziosi. "Modelling and mathematical problems related to tumor evolution and its interaction with the immune system". In: *Math. Comput. Modell.* 32.3–4 (2000), pp. 413–452. DOI: 10.1016/S0895-7177(00)00143-6.

[BG14] H. Benninghoff and H. Garcke. "Efficient image segmentation and restoration using parametric curve evolution with junctions and topology changes". In: *SIAM J. Imag. Sci.* 7.3 (2014), pp. 1451–1483. DOI: 10.1137/130932430.

[BG17] H. Benninghoff and H. Garcke. "Segmentation of three-dimensional images with parametric active surfaces and topology changes". In: *J. Sci. Comput.* 72 (2017), pp. 1333–1367. DOI: 10.1007/s10915-017-0401-3.

[BET11] J. Benzaken, J. Evans, and R. Tamstorf. "Constructing Nitsche's method for variational problems". In: *Arch. Comput. Methods Eng.* 31 (2011), pp. 1867–1896. DOI: 10.1007/s11831-023-09953-6.

[Boi+11] O. Boiarkine, D. Kuzmin, S. Čanić, G. Guidoboni, and A. Mikelić. "A positivity-preserving ALE finite element scheme for convection–diffusion equations in moving domains". In: *J. Comput. Phys.* 230.8 (2011), pp. 2896–2914. DOI: 10.1016/j.jcp.2010.12.042.

[Bor+18] S. P. Bordas, E. Burman, M. G. Larson, and M. A. Olshanskii, eds. *Geometrically Unfitted Finite Element Methods and Applications: Proceedings of the UCL Workshop 2016*. Vol. 121. Lecture Notes in Computational Science and Engineering. Springer, 2018. ISBN: 978-3-319-71431-8. DOI: 10.1007/978-3-319-71431-8.

[BS02] S. C. Brenner and L. R. Scott. *The Mathematical Theory of Finite Element Methods*. Vol. 15. Texts in Applied Mathematics. Springer, 2002. ISBN: 978-1-4757-3658-8. DOI: 10.1007/978-1-4757-3658-8.

[BSM20] H.-G. Bui, D. Schillinger, and G. Meschke. "Efficient cut-cell quadrature based on moment fitting for materially nonlinear analysis". In: *Comput. Methods Appl. Mech. Eng.* 366 (2020), p. 113050. DOI: 10.1016/j.cma.2020.113050.

[Bur10] E. Burman. "Ghost Penalty". In: *Comptes Rendus Math.* 348.21-22 (2010), pp. 1217–1220. DOI: 10.1016/j.crma.2010.10.006.

[Bur12] E. Burman. "A penalty-free nonsymmetric Nitsche-type method for the weak imposition of boundary conditions". In: *SIAM J. Numer. Anal.* 50.4 (2012), pp. 1959–1981. DOI: 10.1137/10081784X.

[Bur+21] E. Burman, M. Cicuttin, G. Delay, and A. Ern. "An unfitted hybrid high-order method with cell agglomeration for elliptic interface problems". In: *SIAM J. Sci. Comput.* 43.2 (2021), A859–A882. DOI: 10.1137/19M1285901.

[Bur+15] E. Burman, S. Claus, P. Hansbo, M. G. Larson, and A. Massing. "CutFEM: Discretizing geometry and partial differential equations". In: *Int. J. Numer. Methods Eng.* 104.7 (2015), pp. 472–501. DOI: 10.1002/nme.4823.

[BCM15] E. Burman, S. Claus, and A. Massing. "A stabilized cut finite element method for the three field Stokes problem". In: *SIAM J. Sci. Comput.* 37.4 (2015), A1705–A1726. DOI: 10.1137/140983574.

[BE07] E. Burman and A. Ern. "Continuous interior penalty *hp*-finite element methods for advection and advection-diffusion equations". In: *Math. Comput.* 76 (2007), pp. 1119–1140. DOI: 10.1090/S0025-5718-07-01951-5.

[BE18] E. Burman and A. Ern. "An unfitted hybrid high-order method for elliptic interface problems". In: *SIAM J. Numer. Anal.* 56.3 (2018), pp. 1525–1546. DOI: 10.1137/17M1154266.

[BH10] E. Burman and P. Hansbo. "Fictitious domain finite element methods using cut elements: I. A stabilized Lagrange multiplier method". In: *Comput. Methods Appl. Mech. Eng.* 199.41–44 (2010), pp. 2680–2686. DOI: 10.1016/j.cma.2010.05.011.

[BH12] E. Burman and P. Hansbo. "Fictitious domain finite element methods using cut elements: II. A stabilized Nitsche method". In: *Appl. Numer. Math.* 62.4 (2012), pp. 328–341. DOI: 10.1016/j.apnum.2011.01.008.

[BH14] E. Burman and P. Hansbo. "Fictitious domain methods using cut elements: III. A stabilized Nitsche method for Stokes' problem". In: *ESAIM:M2AN* 48.3 (2014), pp. 859–874. DOI: 10.1051/m2an/2013123.

[BHL18] E. Burman, P. Hansbo, and M. G. Larson. "A cut finite element method with boundary value correction". In: *Math. Comput.* 87 (2018), pp. 633–657. DOI: 10.1090/mcom/3240.

[Bur66] A. C. Burton. "Rate of growth of solid tumours as a problem of diffusion". In: *Growth* 30.2 (1966), pp. 157–176.

[Byr+03] H. Byrne, J. King, D. McElwain, and L. Preziosi. "A two-phase model of solid tumour growth". In: *Appl. Math. Lett.* 16.4 (2003), pp. 567–573. DOI: 10.1016/S0893-9659(03)00038-7.

[BP03] H. Byrne and L. Preziosi. "Modeling solid tumour growth using the theory of mixtures". In: *Math. Med. Biol.* 20 (2003), pp. 341–366. DOI: 10.1093/imammb/20.4.341.

[Car+21] T. Carraro, S. E. Wetterauer, A. V. P. Bobadilla, and D. Trucu. "A level-set approach for a multi-scale cancer invasion model". In: *Math. Appl. Sci. Eng.* 2.1 (2021), pp. 1–23. DOI: 10.5206/mase/11087.

[Che+97] S. Chen, B. Merriman, S. Osher, and P. Smereka. "A simple level set method for solving Stefan problems". In: *J. Comput. Phys.* 135.1 (1997), pp. 8–29. DOI: 10.1006/jcph.1997.5721.

[CZ98] Z. Chen and J. Zou. "Finite element methods and their convergence for elliptic and parabolic interface problems". In: *Numer. Math.* 79 (1998), pp. 175–202. DOI: 10.1007/s002110050336.

[CSB02] J. Chessa, P. Smolinski, and T. Belytschko. "The extended finite element method (XFEM) for solidification problems". In: *Int. J. Numer. Methods Eng.* 53.8 (2002), pp. 1959–1977. DOI: 10.1002/nme.386.

[Cho24] F. Chouly. *Finite Element Approximation of Boundary Value Problems*. Compact Textbooks in Mathematics. Birkhäuser, 2024. ISBN: 978-3-031-72530-2. DOI: 10.1007/978-3-031-72530-2.

[Cia02] P. G. Ciarlet. *The Finite Element Method for Elliptic Problems*. Society for Industrial and Applied Mathematics, 2002. ISBN: 978-0-89871-920-8. DOI: 10.1137/1.9780898719208.

[CB09] R. Codina and J. Baiges. "Approximate imposition of boundary conditions in immersed boundary methods". In: *Int. J. Numer. Methods Eng.* 80.11 (2009), pp. 1379–1405. DOI: 10.1002/nme.2662.

[Cod+23] R. Codina, J. Baiges, I. Castañar, I. Martínez-Suárez, L. Moreno, and S. Parada. "An embedded strategy for large scale incompressible flow simulations in moving domains". In: *J. Comput. Phys.* 488 (2023), p. 112181. DOI: 10.1016/j.jcp.2023.112181.

[CB97] R. Codina and J. Blasco. "A finite element formulation for the Stokes problem allowing equal velocity-pressure interpolation". In: *Comput. Methods Appl. Mech. Eng.* 143.3–4 (1997), pp. 373–391. DOI: 10.1016/S0045-7825(96)01154-1.

[CB02] R. Codina and J. Blasco. "Analysis of a stabilized finite element approximation of the transient convection-diffusion-reaction equation using orthogonal subscales". In: *Comput. Vis. Sci.* 4 (2002), pp. 167–174. DOI: s007910100068.

[CGH15] P. Colli, G. Gilardi, and D. Hilhorst. "On a Cahn-Hilliard type phase field system related to tumor growth". In: *Discrete Contin. Dyn. Syst.* 35.6 (2015), pp. 2423–2442. DOI: 10.3934/dcds.2015.35.2423.

[CLN03] V. Cristini, J. Lowengrub, and Q. Nie. "Nonlinear simulation of tumor growth". In: *J. Math. Biol.* 46 (2003), pp. 191–224. DOI: 10.1007/s00285-002-0174-6.

[DP00] E. De Angelis and L. Preziosi. "Advection-diffusion models for solid tumour evolution in vivo and related free boundary problem". In: *Math. Models Methods Appl. Sci.* 10.3 (2000), pp. 379–407. DOI: 10.1142/S0218202500000239.

[DD00] K. Deckelnick and G. Dziuk. "Error estimates for a semi-implicit fully discrete finite element scheme for the mean curvature flow of graphs". In: *Interfaces Free Boundaries* 2.4 (2000), pp. 341–359. DOI: 10.4171/IFB/24.

[DDE05] K. Deckelnick, G. Dziuk, and C. M. Elliott. "Computation of geometric partial differential equations and mean curvature flow". In: *Acta Numer.* 14 (2005), pp. 139–232. DOI: 10.1017/S0962492904000224.

[DT06] A. Dervieux and F. Thomasset. "A finite element method for the simulation of a Rayleigh-Taylor instability". In: *Approximation Methods for Navier-Stokes Problems*. Ed. by R. Rautmann. Vol. 771. Lecture Notes in Mathematics. Springer, 2006, pp. 145–158. ISBN: 978-3-540-38550-9. DOI: 10.1007/BFb0086904. Originally appeared in 1980.

[DK10a] V. Dobrev and T. Kolev. *GLVis: OpenGL Finite Element Visualization Tool*. glvis.org. 2010. DOI: 10.11578/dc.20171025.1249.

[DK10b] V. Dobrev and T. Kolev. *MFEM: Modular Finite Element Methods Library*. mfem.org. 2010. DOI: 10.11578/dc.20171025.1248.

[DGH82] J. Donea, S. Giuliani, and J. P. Halleux. "An arbitrary lagrangian-eulerian finite element method for transient dynamic fluid-structure interactions". In: *Comput. Methods Appl. Mech. Eng.* 33.1–3 (1982), pp. 689–723. DOI: 10.1016/0045-7825(82)90128-1.

[Don18] D. Donner. "Gradientenrekonstruktionstechnicken zur Stabilisierung konvenktiver Terme bei stetigen Galerkin-Diskretisierungen hoher Ordnung". Master's Thesis. TU Dortmund University, 2018.

[DF20] Q. Du and X. Feng. "The phase field method for geometric moving interfaces and their numerical approximations". In: *Geometric Partial Differential Equations - Part I*. Ed. by A. Bonito and R. H. Nochetto. Vol. 21. Handbook of Numerical Analysis. Elsevier, 2020, pp. 425–508. ISBN: 978-0-444-64003-1. DOI: 10.1016/bs.hna.2019.05.001.

[DH20] A. Düster and S. Hubirch. "Adaptive integration of cut finite elements and cells for nonlinear structural analysis". In: *Modeling in Engineering Using Innovative Numerical Methods for Solids and Fluids*. Ed. by L. De Lorenzis and A. Düster. Scientific Computation. Springer, 2020, pp. 31–73. ISBN: 978-3-030-37518-8. DOI: 10.1007/978-3-030-37518-8_2.

[DE13] G. Dziuk and C. M. Elliott. "Finite element methods for surface PDEs". In: *Acta Numer.* 22 (2013), pp. 289–396. DOI: 10.1017/S0962492913000056.

[Eck+09] C. Eck, M. A. Fontelos, G. Grün, F. Klingbeil, and O. Vantzos. "On a phase-field model for electrowetting". In: *Interfaces Free Boundaries* 11.2 (2009), pp. 259–290. DOI: 10.4171/IFB/211.

[EKL25] D. Edelmann, B. Kovács, and C. Lubich. "Numerical analysis of an evolving bulk–surface model of tumour growth". In: *IMA J. Numer. Anal.* 45.5 (2025), pp. 2581–2627. DOI: 10.1093/imanum/drae077.

[ETT05] B. Engquist, A.-K. Tornberg, and R. Tsai. "Discretization of Dirac delta functions in level set methods". In: *J. Comput. Phys.* 207.1 (2005), pp. 28–51. DOI: 10.1016/j.jcp.2004.09.018.

[EG04] A. Ern and J.-L. Guermond. *Theory and Practice of Finite Elements*. Vol. 159. Applied Mathematical Sciences. Springer, 2004. ISBN: 978-1-4757-4355-5. DOI: 10.1007/978-1-4757-4355-5.

[EG21] A. Ern and J.-L. Guermond. *Finite Elements I: Approximation and Interpolation*. Vol. 72. Texts in Applied Mathematics. Springer, 2021. ISBN: 978-3-030-56341-7. DOI: 10.1007/978-3-030-56341-7.

[Eva10] L. C. Evans. *Partial Differential Equations*. Vol. 19. Graduate Studies in Mathematics. American Mathematical Society, 2010. ISBN: 978-0-8218-4974-3. DOI: 10.1090/gsm/019.

[Eyl19] J. Eyles. "Numerical analysis and simulations of a tractable model for tumour growth". Dissertation. University of Sussex, 2019.

[EKS19] J. Eyles, J. R. King, and V. Styles. "A tractable mathematical model for tissue growth". In: *Interfaces Free Boundaries* 21.4 (2019), pp. 463–493. DOI: 10.4171/IFB/428.

[FN99] L. Formaggia and F. Nobile. "A stability analysis for the arbitrary Lagrangian Eulerian formulation with finite elements". In: *East-West J. Math.* 7.2 (1999), pp. 105–132.

[FN04] L. Formaggia and F. Nobile. "Stability analysis of second-order time accurate schemes for ALE–FEM". In: *Comput. Methods Appl. Mech. Eng.* 193.39–41 (2004), pp. 4097–4116. DOI: 10.1016/j.cma.2003.09.028.

[FGR15] S. Frigeri, M. Grasselli, and E. Rocca. "On a diffuse interface model of tumour growth". In: *Eur. J. Appl. Math.* 26.2 (2015), pp. 215–243. DOI: 10.1017/S0956792514000436.

[Gar+16] H. Garcke, K. F. Lam, E. Sitka, and V. Styles. "A Cahn–Hilliard–Darcy model for tumour growth with chemotaxis and active transport". In: *Math. Models Methods Appl. Sci.* 26.6 (2016), pp. 1095–1148. DOI: 10.1142/S0218202516500263.

[GT22] H. Garcke and D. Trautwein. "Numerical analysis for a Cahn–Hilliard system modelling tumour growth with chemotaxis and active transport". In: *J. Numer. Math.* 30.4 (2022), pp. 295–324. DOI: 10.1515/jnma-2021-0094.

[GD22] W. Garhuom and A. Düster. "Non-negative moment fitting quadrature for cut finite elements and cells undergoing large deformations". In: *Comput. Mech.* 70 (2022), pp. 1059–1081. DOI: 10.1007/s00466-022-02203-9.

[GG03] R. A. Gatenby and E. T. Gawlinski. "The glycolytic phenotype in carcinogenesis and tumor invasion: Insights through mathematical models". In: *Cancer Res.* 63.14 (2003), pp. 3847–3854. DOI: 10.1158/0008-5472.CAN-03-0231.

[Gib+07] F. Gibou, L. Chen, D. Nguyen, and S. Banerjee. "A level set based sharp interface method for the multiphase incompressible Navier–Stokes equations with phase change". In: *J. Comput. Phys.* 222.2 (2007), pp. 536–555. DOI: 10.1016/j.jcp.2006.07.035.

[Gli+98] J. Glimm, J. W. Grove, X. L. Li, K.-M. Shyue, Y. Zeng, and Q. Zhang. "Three-dimensional front tracking". In: *SIAM J. Sci. Comput.* 19.3 (1998), pp. 703–727. DOI: /10.1137/S1064827595293600.

[Gre72] H. P. Greenspan. "Models for the growth of a solid tumor by diffusion". In: *Stud. Appl. Math.* 51.4 (1972), pp. 317–340. DOI: 10.1002/sapm1972514317.

[Gre74] H. P. Greenspan. "On the self-inhibited growth of cell cultures". In: *Growth* 38.1 (1974), pp. 81–95.

[Gre76] H. P. Greenspan. "On the growth and stability of cell cultures and solid tumors". In: *J. Theor. Biol.* 56.1 (1976), pp. 229–242. DOI: 10.1016/S0022-5193(76)80054-9.

[GR11] S. Gross and A. Reusken. *Numerical Methods for Two-phase Incompressible Flows*. Vol. 40. Springer Series in Computational Mathematics. Springer, 2011. ISBN: 978-3-642-19686-7. DOI: 10.1007/978-3-642-19686-7.

[HKA19] H. Hajduk, D. Kuzmin, and V. Aizinger. "New directional vector limiters for discontinuous Galerkin methods". In: *J. Comput. Phys.* 384 (2019), pp. 308–325. DOI: 10.1016/j.jcp.2019.01.032.

[HH02] A. Hansbo and P. Hansbo. "An unfitted finite element method, based on Nitsche's method, for elliptic interface problems". In: *Comput. Methods Appl. Mech. Eng.* 191.47-48 (2002), pp. 5537–5552. DOI: 10.1016/S0045-7825(02)00524-8.

[HLZ14] P. Hansbo, M. G. Larson, and S. Zahedi. "A cut finite element method for a Stokes interface problem". In: *Appl. Numer. Math.* 85 (2014), pp. 90–114. DOI: 10.1016/j.apnum.2014.06.009.

[Haw+13] A. Hawkins-Daarud, S. Prudhomme, K. G. van der Zee, and J. T. Oden. "Bayesian calibration, validation, and uncertainty quantification of diffuse interface models of tumor growth". In: *J. Math. Biol.* 67 (2013), pp. 1457–1485. DOI: 10.1007/s00285-012-0595-9.

[HN81] C. W. Hirt and B. D. Nichols. "Volume of fluid (VOF) method for the dynamics of free boundariues". In: *J. Comput. Phys.* 39 (1981), pp. 201–225. DOI: 10.1016/0021-9991(81)90145-5.

[HMS05] C. S. Hogea, B. T. Murray, and J. A. Sethian. "Implementation of the level set method for continuum mechanics based tumor growth models". In: *Fluid Dyn. Mater. Process.* 1.2 (2005), pp. 109–130. DOI: 10.3970/fdmp.2005.001.109.

[HMS06] C. S. Hogea, B. T. Murray, and J. A. Sethian. "Simulating complex tumor dynamics from avascular to vascular growth using a general level-set method". In: *J. Math. Biol.* 53 (2006), pp. 86–134. DOI: 10.1007/s00285-006-0378-2.

[HLZ81] T. J. Hughes, W. K. Liu, and T. K. Zimmermann. "Lagrangian-Eulerian finite element formulation for incompressible viscous flows". In: *Comput. Methods Appl. Mech. Eng.* 29.3 (1981), pp. 329–349. DOI: 10.1016/0045-7825(81)90049-9.

[Hys06] S. Hysing. "A new implicit surface tension implementation for interfacial flows". In: *Int. J. Numer. Methods Fluids* 51.6 (2006), pp. 659–672. DOI: 10.1002/fld.1147.

[Hys07] S.-R. Hysing. "Numerical Simulation of Immiscible Fluids with FEM Level Set Techniques". Dissertation. TU Dortmund University, 2007. DOI: 10.17877/DE290R-65.

[Jac01] D. Jacqmin. "Calculation of two-phase Navier-Stokes flows using phase-field modeling". In: *J. Comput. Phys.* 169.2 (2001), pp. 624–651. DOI: 10.1006/jcph.2000.6692.

[Jam+99] D. Jamet, O. Lebaigue, N. Coutris, and J. M. Delhaye. "The second gradient method for the direct numerical simulation of liquid-vapor flows with phase change". In: *J. Comput. Phys.* 155.1 (1999), pp. 96–127. DOI: 10.1006/jcph.1999.6332.

[JKL06] V. John, S. Kaya, and W. Layton. "A two-level variational multiscale method for convection-dominated convection–diffusion equations". In: *Comput. Methods Appl. Mech. Eng.* 195.33-36 (2006), pp. 4594–4603. DOI: 10.1016/j.cma.2005.10.006.

[JK10] V. John and A. Kindl. "A variational multiscale method for turbulent flow simulation with adaptive large scale space". In: *J. Comput. Phys.* 229.2 (2010), pp. 301–312. DOI: 10.1016/j.jcp.2009.09.025.

[JK07] V. John and P. Knobloch. "On spurious oscillations at layers diminishing (SOLD) methods for convection–diffusion equations: Part I – A review". In: *Comput. Methods Appl. Mech. Eng.* 196.17-20 (2007), pp. 2197–2215. DOI: 10.1016/j.cma.2006.11.013.

[Kee+11] C. E. Kees, I. Akkermann, M. W. Farthing, and Y. Bazilevs. "A conservative level set method suitable for variable-order approximations and unstructured meshes". In: *J. Comput. Phys.* 230.12 (2011), pp. 4536–4558. DOI: 10.1016/j.jcp.2011.02.030.

[Kel74] R. B. Kellogg. "On the Poisson equation with intersecting interfaces". In: *Appl. Anal.* 4.2 (1974), pp. 101–129. DOI: 10.1080/00036817408839086.

[KF06] J. King and S. Franks. "Mathematical Modelling of Nutrient-limited Tissue Growth". In: *Free Boundary Problems*. Ed. by I. Figueiredo, J. Rodrigues, and L. Santos. Vol. 154. International Series of Numerical Mathematics. Brinkhäuser, 2006, pp. 273–282. ISBN: 978-3-7643-7719-9. DOI: 10.1007/978-3-7643-7719-9_27.

[KT16] C. Kublik and R. Tsai. "Integration over curves and surfaces defined by the closest point mapping". In: *Res. Math. Sci.* 3.1 (2016), p. 3. DOI: 10.1186/s40687-016-0053-1.

[KT18] C. Kublik and R. Tsai. "An extrapolative approach to integration over hypersurfaces in the level set framework". In: *Math. Comput.* 87.313 (2018), pp. 2365–2392. DOI: 10.1090/mcom/3282.

[Kuz12] D. Kuzmin. "Algebraic flux correction I". In: *Flux-Corrected Transport*. Ed. by D. Kuzmin, R. Löhner, and S. Turek. 2nd ed. Scientific Computation. Springer, 2012, pp. 145–192. ISBN: 978-94-007-4038-9. DOI: 10.1007/978-94-007-4038-9.

[Kuz14] D. Kuzmin. "An optimization-based approach to enforcing mass conservation in level set methods". In: *J. Comput. Phys.* 258 (2014), pp. 78–86. DOI: 10.1016/j.cam.2013.09.009.

[KB22] D. Kuzmin and J.-P. Bäcker. "An unfitted finite element method using levle set functions for extrapolation into deformable diffuse interfaces". In: *J. Comput. Phys.* 461 (2022), p. 111218. DOI: 10.1016/j.jcp.2022.111218.

[KH23] D. Kuzmin and H. Hajduk. *Property-Preserving Numerical Schemes for Conservation Laws*. World Scientific, 2023. ISBN: 978-981-127-820-4. DOI: 10.1142/13466.

[KQ20] D. Kuzmin and M. Quezada de Luna. "Entropy conservation property and entropy stabilization of high-order continuous Galerkin approximations to scalar conservation laws". In: *Comput. Fluids* 213 (2020), p. 104742. DOI: 10.1016/j.compfluid.2020.104742.

[LT08] S. Larsson and V. Thomée. *Partial Differential Equations with Numerical Methods*. Vol. 45. Texts in Applied Mathematics. Springer, 2008. ISBN: 978-3-540-88706-5. DOI: 10.1007/978-3-540-88706-5.

[Leh15] C. Lehrenfeld. "On a Space-Time Extended Finite Element Method for the Solution of a Class of Two-Phase Mass Transport Problems". Dissertation. RWTH Aachen University, 2015.

[LO19] C. Lehrenfeld and M. Olshanskii. "An Eulerian finite element method for PDEs in time-dependent domains". In: *ESAIM: M2AN* 53.2 (2019), pp. 585–614. DOI: 10.1051/m2an/2018068.

[LL97] R. J. LeVeque and Z. Li. "Immersed interface methods for Stokes flow with elastic boundaries or surface tension". In: *SIAM J. Sci. Comput.* 18.3 (1997), pp. 709–735. DOI: 10.1137/S106482759528253.

[Li+20] K. Li, N. M. Atallah, G. A. Main, and G. Scovazzi. "The shifted interface method: a flexible approach to embedded interface computations". In: *Int. J. Numer. Methods Eng.* 121.3 (2020), pp. 492–518. DOI: 10.1002/nme.6231.

[Li+09] X. Li, J. Lowengrub, A. Rätz, and A. Voigt. "Solving PDEs in complex geometries: a diffuse domain approach". In: *Commun. Math. Sci.* 7.1 (2009), pp. 81–107. DOI: 10.4310/cms.2009.v7.n1.a4.

[Loh+17] C. Lohmann, D. Kuzmin, J. N. Shadid, and S. Mabuza. "Flux-corrected transport algorithms for continuous Galerkin methods based on high order Bernstein finite elements". In: *J. Comput. Phys.* 344 (2017), pp. 151–186. DOI: 10.1016/j.jcp.2017.04.059.

[Low+10] J. S. Lowengrub, H. B. Frieboes, F. Jin, Y.-L. Chuang, X. Li, P. Macklin, S. M. Wise, and V. Cristini. "Nonlinear modelling of cancer: bridging the gap between cells and tumours". In: *Nonlinearity* 23.1 (2010), R1–R91. DOI: 10.1088/0951-7715/23/1/R01.

[MS18a] A. Main and G. Scovazzi. "The shifted boundary method for embedded domain computations. Part I: Poisson and Stokes problems". In: *J. Comput. Phys.* 372 (2018), pp. 972–995. DOI: 10.1016/j.jcp.2017.10.026.

[MS18b] A. Main and G. Scovazzi. "The shifted boundary method for embedded domain computations. Part II: Linear advection-diffusion and incompressible Navier–Stokes equations". In: *J. Comput. Phys.* 372 (2018), pp. 996–1026. DOI: 10.1016/j.jcp.2017.10.026.

[Mas+14] A. Massing, M. G. Larson, A. Logg, and M. E. Rognes. "A stabilized Nitsche fictitious domain method for the Stokes problem". In: *J. Sci. Comput.* 61 (2014), pp. 604–628. DOI: 10.1007/s10915-014-9838-9.

[MSW18] A. Massing, B. Schott, and W. A. Wall. "A stabilized Nitsche cut finite element method for the Oseen problem". In: *Comput. Methods Appl. Mech. Eng.* 328 (2018), pp. 262–300. DOI: 10.1016/j.cma.2017.09.003.

[MM78] D. L. S. McElwain and L. E. Morris. "Apoptosis as a volume loss mechanism in mathematical models of solid tumor growth". In: *Math. Biosci.* 39.1–2 (1978), pp. 147–157. DOI: 10.1016/0025-5564(78)90033-0.

[MP77] D. L. S. McElwain and P. J. Ponzo. "A model for the growth of a solid tumor with non-uniform oxygen consumption". In: *Math. Biosci.* 35.3–4 (1977), pp. 267–279. DOI: 10.1016/0025-5564(77)90028-1.

[MI05] R. Mittal and G. Iaccarino. "Immersed boundary methods". In: *Annu. Rev. Fluid Mech.* 37.1 (2005), pp. 239–261. DOI: 10.1146/annurev.fluid.37.061903.175743.

[MKO13] B. Müller, F. Kummer, and M. Oberlack. "Highly accurate surface and volume integration on implicit domains by means of moment-fitting". In: *Int. J. Numer. Methods Eng.* 96.8 (2013), pp. 512–528. DOI: 10.1002/nme.4569.

[Nit71] J. Nitsche. "Über ein Variationsprinzip zur Lösung von Dirichlet-Problemen bei Verwendung von Teilräumen, die keinen Randbedingungen unterworfen sind". In: *Abhandlungen aus dem mathematischen Seminar der Universität Hamburg*. Vol. 36. 1. 1971, pp. 9–15. DOI: 10.1007/BF02995904.

[OBK25] M. Olshanskii, J.-P. Bäcker, and D. Kuzmin. "Gradient-penalty stabilization of sharp and diffuse interface formulations in unfitted Nitsche finite element methods". In: *ESAIM:M2AN* 59.6 (2025), pp. 2933–2955. DOI: 10.1051/m2an/2025079.

[OW25] M. Olshanskii and H. von Wahl. "Stability of instantaneous pressures in an Eulerian finite element method for moving boundary flow problems". In: *J. Comput. Phys.* 533 (2025), p. 113983. DOI: 10.1016/j.jcp.2025.113983.

[OF01] S. Osher and R. P. Fedkiw. "Level set methods: An overview and some recent results". In: *J. Comput. Phys.* 169.2 (2001), pp. 463–502. DOI: 10.1006/jcph.2000.6636.

[OS88] S. Osher and J. A. Sethian. "Fronts propagating with curvature-dependent speed: Algorithms based on Hamilton-Jacobi formulations". In: *J. Comput. Phys.* 79.1 (1988), pp. 12–49. DOI: 10.1016/0021-9991(88)90002-2.

[OF06] S. Osher and R. Fedkiw. *Level Set Methods and Dynamic Implicit Surfaces*. Vol. 153. Applied Mathematical Sciences. eBook version of the 2002 edition. Springer, 2006. ISBN: 978-0-387-22746-7. DOI: 10.1007/b98879.

[Pen+17] L. Peng, D. Trucu, P. Lin, A. Thompson, and M. A. J. Chaplain. "A multiscale mathematical model of tumour invasive growth". In: *Bull. Math. Biol.* 79 (2017), pp. 389–429. DOI: 10.1007/s11538-016-0237-2.

[Pes00] C. S. Peskin. "The immersed boundary method". In: *Acta Numer.* 11 (2000), pp. 2480–2492. DOI: 10.1017/S0962492902000077.

[PE12] D. A. D. Pietro and A. Ern. *Mathematical Aspects of Discontinuous Galerkin Methods*. Vol. 69. Mathématiques et Applications. Springer, 2012. ISBN: 978-3-642-22980-0. DOI: 10.1007/978-3-642-22980-0.

[PP01] L. M. Pismen and Y. Pomeau. "Disjoining potential and spreading of thin liquid layers in the diffuse-interface model coupled to hydrodynamics". In: *Phys. Rev. E* 62.2 (2001), pp. 463–502. DOI: 10.1103/PhysRevE.62.2480.

[Pre+23] F. de Prenter, C. V. Verhoosel, E. H. van Brummelen, M. G. Larson, and S. Badia. "Stability and conditioning of immersed finite element methods: analysis and remedies". In: *Arch. Comput. Methods Eng.* 30 (2023), pp. 3617–3656. DOI: 10.1007/s11831-023-09913-0.

[Pre03] L. Preziosi. *Cancer Modelling and Simulation*. CRC Press, 2003. ISBN: 978-0-203-49489-9. DOI: 10.1201/9780203494899.

[QHK20] M. Quezada de Luna, J. Haydel Collins, and C. E. Kees. "An unstructured finite element model for incompressible two-phase flow based on a monolithic conservative level set method". In: *Int. J. Numer. Methods Fluids* 92.9 (2020), pp. 1058–1080. DOI: 10.1002/fld.4817.

[QKK19] M. Quezada de Luna, D. Kuzmin, and C. E. Kees. "A monolithic conservative level set method with built-in redistancing". In: *J. Comput. Phys.* 379 (2019), pp. 262–278. DOI: 10.1016/j.jcp.2018.11.044.

[RE14] A. Reusken and P. Esser. "Analysis of time discretization methods for Stokes equations with a nonsmooth forcing term". In: *Numer. Math.* 126 (2014), pp. 293–319. DOI: 10.1007/s00211-013-0564-2.

[Reu13] A. Reusken. "A finite element level set redistancing method based on gradient recovery". In: *SIAM J. Numer. Anal.* 51.5 (2013), pp. 2723–2745. DOI: 10.1137/120895433.

[Sau+21] K. Saurabh, M. Ishii, M. Fernando, B. Gao, K. Tan, M.-C. Hsu, A. Krishnamurthy, H. Sundar, and B. Ganapathysubramanian. "Scalable adaptive PDE solvers in arbitrary domains". In: *Proceedings of the International Conference for High Performance Computing, Networking, Storage and Analysis*. Ed. by B. R. de Supinski, M. W. Hall, and T. Gamblin. Vol. 154. International Series of Numerical Mathematics. Association for Computing Machinery, 2021, pp. 1–15. ISBN: 978-1-4503-8442-1. DOI: 10.1145/3458817.

[SZ99] R. Scardovelli and S. Zaleski. "Direct numerical msimulations of free-surface and interfacial flow". In: *Annu. Rev. Fluid Mech.* 31 (1999), pp. 567–603. DOI: 10.1146/annurev.fluid.31.1.567.

[SW08] J. Schlottke and B. Weigand. "Direct numerical simulation of evaporating droplets". In: *J. Comput. Phys.* 227.10 (2008), pp. 5215–5237. DOI: 10.1016/j.jcp.2008.01.042.

[Sch24] B. Schweizer. *Partielle Differentialgleichungen*. Masterclass. Springer, 2024. ISBN: 978-3-662-67188-7. DOI: 10.1007/978-3-662-67188-7.

[SBP13] M. Scianna, C. Bell, and L. Preziosi. "A review of mathematical models for the formation of vascular networks". In: *J. Theor. Biol.* 333 (2013), pp. 174–209. DOI: 10.1016/j.jtbi.2013.04.037.

[Set01] J. A. Sethian. "Evolution, implementation, and application of level set and fast marching methods for advancing fronts". In: *J. Comput. Phys.* 169.2 (2001), pp. 503–555. DOI: 10.1006/jcph.2000.6657.

[SS03] J. A. Sethian and P. Smereka. "Level set methods for fluid interfaces". In: *Annu. Rev. Fluid Mech.* 35.1 (2003), pp. 341–372. DOI: 10.1146/annurev.fluid.35.101101.161105.

[Sme06] P. Smereka. "The numerical approximation of a delta function with application to level set methods". In: *J. Comput. Phys.* 211.1 (2006), pp. 77–90. DOI: 10.1016/j.jcp.2005.05.005.

[SD98] D. Son and V. K. Dhir. "Numerical simulation of film boiling near critical pressures with a level set method". In: *J. Heat Transfer* 120.1 (1998), pp. 183–192. DOI: 10.1115/1.2830042.

[Ste71] E. M. Stein. *Singular Integrals and Differentiability Properties of Functions*. Vol. 30. Princeton Mathematical Series. Princeton University Press, 1971. ISBN: 978-0-691-08079-6. DOI: 10.1515/9781400883882.

[Ste09] I. Steinbach. "Phase-field models in materials science". In: *Modelling Simul. Mater. Sci. Eng.* 17.7 (2009), p. 73001. DOI: 10.1088/0965-0393/17/7/073001.

[SSO94] M. Sussman, P. Smereka, and S. Osher. "A level set approach for computing solutions to incompressible two-phase flow". In: *J. Comput. Phys.* 114.1 (1994), pp. 146–159. DOI: 10.1006/jcph.1994.1155.

[TMB07] S. Tanguy, T. Ménard, and A. Berlemont. "A level set method for vaporizing two-phase flows". In: *J. Comput. Phys.* 221.2 (2007), pp. 837–853. DOI: 10.1016/j.jcp.2006.07.003.

[Tei+07] K. E. Teigen, X. Li, J. Lowengrub, F. Wang, and A. Voigt. "A diffuse-interface approach for modelling transport, diffusion and adsorption/desorption of material quantities on a deformable interface". In: *Commun. Math. Sci-* 7.4 (2007), pp. 1009–1037. DOI: 10.4310/cms.2009.v7.n4.a10.

[Tei+11] K. E. Teigen, P. Song, J. Lowengrub, and A. Voigt. "A diffuse-interface method for two-phase flows with soluble surfactant". In: *J. Comput. Phys.* 230.2 (2011), pp. 375–393. DOI: 10.1016/j.jcp.2010.09.020.

[Tra24] D. Trautwein. "Viscoelastic Phase-Field Models for Tumour Growth: Modelling, Analysis and Numerics". Dissertation. Universität Regensburg, 2024. DOI: 10.5283/epub.59630.

[Try+01] G. Tryggvason, B. Bunner, A. Esmaeeli, D. Juric, N. Al-Rawahi, W. Tauber, J. Han, S. Nas, and Y.-J. Jan. "Two methods for discretizing a delta function supported on a level set". In: *J. Comput. Phys.* 169.2 (2001), pp. 708–759. DOI: 10.1006/jcph.2001.6726.

[TSZ11] G. Tryggvason, R. Scardovelli, and S. Zaleski. *Direct Numerical Simulations of Gas–Liquid Multiphase Flows*. Cambridge University Press, 2011. ISBN: 978-0-511-97526-4. DOI: 10.1017/CBO9780511975264.

[TK12] S. Turek and D. Kuzmin. "Algebraic flux correction III". In: *Flux-Corrected Transport*. Ed. by D. Kuzmin, R. Löhner, and S. Turek. 2nd ed. Scientific Computation. Springer, 2012, pp. 239–297. ISBN: 978-94-007-4038-9. DOI: 10.1007/978-94-007-4038-9.

[UT92] S. O. Unverdi and G. Tryggvason. "A front-tracking method for viscous, incompressible, multi-fluid flows". In: *J. Comput. Phys.* 100 (1992), pp. 25–37. DOI: 10.1016/0021-9991(92)90307-K.

[UK18] T. Utz and F. Kummer. "A high-order discontinuous Galerkin method for extension problems". In: *Int. J. Numer. Methods Fluids* 86.8 (2018), pp. 509–518. DOI: 10.1002/fld.4464.

[VRK25] J. Vedral, A. Rupp, and D. Kuzmin. "Strongly consistent low-dissipation WENO schemes for finite elements". In: *Appl. Numer. Math.* 210 (2025), pp. 64–81. DOI: 10.1016/j.apnum.2024.12.008.

[Vog06] W. Vogt. *Adaptive Verfahren zur numerischen Quadratur und Kubatur*. Tech. rep. Preprint No. M 06/01. Institut für Mathematik, TU Ilmenau, 2006.

[Wad+13] E. Wadbro, S. Zahedi, G. Kreiss, and M. Berggren. "A uniformly well-conditioned, unfitted Nitsche method for interface problems". In: *BIT Numer. Math.* 53 (2013), pp. 791–820. DOI: 10.1007/s10543-012-0417-x.

[Wah21] H. M. von Wahl. "Unfitted Finite Elements for Fluid-Rigid Body Interaction Problems". Dissertation. Otto-von-Guericke-Universität Magdeburg, 2021. DOI: 10.25673/40013.

[WK97] J. P. Ward and J. R. King. "Mathematical modelling of avascular-tumour growth". In: *Math. Med. Biol.* 14.1 (1997), pp. 39–69. DOI: 10.1093/imammb/14.1.39.

[Wat87] A. J. Wathen. "Realistic eigenvalue bounds for the Galerkin mass matrix". In: *IMA J. Numer. Anal.* 7.4 (1987), pp. 449–457. DOI: 10.1093/imanum/7.4.449.

[WW00] S. W. Welch and J. Wilson. "A volume of fluid based method for fluid flows with phase changes". In: *J. Comput. Phys.* 160.2 (2000), pp. 662–682. DOI: 10.1006/jcph.2000.6481.

[XVG16] J. Xu, G. Vilanova, and H. Gomez. "A mathematical model coupling tumor growth and angiogenesis". In: *PLoS ONE* 11.2 (2016), e0149422. DOI: 10.1371/journal.pone.0149422.

[Yan+24] C.-H. Yang, K. Saurabh, G. Scovazzi, C. Canuto, A. Krishnamurthy, and B. Ganapathysubramanian. "Optimal surrogate boundary selection and scalability studies for the shifted boundary method on octree meshes". In: *Comput. Methods Appl. Mech. Eng.* 419 (2024), p. 116686. DOI: 10.1016/j.cma.2023.116686.

[ZT10] S. Zahedi and A.-K. Tornberg. "Delta function approximations in level set methods by distance function extension". In: *J. Comput. Phys.* 229.6 (2010), pp. 2199–2219. DOI: 10.1016/j.jcp.2009.11.030.

[Žen90] A. Ženíšek. "The finite element method for nonlinear elliptic equations with discontinuous coefficients". In: *Numer. Math.* 58 (1990), pp. 51–77. DOI: 10.1007/BF01385610.

[ZWC05] X. Zheng, S. M. Wise, and V. Cristini. "Nonlinear simulation of tumor necrosis, neo-vascularization and tissue invasion via an adaptive finite-element/level-set method". In: *Bull. Math. Biol.* 67 (2005), pp. 211–259. DOI: 10.1016/j.bulm.2004.08.001.

[ZZ92a] O. C. Zienkiewicz and J. Z. Zhu. "The superconvergent patch recovery and a posteriori error estimates. Part 1: The recovery technique". In: *Int. J. Num. Meth. Eng.* 33.7 (1992), pp. 1331–1364. DOI: 10.1002/nme.1620330702.

[ZZ92b] O. C. Zienkiewicz and J. Z. Zhu. "The superconvergent patch recovery and a posteriori error estimates. Part 2: Error estimates and adaptivity". In: *Int. J. Num. Meth. Eng.* 33.7 (1992), pp. 1365–1382. DOI: 10.1002/nme.1620330703.